AQP5: A functional gastric cancer stem cell marker in mouse and human tumors

Authors: Hui Yi Grace Lim[1]†, Swathi Yada[1]†, Kazuhiro Murakami[2], Bernett Teck Kwong Lee[3,4,5,6], Sowmya Sagiraju[1], Phyllis Phuah[1], Tanysha Chi-Ying Chen[1], Fidelia B. Alvina[1], Si Hui Tan[1], Kaushal Krishna Kaslikar[3,4], Nur Syahirah Binte Ruhazat[3,4,7], Menaka Priyadharsani Rajapakse[8], Katzrin Bte Ahmad Murad[1], Snezhina Kancheva[1], Liang Thing Tan[1], Seri Mustafah[8], Jimmy Bok Yan So[9,10], Nick Barker[1,11]*

Affiliations: [1]Institute of Molecular and Cell Biology (IMCB), Agency for Science, Technology and Research (A*STAR); 61 Biopolis Drive, Proteos, Singapore 138673, Republic of Singapore.

[2]Division of Epithelial Stem Cell Biology, Cancer Research Institute, Kanazawa University; Kanazawa, Japan.

[3]Lee Kong Chian School of Medicine, Nanyang Technological University; Singapore 636921, Singapore.

[4]Centre for Biomedical Informatics, Lee Kong Chian School of Medicine, Nanyang Technological University; Singapore 636921, Singapore.

[5]Clinical Research Unit, Khoo Teck Puat Hospital; Singapore 768828, Singapore.

[6]A*STAR Infectious Diseases Labs (A*STAR ID Labs), Agency for Science, Technology and Research (A*STAR); 8A Biomedical Grove, Immunos, Singapore 138648, Republic of Singapore.

[7]School of Biological Sciences, Nanyang Technological University; Singapore, Singapore.

[8]Singapore Immunology Network (SIgN), Agency for Science, Technology and Research (A*STAR); 8A Biomedical Grove, Immunos, Singapore 138648, Republic of Singapore.

[9]Department of Surgery, Yong Loo Lin School of Medicine, National University of Singapore; Singapore.

[10]Division of Surgical Oncology, National University Cancer Institute of Singapore; Singapore.

[11]Department of Physiology, Yong Loo Lin School of Medicine, National University of Singapore (NUS); Singapore.

†These authors contributed equally.

*Corresponding author. Email: nicholas_barker@a-star.edu.sg.

Abstract: Cancer stem cells (CSCs) represent a self-renewing population capable of fuelling long-term tumour growth. In gastric cancer, the identity of CSC populations remains unclear. Here, we establish a gastric CSC population marked by the water channel protein AQP5, which reside in human and mouse pyloric tumours. Using multiple organoid and mouse models, we find a requirement for AQP5+ CSCs in both initiating and sustaining cancer progression and demonstrate that AQP5 expression also directly promotes tumour growth and invasion in a WNT, PI3K, and MAPK-dependent manner. Beyond primary cancers, AQP5 further enriches for a functional CSC population in metastatic tumours. Together, our findings support a CSC model in gastric tumours which may have application for therapeutic strategies targeting CSCs.

Main Text:

The concept of targeting cancer stem cells (CSCs) has gained traction in recent years as a therapeutic opportunity to drive long-term remission of cancers (*1*). Like their healthy adult stem cell equivalents, long-lived CSCs residing in tumours are proposed to self-renew and give rise to differentiated cell lineages, driving tumour progression. CSCs are also believed to be a contributor to metastatic dissemination and tumour relapse with the ability to evade standard anti-tumour drug regimens (*2*), requiring alternative strategies to target and eliminate them in the clinic. This is particularly relevant for gastric cancer, which ranks as one of the deadliest cancers worldwide with a high rate of recurrence in patients (*3*). Yet, the primary treatment method for gastric cancer remains surgical resection and chemotherapy, with few available options for advanced metastatic disease (*4*).

Despite the value of defining CSCs involved in gastric cancer progression and relapse, a CSC population residing within primary mouse or human gastric tumours has not convincingly been demonstrated. Generic stem markers such as CD44 have been identified in other cancers, and suggested to mark gastric CSCs, but remain poorly validated only in several cancer cell lines to harbour stem-like properties (*5–7*). Other stem-associated markers such as SOX2 (*8*) play broad functions in maintaining homeostasis of healthy tissues and lack cell surface expression, limiting its utility for targeting and isolating human gastric CSCs. Indeed, despite the numerous correlative markers proposed over the years, the identity of the CSC population residing in human primary gastric tumours remains unclear and no CSC-specific marker has yet emerged as a viable therapeutic target.

We therefore sought to address this critical gap by defining the identity of a gastric CSC population expressing the surface marker AQP5 that resides within primary gastric tumours of both mice and humans. We performed multiple assays that collectively support CSC potential: the ability to generate long-term self-renewing organoid cultures, the ability to reform tumours following *in vivo* transplantation, and lineage tracing of endogenous CSCs and their progeny, demonstrating the CSC-driven maintenance of stem and differentiated lineages. To directly test the therapeutic potential of a targeted CSC-based approach, we employed organoid and mouse models facilitating the selective ablation of AQP5+ CSCs and report a central requirement for these cells in both tumour initiation and subsequent growth. We established that AQP5 itself promotes cancer cell proliferation and invasion across a wide spectrum of gastric cancer models via WNT, PI3K, and MAPK-dependent mechanisms. Finally, we show that in addition to primary gastric tumours, AQP5 is also a functional marker of CSCs in metastatic tumours.

AQP5 marks a subset of epithelial cells within mouse and human pyloric tumours

To study the contribution of AQP5+ tumour cells towards gastric cancer, we first characterized the expression of AQP5 within mouse pyloric tumours. Recombination of conditional *Apc*, *Pten*, and $Kras^{G12D}$ floxed alleles under an *Aqp5-eGFP-IRES-creERT2* driver to model the major co-dysregulated pathways prevalent in human gastric tumours resulted in the formation of Aqp5-Cre/APK pyloric tumours in these mice within 2 to 3 months that were classified as tubular-type adenocarcinoma (Fig. 1A; fig. S1A), as previously described (*9*). AQP5 expression is restricted to the tissue-resident stem cell compartment at pyloric gland bases prior to cancer induction, overlapping with *Lgr5* (Fig. 1B; fig. S1B). At later stages of cancer progression, increasing numbers of AQP5+ tumour cells can be detected in the transformed pyloric epithelium, including regions above the gland bases (Fig. 1, B and C). As insertion of the *Aqp5-eGFP-IRES-creERT2*

cassette disrupts *Aqp5* gene transcription beyond exon 1, we incorporated this allele in a heterozygous form to retain endogenous expression of AQP5 and confirmed spatiotemporal patterns of AQP5 expression during tumour progression using an alternative *Aqp5-2A-creERT2* pyloric cancer model in which *Aqp5* gene transcription is not perturbed (fig. S1, C and D). In agreement with these histological analyses, single cell RNA sequencing (scRNAseq) of Aqp5-Cre/APK pyloric tumours indicated that *Aqp5* was elevated in a subset of tumour epithelial cell lineages (fig. S2, A to C). Notably, while expression patterns of *Aqp5* and *Lgr5* are highly restricted to the same stem cell cluster in the healthy pylorus (*9*), cells expressing the highest levels of *Aqp5* are enriched in a *Pgc/Muc6*+ cluster largely separate from the *Lgr5*+ cluster within pyloric tumours, with a smaller subset of cells co-expressing the two markers (fig. S2, B to D). To localise these *Aqp5*+ cell subsets within the intact pyloric tumour, we also performed imaging-based spatial transcriptomics using MERSCOPE and constructed a spatial cellular map of the mouse Aqp5-Cre/APK tumour (fig. S2E). This approach revealed 8 clusters corresponding to tumour epithelial lineages (fig. S2F), of which 3 showed elevated *Aqp5* transcript levels and mapped to both the gland bases and tumour compartments immediately above the gland bases, including Wnt-active clusters overlapping with *Lgr5*+ cells as well as proliferative clusters expressing *Mki67* (fig. S2, E to G). In line with our scRNAseq dataset, the highest *Aqp5*-expressers resided at gland bases, where they co-express *Pgc* (fig. S2, E to G). Finally, we evaluated *Aqp5* expression in these mouse pyloric tumours relative to other putative gastric CSC markers including *Lgr5*, *Cxcr4*, and *Cd44* using both our scRNAseq dataset as well as RNAscope performed on additional independent tumour sections (fig. S3, A and B), confirming that *Aqp5* labels a distinct subpopulation of pyloric tumour cells.

We established a strategy to isolate these pyloric tumour epithelial AQP5+ and AQP5- cell populations within mouse Aqp5-Cre/APK tumours by fluorescence-activated cell sorting (FACS) to derive biological insights from AQP5+ tumour cells (Fig. 1D; Table S1). The Aqp5-Cre/APK model harbours a Rosa26-tdTomatoLSL reporter that traces entire pyloric glands within one week following induction (*9*), facilitating the use of tdTomato as a marker to isolate the tumour epithelial population, together with eGFP as a reporter of *Aqp5* expression. We further confirmed the specific overlap between this tdTomato reporter and tumour epithelium based on hyperactivated WNT and MAPK signalling within these transformed cells (fig. S3, C to E), which is distinct from gene signatures present in healthy populations (fig. S3, F and G). Sorted eGFP+ tumour epithelial cells showed an average of 9.8-fold enrichment in *Aqp5* levels by qPCR compared to eGFP- cells (Fig. 1E). Using this sorting strategy, we performed transcriptomic profiling of AQP5+ and AQP5- tumour epithelial cells isolated from 6 independent Aqp5-Cre/APK mouse pyloric tumours (fig. S4A). This revealed the selective enrichment of extracellular matrix (ECM) remodelling, epithelial-mesenchymal transition (EMT), and drug resistance-associated pathways in the AQP5+ tumour cell transcriptome (Fig. 1F; fig. S4, B and C; Table S2), features typically associated with CSCs in other systems (*10*–*13*). We validated many of these upregulated genes including *Pthlh*, *Rgs5*, and *Hey1* using additional mouse pyloric tumour samples by qPCR and RNAscope (fig. S4, D to H), confirming their enrichment in the AQP5+ tumour cell population.

We previously identified and characterized AQP5-expressing stem cells in the healthy human pylorus (*9*). We next performed a detailed evaluation of their tumour equivalents, and conducted a comprehensive analysis of *AQP5* expression using publicly available human scRNAseq datasets of healthy stomach and gastric tumour tissues (*14*, *15*). We used published lineage markers to identify the tumour epithelial clusters, representing the gastric mucous (*MUC5AC*+, *MUC6*+) and enteroendocrine (*CHGA*+) lineages, along with intestinal-like (*TFF3*+, *FABP1*+) populations (fig. S5, A and B). Within the healthy human pylorus, *AQP5* is primarily

expressed in the *MUC6*+ mucous gland base cell cluster (fig. S5, C and D), previously associated with the gastric stem cell compartment in both mice and humans (*9*). *AQP5* expression in human gastric tumours is elevated across multiple epithelial cell clusters with the highest levels enriched within the *MUC6*+ compartment, aligning with observations from our mouse pyloric tumour dataset (fig. S5, C and D). Notably, *AQP5* expression displays tumour subtype-specific patterns, with the largest elevation in *AQP5* levels detected in intestinal-type tumours over their healthy counterparts (fig. S5, E to H). Further comparison of *AQP5* expression patterns against other proposed CSC markers revealed that many CD proteins were broad-spectrum markers present across epithelial and non-epithelial fractions, whereas *AQP5* and *LGR5* expression were specific to the tumour epithelium with the highest expressers enriched in different cell clusters, in line with our mouse dataset (fig. S6, A and B). We confirmed these observations using an independent human scRNAseq dataset, where *AQP5* levels were also elevated in gastric tumour cells over their healthy equivalents, particularly in the *MUC6*+ mucous cell cluster (fig. S6, C to E), and by detecting AQP5 at the protein level using IHC performed on human gastric tissue microarrays (Fig. 1G; fig. S6F), corroborating previous work (*16–18*). Collectively, these analyses identify an elevated AQP5 expression signature in a subset of epithelial cells within human gastric tumours primarily associated with intestinal-type tumours, features that are captured in our Aqp5-Cre/APK mouse pyloric cancer model.

As AQP5 is a surface protein amenable to antibody-based FACS, we adapted our sorting protocols to isolate AQP5+ and AQP5- human pyloric tumour epithelial cells from freshly collected patient tumour biopsies (Fig. 1H; Table S3). Our FACS sorting strategy was validated by qPCR reflecting a mean of 10.8-fold upregulation of *AQP5* levels in the sorted AQP5+ cell population (Fig. 1I). Using this sorting approach, we performed bulk RNAseq analyses on isolated AQP5+ and AQP5- human pyloric tumour cells from 5 independent tumour samples (fig. S7A). Like the mouse AQP5+ profile, human AQP5+ tumour cells displayed a transcriptomic signature enriched in CSC-associated phenotypes, including ECM organization, EMT, and chemoresistance (Fig. 1J; fig. S7, B and C; Table S4). We validated selected upregulated targets including *CLDN2*, *HEY2*, and *PLA1A* by qPCR and RNAscope using additional independent patient tumour samples (fig. S7, D to H), confirming the accuracy of our RNAseq dataset. In all, we identify an upregulated AQP5 expression signature within a subset of mouse and human pyloric tumour cells and establish methods to isolate primary mouse and human AQP5+ pyloric tumour cells, revealing a CSC-enriched profile in this cell population.

AQP5+ tumour cells function as CSCs in mouse and human pyloric tumours

Markers that label healthy and cancer stem cells are known to be highly overlapping in many tumour contexts (*19*). However, existing stem cell markers including LGR5, CD44, and CXCR4 have not been shown to identify gastric CSCs using functional assays of stem potential (*5–8*, *20*), although targeted ablation of LGR5+ gastric tumour cells does ameliorate cancer progression in mouse models (*21*). Given that AQP5 marks the healthy mouse and human pyloric stem cell compartment (*9*), and many reported CSC-associated pathway signatures are enriched in the transcriptomes derived from AQP5+ tumour cells (Fig. 1; fig. S4 and S7), we asked if AQP5 could also be a specific marker enriching for the pyloric CSC population within mouse and human gastric tumours. To functionally test this hypothesis, we isolated AQP5+ and AQP5- epithelial tumour cells from Aqp5-Cre/APK mouse pyloric tumours by FACS and seeded them for organoid culture as a readout of their *in vitro* stem cell potential. This revealed organoid formation by AQP5+ tumour cells that could be maintained long-term (more than 10 passages) (Fig. 2, A and B).

Moreover, organoids derived from isolated AQP5+ tumour cells contained multiple differentiated cell lineages that resembled organoids generated from whole pyloric tumour glands (Fig. 2C; fig. S8A), suggesting their multi-lineage potential. In contrast, AQP5- tumour cells formed on average 9-fold fewer organoids in culture that were rapidly lost within 2 passages (Fig. 2, A and B), reflecting a lack of self-renewal capacity. To further investigate the retention of a long-lived stem population within these AQP5+ cell-derived organoids, we performed a secondary FACS isolation of AQP5+ and AQP5- cells from these organoids and evaluated their organoid initiation efficiency. This revealed that AQP5+ cells in AQP5+ cell-derived organoids continue to display organoid outgrowth and stem cell potential (fig. S8B). Thus, AQP5 marks a functional CSC population within mouse pyloric tumours capable of long-term tumour organoid growth.

Another approach to assess CSC potential is by transplantation of specific cell populations into mice to evaluate their tumour-forming capacity in an *in vivo* context. As noted in previous studies, it remains challenging to transplant sorted cell populations from solid tumours, and efficiency of tumour initiation can vary markedly depending on the tissue type and recipient (*22*). To circumvent this issue, we transplanted Aqp5-Cre/APK pyloric tumour organoids into immune-deficient mice and FACS sorted AQP5+ and AQP5- cells from the resultant orthotopic tumours for re-transplantation back into the pylorus of immune-deficient mice (fig. S8C), as we reasoned that these cells would have better adapted to the local tumour environment within their hosts. We confirmed that tumour organoids (and orthotopic tumour derivatives) were similar to primary pyloric tumours in terms of 1) histology, with a certified animal pathologist confirming both models as tubular-type gastric adenocarcinoma with shared histological features of cellular atypia, hyperchromatism, and loss of basement membrane integrity (fig. S8, D and E); 2) molecular profiles, with enrichment of cancer-promoting and chemoresistance genes upregulated in AQP5+ cells derived from both models (fig. S8F); and 3) functional properties of AQP5+ cells, which function in both models as a CSC population through their ability to sustain long-lived organoid cultures (fig. S8G). Using this strategy, sorted tumour epithelial cells from Aqp5-Cre/APK orthotopic tumours seeded new tumours in mice more efficiently than cells isolated from primary tumours (fig. S9, A and B), offering a viable system for evaluating their tumour initiation capacities. Across the independent sets of mice examined, AQP5+ tumour cells consistently established orthotopic tumours that were larger in volume with more severe dysplastic and necrotic lesions with abundant invasion into the muscular layer, driving moderate degenerative changes in the smooth muscles (Fig. 2, D and E). In contrast, transplanted AQP5- tumour cells derived from the same tumour are retained within the submucosal space at the site of injection with no signs of invasion into other tissue layers, inflammation, or necrosis (Fig. 2, D and E). AQP5+ cell-derived tumours were also composed of both AQP5+ and AQP5- cells, including the expression of multiple differentiated cell lineages (fig. S9C), indicating that these AQP5+ CSCs have the capacity to reconstitute the diverse lineages within their original tumours. Notably, AQP5- cells are devoid of AQP5 immediately following transplantation but a minor subset is capable of activating AQP5 expression by the 3-week timepoint (fig. S9, D and E), suggesting that these populations are highly plastic with the potential to interconvert under specific contexts.

To evaluate whether AQP5+ tumour cells function more broadly as CSCs across multiple gastric cancer types, we isolated AQP5+ and AQP5- tumour cells from an independent pyloric cancer mouse model harbouring the constitutively active $p53^{R172H}$ mutant (fig. S10, A to C), given that *Trp53* is frequently mutated in human gastric cancers (*23*). FACS isolation of these cells was validated by qPCR reflecting a 38-fold enrichment of *Aqp5* in the sorted AQP5+ population (fig. S10, D and E). As with the Aqp5-Cre/APK pyloric tumour model, sorted AQP5+ tumour cells from P53 mutant tumours formed 8.4-fold more organoids *in vitro* compared to AQP5- cells

derived from the same tumour (fig. S10, F and G), indicating that AQP5+ cells likely also function as stem cells in this context. We further analyzed AQP5+ populations within a third model incorporating a Cldn18-CreERT2 driver that targets mutations throughout the gastric epithelium (fig. S10, H and I). Like the other pyloric cancer models, AQP5+ and AQP5- cells could be efficiently isolated by FACS (fig. S10, J and K). In this model, efficiency of organoid outgrowth from sorted AQP5+ cells was also markedly elevated over the AQP5- population (fig. S10, L and M). Taken together, the organoid initiation and transplantation assays support mouse AQP5+ tumour cells as a functional gastric CSC population capable of long-term self-renewal and multi-lineage differentiation across multiple gastric cancer models.

We then asked if human AQP5+ pyloric tumour cells also function as CSCs. To this end, we isolated AQP5+ and AQP5- cells from primary patient tumour biopsy samples and plated these cells for organoid culture. We found that human AQP5+ tumour cells generated tumour organoids at a 25.6-fold higher rate than the corresponding AQP5- cells isolated from the same tumour (Fig. 2, F and G). The AQP5+ tumour cell-derived organoids also displayed long-term self-renewal capabilities (beyond 10 passages) and gave rise to differentiated cell lineages resembling human organoids established from whole pyloric glands (Fig. 2H; fig. S11A), suggesting that the human AQP5+ cell population retains an intrinsic stem capacity for repopulating the cell lineages and characteristics of its original tumour. In contrast, the small proportion of AQP5- cell-derived organoids that formed failed to propagate beyond an average of 3 passages (Fig. 2, F and G).

As an additional readout of stem potential of the human AQP5+ tumour cell population, we performed transplantation of sorted human AQP5+ and AQP5- cells isolated from xenografts derived from orthotopically transplanted human gastric cancer organoids. Like their mouse counterparts, human AQP5+ cells seeded significantly larger and more invasive tumours following orthotopic transplantation (Fig. 2, I and J), which were highly proliferative and continued to express AQP5 (fig. S11B). In contrast, human AQP5- cells were predominantly incapable of establishing tumours following transplantation (Fig. 2, I and J; fig. S11B), supporting the presence of a CSC pool within the transplanted human AQP5+ population. Finally, we established human gastric tumour organoids with CRISPR/Cas9-mediated insertion of *AQP5-2A-CreERT2; CAG-LSL-tdTomato* to facilitate *in vitro* lineage tracing of human AQP5+ cells and their progeny within these tumour organoids (fig. S11, C and D). Short-term administration of 4-hydroxytamoxifen (4-OHT) to these tumour organoid cultures resulted in the labelling of a small pool of AQP5+ cells, with subsequent expansion of reporter expression to encompass differentiated gastric lineage markers over time (fig. S11, E to G). In contrast, uninduced organoids never displayed tdTomato tracing across the same timepoints (fig. S11H). Therefore, multiple independent assays of stem potential collectively support the finding that human AQP5+ tumour cells also function as a CSC population that contributes to the long-term maintenance of organoid cultures and generation of multiple differentiated cell lineages.

Ablation of AQP5+ tumour cells impairs tumour development

CSCs are considered a major source of tumour relapse due to their ability to resist standard cancer therapies via multiple mechanisms, including activation of drug efflux transporters (*24*). Methods of targeting CSCs have thus been proposed as a clinical strategy to reduce tumour burden and recurrence, but this has been hindered by the current lack of well-validated and clinically relevant markers of gastric CSCs. In view of our functional characterization of mouse and human AQP5+ cells as a CSC population in pyloric tumours (Fig. 2; fig. S8 to 11), we therefore proceeded to test

the effect of ablating AQP5+ cells in mouse and human gastric tumour models as an independent functional readout of their CSC identity and to evaluate the effectiveness of targeting the AQP5+ CSC population in gastric cancer.

To selectively ablate AQP5+ tumour cells in mouse pyloric tumours, we incorporated the *Aqp5-2A-DTR* allele into our Aqp5-Cre/APK pyloric cancer mouse model, which facilitates endogenous expression of AQP5 together with the diphtheria toxin receptor (DTR) in AQP5-expressing cells (fig. S12A). Aqp5-Cre/APK/DTR tumours were indistinguishable from Aqp5-Cre/APK tumours in terms of tumour morphology, tumour load, and proportion of tumour-resident AQP5+ cells (fig. S12B). To selectively target AQP5+ pyloric tumour cells, we performed intraperitoneal administration of diphtheria toxin (DT) to Aqp5-Cre/APK/DTR mice harbouring pyloric tumours. 12h after the last DT dose, DT-treated tumours were significantly reduced in size (fig. S12, C and D). We confirmed the loss of AQP5 expression in DT-treated tumours and the concurrent emergence of Caspase3+ apoptotic cells and a KI67+ proliferative response in the surviving AQP5- tumour load suggestive of activation of tumour plasticity mechanisms (fig. S12D). There was no effect of DT on pyloric tumours in Aqp5-Cre/APK mice lacking the *Aqp5-2A-DTR* allele (fig. S12E), or in Aqp5-Cre/APK and Aqp5-Cre/APK/DTR mice receiving PBS injections without DT (fig. S12, D and E).

While administration of DT to Aqp5-Cre/APK/DTR mice ablates AQP5+ pyloric tumour cells, AQP5+ cells in other healthy tissues are also affected, leading to high mortality rates in these mice that precludes analysis of late tumour timepoints. To circumvent this issue, we generated tumour organoids from Aqp5-Cre/APK/DTR pyloric tumours that maintained a small (9.2%) pool of cells expressing high levels of AQP5 in culture (fig. S12F). Addition of DT to Aqp5-Cre/APK/DTR organoid cultures during the initial stages of organoid outgrowth ablated the majority of AQP5+ cells, with an 80-90% reduction in *Aqp5* levels 1 day after treatment (fig. S12G),and completely abolished organoid outgrowth across 4 independent lines examined (Fig. 3, A and B). We also tested the effect of DT administration to established Aqp5-Cre/APK/DTR organoid cultures, which resulted in a >90% reduction in *Aqp5* levels (fig. S12G) and rapid degeneration of organoids within 1 day of treatment, with no viable organoids remaining after 4 days (Fig. 3, C and D). In contrast, the same DT dosage given to Aqp5-Cre/APK organoids lacking the *Aqp5-2A-DTR* allele had no effect on Aqp5 expression or on organoid outgrowth and subsequent organoid maintenance (fig. S12, H to J), highlighting a specific effect of AQP5+ cell ablation on the observed organoid phenotypes.

To corroborate these findings within a more physiological system, we established methods to orthotopically transplant Aqp5-Cre/APK/DTR tumour organoids into the pylorus of immune-deficient mice to facilitate the selective ablation of AQP5+ cells in pyloric tumours developed from these organoids (Fig. 3E). Importantly, as the *Aqp5-2A-DTR* allele is not expressed in other tissues within these mice, we are able to monitor tumour progression to more advanced stages following DT administration without complications arising from systemically ablating AQP5+ cells. We confirmed that orthotopic transplantation of Aqp5-Cre/APK/DTR pyloric organoids resulted in initiation of adenomatous hyperplasia within 4 weeks (Fig. 3F; fig. S13A), which progressed to adenocarcinomas with signs of invasion into the epithelium by 8 weeks (Fig. 3G; fig. S13B). Intraperitoneal injection of DT to mice immediately following orthotopic transplantation of Aqp5-Cre/APK/DTR tumour organoids resulted in the loss of AQP5-expressing cells (fig. S13C) and completely inhibited tumour outgrowth at 4 weeks in all mice examined (Fig. 3F; fig. S13A), highlighting the role of AQP5+ CSCs in tumour initiation *in vivo*. To evaluate the requirement of AQP5+ tumour cells in driving subsequent tumour progression, we then

administered DT to established tumours in mice 4 weeks after orthotopic transplantation of Aqp5-Cre/APK/DTR organoids and validated the ablation efficiency in these tumours (fig. S13D). In contrast to untreated tumours, DT-treated tumours displayed an almost 8-fold reduction in tumour load with no accompanying invasion into the surrounding tissue layers (Fig. 3G; fig. S13B). We continued to track the minimal residual tumour load following DT treatment and found that while tumour cells are retained in the gastric submucosa, tumour volumes were constant with no evident signs of relapse (Fig. 3H; S13E). Critically, repeated ablation of the AQP5+ CSC pool via weekly DT administration sufficed to completely eliminate any residual tumour cells (Fig. 3I; S13F), mirroring phenotypes observed following ablation of LGR5+ cells in colon cancer models (*25*). Finally, we confirmed that orthotopic tumours derived from Aqp5-Cre/APK tumour organoids without the *Aqp5-2A-DTR* allele were unaffected by DT administration at both early and late stages of tumour growth (fig. S13, G and H). Taken together, these results identify a dependence on mouse AQP5+ tumour cells for maintaining tumour establishment and progression across both organoid and mouse models of pyloric cancer.

We then tested the effect of ablating human AQP5+ cells in a human gastric cancer organoid system. We generated human gastric cancer organoids (intestinal-subtype) expressing *AQP5-2A-iCaspase*, which harboured AQP5+ cells co-expressing an inducible Caspase9 (iCaspase9) that facilitates the selective induction of caspase-mediated cell death within AQP5+ cells upon administration of a dimerizing agent (Fig. 3J; fig. S14A). We confirmed that the *AQP5-2A-iCaspase* organoids presented comparable organoid morphology, AQP5 expression, and cell lineage marker expression with unedited tumour organoids (Fig. 3K). To ablate human AQP5+ cells, we administered the B/B homodimerizer agent to *AQP5-2A-iCaspase* human organoid cultures and confirmed a 60% loss in Aqp5 expression in treated organoids (Fig. 3, L and M). Treated *AQP5-2A-iCaspase* tumour organoids displayed significantly diminished growth rates in culture (Fig. 3, L and N), although they continued to be viable, possibly due to the remaining unablated AQP5+ cells in these cultures. Unedited tumour organoids were not affected by the treatment with B/B homodimerizer, with no significant differences in both *AQP5* levels and organoid sizes observed (fig. S14, B and C). To broaden the relevance of our findings, we repeated the ablation experiments in an independent diffuse-subtype human gastric cancer organoid line, GC10, and confirmed the specific effect of ablating AQP5+ cells on repressing organoid growth (fig. S14, D to G). Thus, like their mouse counterparts, human AQP5+ CSCs in gastric tumour organoids also promote cancer progression.

AQP5 promotes cancer traits in mouse and human models of gastric cancer

AQP5 has been implicated in driving tumour cell proliferation and migration in human gastric cancer cell lines (*18*, *26*), although its precise mechanism of action remains unclear. In gastric tumours, AQP5 is frequently expressed at elevated levels (Fig. 1, fig. S5), but the role of AQP5 in gastric cancer has not been explored in organoid and mouse models. We first probed AQP5 functions in multiple gastric cancer cell lines, extending on prior published work (*18*, *26*). The human gastric cancer cell line AGS, which is derived from an intestinal-type tumour, does not present detectable levels of AQP5 *in vitro* (fig. S15A). We generated three independent *AQP5*-overexpressing AGS cell lines with highly elevated AQP5 levels and found that they displayed significantly increased cell proliferation and cell migration rates *in vitro* over the parental line (fig. S15, A and B), in agreement with a previous study (*18*). To expand these findings to a more physiological setting, we performed orthotopic transplantation of these cell lines into the pylorus of immune-deficient mice and evaluated the resultant tumour phenotypes. In line with the *in vitro*

data, *AQP5*-overexpressing AGS intestinal-type gastric cancer cells consistently formed larger tumours than parental cells that invaded aggressively into the epithelial and muscle layers of the stomach (fig. S15C). Analysis of *AQP5* functions in a diffuse-type gastric cancer cell line, SNU601, also similarly showed elevated cell proliferation and migration rates *in vitro* across three independent *AQP5*-overexpressing cell lines (fig. S15, D and E), although these AQP5-overexpressing cells did not seed larger orthotopic tumours following transplantation (fig. S15F), highlighting potential tumour subtype-specific functions of AQP5 in driving tumourigenesis. Finally, we tested the effect of knocking out *AQP5* in the diffuse-type gastric cancer cell line KATOIII, which normally expresses high levels of *AQP5 in vitro* (fig. S15G). In line with a role for AQP5 in tumourigenesis, loss of *AQP5* in this cell line resulted in suppressed cell proliferation rates *in vitro* relative to the parental cell line (fig. S15G). Moreover, while parental KATOIII cells seeded large, invasive tumours in the gastric submucosa following orthotopic transplantation, *AQP5*-null KATOIII cells failed to establish tumours in the majority of mice analysed (fig. S15H), suggesting that AQP5 could contribute to tumour establishment. Thus, our work ties in with existing literature on AQP5 functions in promoting tumourigenic traits of cell proliferation and migration, and further extends these findings to a suite of gastric cancer cell lines using both *in vitro* and *in vivo* assays.

To explore AQP5 functions within additional *in vivo* models of gastric cancer, we next generated an *Aqp5* knockout pyloric tumour mouse model (Aqp5KO-APK) by incorporating an *Aqp5* null allele alongside the *Aqp5-eGFP-IRES-creERT2* cassette (which effectively results in inactivation of both copies of *Aqp5*). Prior to cancer induction, *Aqp5*-null mice are healthy and indistinguishable from their *Aqp5* wildtype counterparts. Following tamoxifen administration, tdTomato-traced epithelial lesions formed in these Aqp5KO-APK mice with complete absence of AQP5 expression (fig. S16, A to C). Importantly, these *Aqp5*-null lesions were significantly smaller in volume and presented pre-cancerous features of intraepithelial neoplasia, whereas *Aqp5* wildtype tumours were classified by certified pathologists as tubular-type gastric adenocarcinomas by the same timepoint (fig. S16, A and B), suggesting that AQP5 may play a role in driving tumour progression in an *in vivo* primary tumour mouse model. To replicate these findings *in vitro*, we generated *Aqp5*-null mouse pyloric tumour organoids from Aqp5KO-APK tumours and confirmed that they fail to express AQP5 (fig. S16C). In agreement with *Aqp5* knockout in native tumours, Aqp5KO-APK tumour organoids similarly formed tumours following orthotopic transplantation into immune-deficient mice that presented significantly less invasive phenotypes (fig. S16, D to F), highlighting the role of AQP5 in driving tumour progression within this gastric cancer model.

Tapping on our Aqp5KO-APK pyloric tumour mouse model, we went on to probe the underlying mechanisms driving our observed AQP5 tumour-promoting functions in this system. We utilised the GFP marker whose expression is driven by the *Aqp5* promoter to isolate the putative CSCs (GFP+) and the remaining tumour epithelial bulk (GFP-) from both *Aqp5* knockout and *Aqp5* wildtype mouse pyloric tumours by FACS and performed bulk RNA sequencing on these cells (fig. S16, G to J). This yielded a CSC signature including genes common to both *Aqp5* wildtype and knockout tumours (presumably genes unaffected by AQP5 levels) as well as differentially expressed genes unique to *Aqp5* wildtype or knockout tumours (fig. S16K; Table S5). In line with the invasive phenotypes observed in *Aqp5* wildtype tumours, we found that genes unique to *Aqp5* wildtype CSCs were enriched in gene ontology (GO) pathways associated with ECM degradation and cell membrane-ECM interactions (fig. S16, L to P), suggesting that AQP5 enriched in the CSC population could be promoting cell invasion in these tumours via ECM remodelling. Conversely, *Aqp5* knockout CSCs presented a transcriptomic profile devoid of ECM-associated pathways but instead enriched in neuronal regulation via GABA receptors and voltage-

gated ion channels (fig. S16M), reflecting potential tumour-neuronal crosstalk in these neoplastic tissues. Taken together, our profiling efforts reveal that AQP5 not only marks gastric CSCs but may also play a function in activating ECM remodelling pathways to drive tumour invasion within primary mouse pyloric tumours.

To expand our findings to a more complex human gastric cancer system, we finally probed AQP5 functions in human gastric cancer organoids. We confirmed AQP5 expression in human intestinal-type gastric cancer organoids and successfully established four independent *AQP5* knockout organoid clones from the same parental line (Fig. 4A). All four *AQP5*-null organoid lines reproducibly showed markedly lower rates of proliferation *in vitro* relative to the *AQP5* wildtype parental organoid line (Fig. 4, A and B) and established smaller tumours following orthotopic transplantation into mice that were frequently less invasive (Fig. 4, C and D), in line with our primary tumour and mouse organoid data (fig. S15 and 16). Conversely, overexpression of *AQP5* was sufficient to promote cell proliferation *in vitro* in two additional human gastric cancer organoid lines (Fig. 4, E and F; fig. S17A). Following orthotopic transplantation, *AQP5*-overexpressing human intestinal-type gastric tumour organoids established larger tumours that were also more invasive *in vivo* (Fig. 4, G and H), but these tumour differences were less evident in an organoid line displaying diffuse-type phenotypes (fig. S17B), indicative of context-specific cancer-promoting functions of AQP5 in line with our earlier analysis of tumour phenotypes in human gastric cancer cell lines.

Lastly, to dissect the specific mechanisms driving AQP5 functions in human gastric cancer, we generated human organoids amenable to conditional knockout of *AQP5* based on the FLIP-Puro system (*27*) (fig. S17, C and D). In contrast to our Aqp5KO-APK mouse model, which allowed us to model the long-term consequences of *Aqp5* loss *in vivo*, the shorter-term conditional *AQP5* knockout human organoid system could be exploited to perform targeted exploration of immediate phenotypic and molecular changes following *AQP5* loss. In this system, administration of Cre recombinase gesicles results in altered exon splicing that generates a truncated, non-functional AQP5 product (fig. S17C). We confirmed that Cre gesicle-treated human organoids no longer expressed *AQP5* and displayed significantly reduced growth in culture (fig. S17, E and F), concurring with the phenotypes observed from our constitutive *AQP5* knockout human organoid lines (Fig. 4, A and B). We then performed bulk RNAseq on *AQP5 FLIP-Puro* organoids at 12h, 24h, 2d and 5d timepoints immediately following Cre recombination in both treated and untreated organoids and analysed differentially expressed genes in these organoids over time (fig. S17F; Table S6). GO pathway analyses revealed the downregulation of WNT, PI3K, and p38MAPK pathways at the earliest timepoints (12h and 24h) immediately following conditional loss of *AQP5* (fig. S17G), suggesting that these pathways could be functioning downstream of AQP5.

To test this hypothesis, we first analysed pathway activity in *AQP5* knockout and *AQP5*-overexpressing organoid lines. *AQP5* knockout organoids consistently displayed reduced pAKT (Fig. 4I), pMAPK (Fig. 4J), and multiple WNT target genes including *MYC* and *CCND1* (Fig. 4, K and L; fig. S18A), indicative of reduced activation of PI3K, MAPK, and WNT pathways respectively. Conversely, organoids overexpressing *AQP5* displayed the opposite characteristics (fig. S18, B and C). We then perturbed each of these pathways individually and found that these singular treatments were sufficient to reduce organoid growth (Fig. 4, M and N; fig. S18, D and E), an effect that was further enhanced with combined treatment of multiple inhibitors to reach levels comparable to *AQP5* knockout in these organoids (Fig. 4O). Importantly, we did not observe significant changes in organoid growth when the same inhibitors were used on *AQP5* knockout organoids (fig. S18F), indicating that the phenotypes observed were specific to AQP5 expression.

Finally, we overexpressed constitutively active WNT and PI3K mutants in *AQP5* knockout organoids and found that this was sufficient to significantly rescue the changes in organoid proliferation (fig. S18, G and H), supporting the role of these pathways downstream of AQP5 in driving cancer growth.

AQP5+ cells are functional CSCs in metastatic gastric cancer

We finally explored the role of AQP5+ CSCs within metastatic gastric tumours. To date, few genetic mouse models of gastric cancer recapitulate metastasis, with mice frequently succumbing early on due to tumour loads in other organs, such as highly aggressive intestinal tumours that form in Lgr5-CreERT2 driven models of cancer (*28*). Cldn18-CreERT2 driven systems were previously shown to support metastatic spread to multiple organs in a model of corpus cancer (*29*), but a pylorus-specific model has not yet been established. Given the advantages of our Aqp5-CreERT2 driven model in specifically targeting mutations to the pyloric stem cell compartment, we explored the potential of modelling advanced stages of pyloric cancer , including metastatic spread. While induced Aqp5-Cre/APK mice developed adenocarcinomas after 10 weeks (Fig. 1B), mice continued to be viable 8 months after induction, at which point metastatic spread to the lungs and liver could be observed (Fig. 5A). We validated the gastric origin of the metastatic cancer cells that disseminated to the lungs and liver (fig. S19, A and B), and documented AQP5 expression across all the cancer compartments in a subset of metastatic cancer cells (Fig. 5A). To accelerate the development of these metastatic cancers, we generated a second orthotopic pyloric cancer mouse model from transplantation of pyloric cancer organoids, which rapidly yielded lung and liver metastases within 2 months (Fig. 5B). The orthotopic model was able to recapitulate patterns of expression observed in the primary metastatic models (Fig. 5, B and C; fig. S19, C and D).

We used these liver metastases to establish long-lived metastatic organoid cultures, from which we could isolate by FACS the AQP5+ and AQP5- populations for analysis. We confirmed that metastatic AQP5+ cells were able to initiate organoid outgrowth much more efficiently than their AQP5- counterparts (Fig. 5D), suggesting that AQP5+ cells from metastatic tumours also function as a CSC population. To test a role for AQP5 itself in promoting metastatic progression, we finally explored long-term phenotypic changes in xenografts derived from parental and *AQP5* knockout human gastric cancer organoids (Fig. 5E). While parental organoids established adenocarcinomas that invaded through the mucosal epithelium and disseminated deeply through the muscularis propria, serosa, and surrounding liver and pancreatic tissues (tumour stage T4), AQP5-null organoids were retained within the submucosal space with minimal invasion into the other tissue layers (tumour stage T1 and T2), as assessed by an animal pathologist (Fig. 5, E and F). Therefore, in addition to their roles in the primary pyloric tumour, AQP5+ cancer cells likely also serve as functional CSCs within the metastatic setting.

Taken together, through our analyses of multiple gastric cancer models, we propose AQP5 as a functionally validated mouse and human gastric CSC marker that promotes tumour progression and metastasis.

Discussion

The CSC model links clinical observations of chemoresistance and tumour relapse to the activity of a pool of stem cells in fuelling continued tumour growth, which offers an attractive target that

can be harnessed for therapeutic use. CSCs were first identified in blood cancers (*30*, *31*) and later also defined in brain (*32*) and colon (*33*, *34*) cancers, but the presence of such a CSC pool within gastric tumours has yet to be directly proven. This is potentially related to technical challenges involved in isolating, culturing, and transplantation of primary gastric tumour cells, using methods originally established in blood cancers that provide a direct readout of stem cell potential but has proven more challenging to adapt for solid tumours (*22*). As a result, prior studies have primarily relied on associations with other established pluripotency markers such as SOX2 (*8*) and NANOG (*35*) to define CSC populations or used gastric cancer cell line models that have already undergone major cellular transformation in culture to identify putative CSC populations, such as those marked by CD44 (*5*–*7*). However, the clinical relevance and impact of these findings remain limited without a direct assessment of CSC potential in primary human tumours or more physiologically relevant models.

Our study addresses these issues by firstly establishing techniques to enrich, isolate, and culture primary AQP5+ cancer cells from both mouse and human gastric tumour tissues, and secondly by developing a strategy to orthotopically transplant these cells into the stomachs of immune-deficient mice to evaluate their tumour outgrowth capacity. These technical advancements have enabled us to derive a comprehensive transcriptomic profile of mouse and human AQP5+ gastric CSCs and also establish via multiple complementary approaches encompassing organoid initiation, orthotopic transplantation, and lineage tracing assays the stem potential exhibited by this tumour cell population over their AQP5- counterparts, allowing us to define a functional gastric CSC population. In contrast to previously proposed stem cell markers with broad expression across multiple tissue compartments and/or lack cell surface expression, the specific membranous AQP5 expression within both the mouse and human gastric CSC compartment also renders it uniquely compatible with FACS isolation approaches for downstream functional studies.

Selective ablation of mouse and human AQP5+ cells was sufficient to block pyloric tumour initiation and growth, reinforcing the contribution of AQP5+ cells as a CSC pool maintaining cancer progression. Interestingly, immediately following ablation of AQP5+ cells, we observed a distinct proliferative response in the surviving AQP5- tumour load. When tracked to later timepoints, ablated tumours retain tumour remnants within the tissue, but even this minor population can be fully eliminated with sustained ablation of AQP5+ cells. Hence, loss of AQP5+ CSCs likely drives a tumour plasticity response within the remaining AQP5- pool to upregulate AQP5 expression, supporting the survival of a small population of tumour cells within the tissue. This is reminiscent of phenotypes observed following LGR5+ CSC ablation in colon cancer models, where the LGR5- cells continuously re-express LGR5 to maintain the tumour load (*25*). Therefore, while our data supports the CSC potential within the AQP5+ population in gastric tumours, we note that AQP5- cells retain the ability to activate AQP5 expression and tumour plasticity mechanisms under specific situations, such as in response to targeted killing of CSCs.

To establish the broader relevance of our findings, we tested the role of AQP5+ CSCs across multiple gastric cancer contexts in this study, including cell lines, organoids, and xenograft/primary mouse models, which showed a strong concurrence in the main conclusions of this study. Despite our best efforts, it was not possible to perform an exhaustive evaluation of AQP5+ cells across all available models of gastric cancer. Thus, while a range of primary human samples as well as three independent mouse models collectively identified AQP5 as a CSC marker, we cannot exclude the possibility that alternative models, such as those originating from non-AQP5-expressing cell types or from other stomach regions like the corpus, could give rise to

tumours with a different CSC population. Indeed, LGR5 was previously proposed to mark stem-like populations in mouse corpus cancer models (*29*). In our pyloric cancer models, we instead find that cells expressing the highest levels of AQP5 are primarily enriched within the MUC6+ epithelial cell cluster largely distinct from LGR5, although a smaller subset show overlapping expression of both markers. An important area of future investigation would therefore be to tease apart contributions of AQP5-expressing epithelial subsets, including cells co-expressing both AQP5 and LGR5, across a variety of cancer contexts. Our functional characterization of AQP5+ cells in pyloric cancer models indicate that while LGR5 could function as CSCs in the corpus, AQP5 may represent a more relevant CSC marker in the pyloric region of the stomach, hinting at the potential role of microenvironmental influences in regulating CSC activity.

In terms of its functions, AQP5 is traditionally known as a water channel protein. AQP5 expression has recently been associated with a number of human cancers (*36*, *37*), but its role within a cancer context remains poorly understood. It has been suggested that AQP5 may promote increased tumour cell proliferation and migration via the Ras signalling pathway in NIH3T3 cells (*38*) and the colorectal cancer cell line HCT116 (*37*), along with the potential involvement of ERK signalling shown in H1299, a non-small cell lung cancer cell line (*39*). More recently, ERK signalling was also proposed to function downstream of AQP5 in a *H. pylori* infection gastric cancer cell line model to drive EMT phenotypes (*26*). However, there continues to be a limited exploration of AQP5 functions within more physiologically relevant gastric cancer models. In contrast to previous studies, we established methods to perturb AQP5 expression not only in cell lines but also across multiple human gastric cancer organoid and mouse models. We find that AQP5 is dispensable for epithelial homeostasis in the healthy stomach but plays a cancer-specific role in promoting increased cell proliferation, migration, and invasion via WNT, PI3K, and MAPK signalling, providing a mechanistic link between AQP5 and its tumour-promoting functions.

Finally, we demonstrate AQP5+ cells as functional CSCs in metastatic gastric cancers, extending beyond the primary cancer context. We established a new genetic mouse model of metastatic pyloric cancer with extensive dissemination to the liver and lungs, from which we were able to evaluate AQP5+ CSCs and their functions in the metastatic setting. Given that most genetic mouse models of gastric cancer capture only the early stages of tumour progression, our pyloric cancer model may represent one of the few capable of recapitulating advanced disease and metastatic spread. Moreover, while CSCs have frequently been associated with metastasis, the contribution of CSCs in metastatic gastric tumours has remained unclear. Our establishment of a functional AQP5+ CSC population in these disseminated tumours now sets the stage for a wider exploration of CSC-driven mechanisms across primary and metastatic contexts.

References and Notes

1. E. Batlle, H. Clevers, Cancer stem cells revisited. *Nature Medicine* **23**, 1124–1134 (2017).

2. D. Nassar, C. Blanpain, Cancer Stem Cells: Basic Concepts and Therapeutic Implications. *Annual Review of Pathology: Mechanisms of Disease* **11**, 47–76 (2016).

3. F. Bray, M. Laversanne, H. Sung, J. Ferlay, R. L. Siegel, I. Soerjomataram, A. Jemal, Global cancer statistics 2022: GLOBOCAN estimates of incidence and mortality worldwide for 36 cancers in 185 countries. *CA A Cancer J Clinicians* **74**, 229–263 (2024).

4. M. Alsina, V. Arrazubi, M. Diez, J. Tabernero, Current developments in gastric cancer: from molecular profiling to treatment strategy. *Nat Rev Gastroenterol Hepatol* **20**, 155–170 (2023).

5. S. Takaishi, T. Okumura, S. Tu, S. S. W. Wang, W. Shibata, R. Vigneshwaran, S. A. K. Gordon, Y. Shimada, T. C. Wang, Identification of Gastric Cancer Stem Cells Using the Cell Surface Marker CD44. *Stem Cells* **27**, 1006–1020 (2009).

6. W. M. Lau, E. Teng, H. S. Chong, K. A. P. Lopez, A. Y. L. Tay, M. Salto-Tellez, A. Shabbir, J. B. Y. So, S. L. Chan, CD44v8-10 Is a Cancer-Specific Marker for Gastric Cancer Stem Cells. *Cancer Research* **74**, 2630–2641 (2014).

7. C. Zhang, C. Li, F. He, Y. Cai, H. Yang, Identification of CD44+CD24+ gastric cancer stem cells. *Journal of Cancer Research and Clinical Oncology* **137**, 1679–1686 (2011).

8. D. Pádua, R. Barros, A. L. Amaral, P. Mesquita, A. F. Freire, M. Sousa, A. F. Maia, I. Caiado, H. Fernandes, A. Pombinho, C. F. Pereira, R. Almeida, A SOX2 Reporter System Identifies Gastric Cancer Stem-Like Cells Sensitive to Monensin. *Cancers* **12**, 495 (2020).

9. S. H. Tan, Y. Swathi, S. Tan, J. Goh, R. Seishima, K. Murakami, M. Oshima, T. Tsuji, P. Phuah, L. T. Tan, E. Wong, A. Fatehullah, T. Sheng, S. W. T. Ho, H. I. Grabsch, S. Srivastava, M. Teh, S. L. I. J. Denil, S. Mustafah, P. Tan, A. Shabbir, J. So, K. G. Yeoh, N. Barker, AQP5 enriches for stem cells and cancer origins in the distal stomach. *Nature* **578**, 437–443 (2020).

10. S. A. Mani, W. Guo, M.-J. Liao, E. Ng. Eaton, A. Ayyanan, A. Y. Zhou, M. Brooks, F. Reinhard, C. C. Zhang, M. Shipitsin, L. L. Campbell, K. Polyak, C. Brisken, J. Yang, R. A. Weinberg, The Epithelial-Mesenchymal Transition Generates Cells with Properties of Stem Cells. *Cell* **133**, 704–715 (2008).

11. X. Ye, W. L. Tam, T. Shibue, Y. Kaygusuz, F. Reinhardt, E. Ng Eaton, R. A. Weinberg, Distinct EMT programs control normal mammary stem cells and tumour-initiating cells. *Nature* **525**, 256–260 (2015).

12. S. Bao, Q. Wu, R. E. McLendon, Y. Hao, Q. Shi, A. B. Hjelmeland, M. W. Dewhirst, D. D. Bigner, J. N. Rich, Glioma stem cells promote radioresistance by preferential activation of the DNA damage response. *Nature* **444**, 756–760 (2006).

13. M. Diehn, R. W. Cho, N. A. Lobo, T. Kalisky, M. J. Dorie, A. N. Kulp, D. Qian, J. S. Lam, L. E. Ailles, M. Wong, B. Joshua, M. J. Kaplan, I. Wapnir, F. M. Dirbas, G. Somlo, C. Garberoglio, B. Paz, J. Shen, S. K. Lau, S. R. Quake, J. M. Brown, I. L. Weissman, M. F. Clarke, Association of reactive oxygen species levels and radioresistance in cancer stem cells. *Nature* **458**, 780–783 (2009).

14. V. Kumar, K. Ramnarayanan, R. Sundar, N. Padmanabhan, S. Srivastava, M. Koiwa, T. Yasuda, V. Koh, K. K. Huang, S. T. Tay, S. W. T. Ho, A. L. K. Tan, T. Ishimoto, G. Kim, A. Shabbir, Q. Chen, B. Zhang, S. Xu, K.-P. Lam, H. Y. J. Lum, M. Teh, W. P. Yong, J. B. Y. So, P. Tan, Single-Cell Atlas of Lineage States, Tumor Microenvironment, and Subtype-Specific Expression Programs in Gastric Cancer. *Cancer Discovery* **12**, 670–691 (2022).

15. J. Kim, C. Park, K. H. Kim, E. H. Kim, H. Kim, J. K. Woo, J. K. Seong, K. T. Nam, Y. C. Lee, S. Y. Cho, Single-cell analysis of gastric pre-cancerous and cancer lesions reveals cell lineage diversity and intratumoral heterogeneity. *npj Precis. Onc.* **6**, 9 (2022).

16. T. Watanabe, T. Fujii, T. Oya, N. Horikawa, Y. Tabuchi, Y. Takahashi, M. Morii, N. Takeguchi, K. Tsukada, H. Sakai, Involvement of aquaporin-5 in differentiation of human gastric cancer cells. *The Journal of Physiological Sciences* **59**, 113–122 (2009).

17. L. Shen, Z. Zhu, Y. Huang, Y. Shu, M. Sun, H. Xu, G. Zhang, R. Guo, W. Wei, W. Wu, Expression profile of multiple aquaporins in human gastric carcinoma and its clinical significance. *Biomedicine & Pharmacotherapy* **64**, 313–318 (2010).

18. Y.-H. Huang, X.-Y. Zhou, H.-M. Wang, H. Xu, J. Chen, N.-H. Lv, Aquaporin 5 promotes the proliferation and migration of human gastric carcinoma cells. *Tumor Biology* **34**, 1743–1751 (2013).

19. W.-T. Kim, C. J. Ryu, Cancer stem cell surface markers on normal stem cells. *BMB Rep.* **50**, 285–298 (2017).

20. S. Nishikawa, M. Konno, A. Hamabe, S. Hasegawa, Y. Kano, K. Ohta, T. Fukusumi, D. Sakai, T. Kudo, N. Haraguchi, T. Satoh, S. Takiguchi, M. Mori, Y. Doki, H. Ishii, Aldehyde dehydrogenasehigh gastric cancer stem cells are resistant to chemotherapy. *International Journal of Oncology* **42**, 1437–1442 (2013).

21. A. Fatehullah, Y. Terakado, S. Sagiraju, T. L. Tan, T. Sheng, S. H. Tan, K. Murakami, Y. Swathi, N. Ang, R. Rajarethinam, T. Ming, P. Tan, B. Lee, N. Barker, A tumour-resident Lgr5+ stem-cell-like pool drives the establishment and progression of advanced gastric cancers. *Nat Cell Biol* **23**, 1299–1313 (2021).

22. J. E. Visvader, G. J. Lindeman, Cancer stem cells in solid tumours: accumulating evidence and unresolved questions. *Nat Rev Cancer* **8**, 755–768 (2008).

23. P. Tan, K.-G. Yeoh, Genetics and Molecular Pathogenesis of Gastric Adenocarcinoma. *Gastroenterology* **149**, 1153-1162.e3 (2015).

24. C. Holohan, S. Van Schaeybroeck, D. B. Longley, P. G. Johnston, Cancer drug resistance: an evolving paradigm. *Nat Rev Cancer* **13**, 714–726 (2013).

25. F. De Sousa E Melo, A. V. Kurtova, J. M. Harnoss, N. Kljavin, J. D. Hoeck, J. Hung, J. E. Anderson, E. E. Storm, Z. Modrusan, H. Koeppen, G. J. P. Dijkgraaf, R. Piskol, F. J. De Sauvage, A distinct role for Lgr5+ stem cells in primary and metastatic colon cancer. *Nature* **543**, 676–680 (2017).

26. N. Li, X. Xu, H. Yang, H. Wang, Y. Ouyang, Y. Zhou, C. Peng, Z. Yuan, C. He, C. Zeng, J. Hong, Activation of Aquaporin 5 by carcinogenic Helicobacter pylori infection promotes epithelial-mesenchymal transition via the MEK/ERK pathway. *Helicobacter* **26** (2021).

27. A. Andersson-Rolf, R. C. Mustata, A. Merenda, J. Kim, S. Perera, T. Grego, K. Andrews, K. Tremble, J. C. R. Silva, J. Fink, W. C. Skarnes, B.-K. Koo, One-step generation of conditional and reversible gene knockouts. *Nat Methods* **14**, 287–289 (2017).

28. N. Barker, R. A. Ridgway, J. H. van Es, M. van de Wetering, H. Begthel, M. van den Born, E. Danenberg, A. R. Clarke, O. J. Sansom, H. Clevers, Crypt stem cells as the cells-of-origin of intestinal cancer. *Nature* **457**, 608–611 (2009).

29. A. Fatehullah, Y. Terakado, S. Sagiraju, T. L. Tan, T. Sheng, S. H. Tan, K. Murakami, Y. Swathi, N. Ang, R. Rajarethinam, T. Ming, P. Tan, B. Lee, N. Barker, A tumour-resident Lgr5+ stem-cell-like pool drives the establishment and progression of advanced gastric cancers. *Nat Cell Biol* **23**, 1299–1313 (2021).

30. T. Lapidot, C. Sirard, J. Vormoor, B. Murdoch, T. Hoang, J. Caceres-Cortes, M. Minden, B. Paterson, M. A. Caligiuri, J. E. Dick, A cell initiating human acute myeloid leukaemia after transplantation into SCID mice. *Nature* **367**, 645–648 (1994).

31. D. Bonnet, J. E. Dick, Human acute myeloid leukemia is organized as a hierarchy that originates from a primitive hematopoietic cell. *Nature Medicine* **3**, 730–737 (1997).

32. S. K. Singh, C. Hawkins, I. D. Clarke, J. A. Squire, J. Bayani, T. Hide, R. M. Henkelman, M. D. Cusimano, P. B. Dirks, Identification of human brain tumour initiating cells. *Nature* **432**, 396–401 (2004).

33. C. A. O'Brien, A. Pollett, S. Gallinger, J. E. Dick, A human colon cancer cell capable of initiating tumour growth in immunodeficient mice. *Nature* **445**, 106–110 (2007).

34. L. Ricci-Vitiani, D. G. Lombardi, E. Pilozzi, M. Biffoni, M. Todaro, C. Peschle, R. De Maria, Identification and expansion of human colon-cancer-initiating cells. *Nature* **445**, 111–115 (2007).

35. X. Ma, B. Wang, X. Wang, Y. Luo, W. Fan, NANOGP8 is the key regulator of stemness, EMT, Wnt pathway, chemoresistance, and other malignant phenotypes in gastric cancer cells. *PLoS ONE* **13**, e0192436 (2018).

36. H. J. Jung, J.-Y. Park, H.-S. Jeon, T.-H. Kwon, Aquaporin-5: A Marker Protein for Proliferation and Migration of Human Breast Cancer Cells. *PLoS ONE* **6**, e28492 (2011).

37. S. K. Kang, Y. K. Chae, J. Woo, M. S. Kim, J. C. Park, J. Lee, J. C. Soria, S. J. Jang, D. Sidransky, C. Moon, Role of Human Aquaporin 5 In Colorectal Carcinogenesis. *The American Journal of Pathology* **173**, 518–525 (2008).

38. J. Woo, J. Lee, M. S. Kim, S. J. Jang, D. Sidransky, C. Moon, The effect of aquaporin 5 overexpression on the Ras signaling pathway. *Biochemical and Biophysical Research Communications* **367**, 291–298 (2008).

39. A. Elkhider, B. Wang, X. Ouyang, M. Al-Azab, W. Walana, X. Sun, H. Li, Y. Tang, J. Wei, X. Li, Aquaporin 5 promotes tumor migration and angiogenesis in non-small cell lung cancer cell line H1299. *Oncol Lett* **19**, 1665–1672 (2020).

Acknowledgments: The authors extend their gratitude towards the surgical team (A Shabbir, G Kim, D Chia, and JBY So), clinical research coordinators (A Pang, C Yap, K Lynn, and R Liew) of the Department of Surgery, and staff at the Department of Pathology, National University Hospital, Singapore for assistance with the collection of patient tumour biopsy samples, I. Low and B. Ng from the FACS facility at the Singapore Immunology Network (SIgN, A*STAR) for help with cell sorting, R. Rajarethinam from the Advanced Molecular Pathology Laboratory (AMPL, A*STAR) and senior consultant S.Y. Tan from the National University Hospital Singapore (NUHS) for pathology evaluation of H&E stained slides, staff at the IMCB-Central Imaging Facility and SBIC-Nikon Imaging Centre for assistance with imaging needs, and H. Clevers and members of the Barker lab for critical reading of the manuscript.

Funding:

Agency for Science, Technology and Research (NB)

Institute of Molecular and Cell Biology (NB, HYGL)

Singapore Ministry of Health's National Medical Research Council Open Fund-Individual Research Grant OFIRG19may-0069 (NB)

Singapore Ministry of Health's National Medical Research Council Open Fund-Young Individual Research Grant OFYIRG22jul-0006 (HYGL)

Agency for Science, Technology and Research Target Translation Consortium Grant TTC2019_002 (NB)

Author contributions:

Conceptualization: HYGL, SY, SHT, NB

Formal analysis: BTKL, KKK, NSBR, MPR

Funding acquisition: HYGL, NB

Investigation: HYGL, SY, KM, SS, PP, TCC, FBA, KBAM, SK, LTT, SM

Resources: KM, JBYS

Supervision: HYGL, NB

Writing – original draft: HYGL

Writing – review & editing: HYGL, SY, SHT, NB

Competing interests: HYGL, SY, SHT, and NB are listed as inventors on patent application (PCT/SG2024/050154) submitted by the Agency for Science, Technology and Research (A*STAR) that covers the use of AQP5 in cancer detection and therapeutics.

Data and materials availability: All data are available in the main text or the supplementary materials. The sequencing data reported in this paper can be found in the Gene Expression Omnibus database under accession numbers GSE265919, GSE265920, and GSE266551.

Supplementary Materials

Materials and Methods

Figs. S1 to S19

Tables S1 to S7

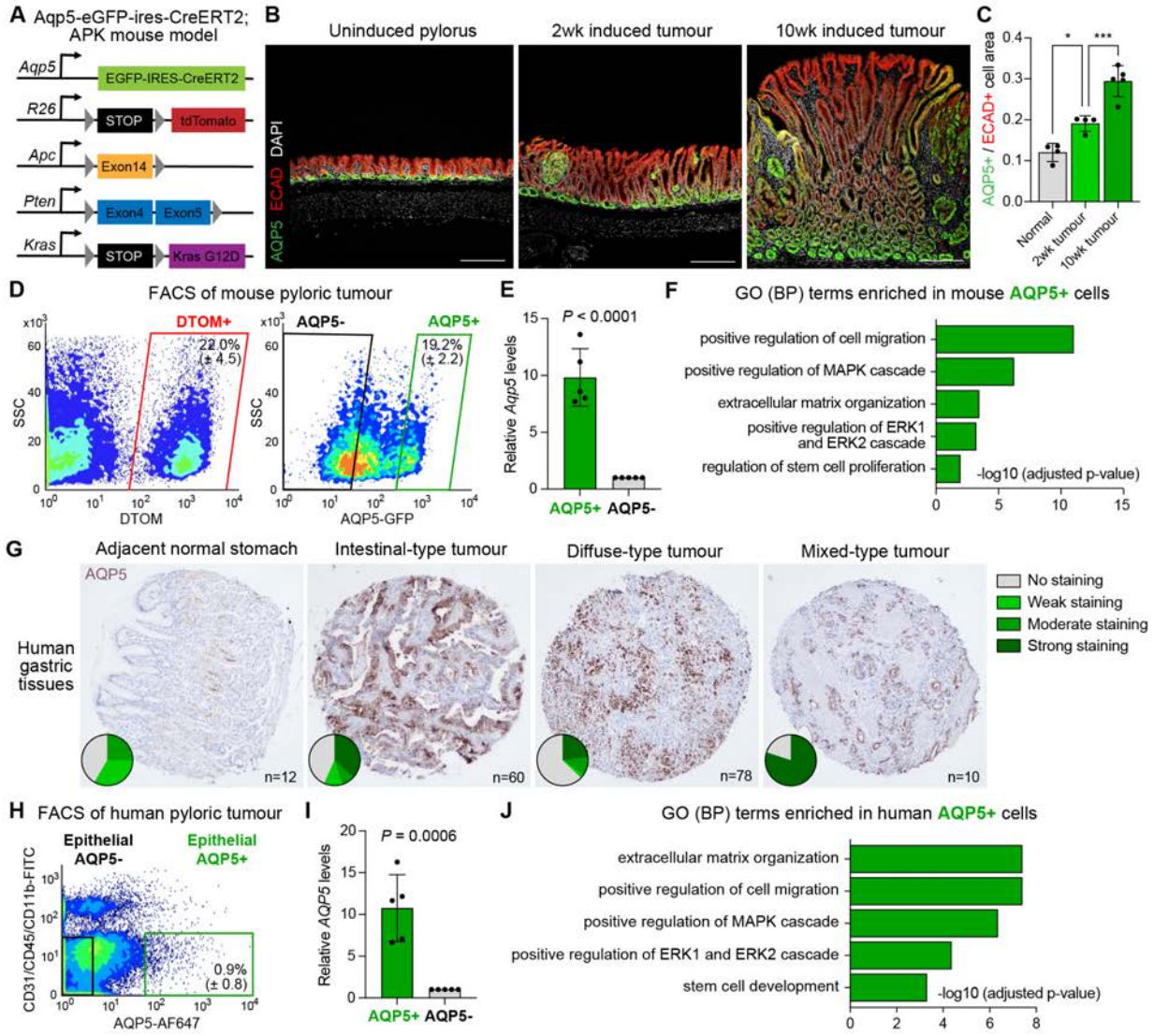

Fig. 1. AQP5 is overexpressed in a distinct subpopulation of mouse and human pyloric tumours that display properties of cancer stem cells. (**A**) Alleles present in the *Aqp5-eGFP-ires-CreERT2; Apc*$^{fl/fl}$*; Pten*$^{fl/fl}$*; Kras*$^{LSL\text{-}G12D/+}$*; Rosa26-tdTomato*^{LSL} conditional genetic mouse model for pyloric cancer (Aqp5-Cre/APK in short). Upon tamoxifen administration, Cre recombinase is activated to drive recombination at the indicated loxP sites (grey triangles), resulting in tdTomato reporter expression and mutations in *Apc*, *Pten*, and *Kras* driving Wnt, PI3K, and Ras pathway hyperactivation respectively. (**B**) AQP5 expression in the pylorus across multiple stages of tumour development in the Aqp5-Cre/APK mouse model. n = 4 biological replicates; scale bars, 200μm. (**C**) Quantification of the changes in proportion of AQP5+ cells within the healthy and tumour pyloric epithelium (ECAD+ cells) over time. Statistical analysis was performed using one-way ANOVA with Tukey's multiple comparisons test. *P = 0.0154, ***P = 0.0009. (**D**) FACS gating strategy for isolation of tumour epithelial (DTOM+) AQP5- and AQP5+ cells from primary mouse pyloric tumours. SSC, side scatter. n = 5 biological replicates. (**E**) Relative *Aqp5* expression in sorted mouse tumour cell populations by qPCR. (**F**) Selected gene ontology (GO) terms from the biological process (BP) category significantly enriched in the transcriptome of mouse pyloric tumour AQP5+ cells compared to AQP5- cells. The x-axis shows

the negative log10 transform of the adjusted *P* values. (**G**) AQP5 expression in human gastric tissue microarrays of the normal stomach, intestinal-type gastric tumours, diffuse-type gastric tumours, and mixed-type gastric tumours. Degree of staining was scored on a scale ranging from absence of staining to strong staining as indicated in the legend (right). Pie charts show the proportion of analysed cores displaying the indicated levels of staining. Images shown are representative of tissue cores presenting moderate staining in the normal stomach and strong staining in the tumour tissues. (**H**) FACS gating strategy for isolation of tumour epithelial AQP5- and AQP5+ cells from primary human pyloric tumour biopsies. SSC, side scatter. $n = 5$ biological replicates. (**I**) Relative *AQP5* expression in sorted human tumour cell populations by qPCR. (**J**) Selected gene ontology (GO) terms from the biological process (BP) category significantly enriched in the transcriptome of human pyloric tumour AQP5+ cells compared to AQP5- cells. Graphs represent mean ± S.D. with two-tailed unpaired *t*-test unless otherwise specified.

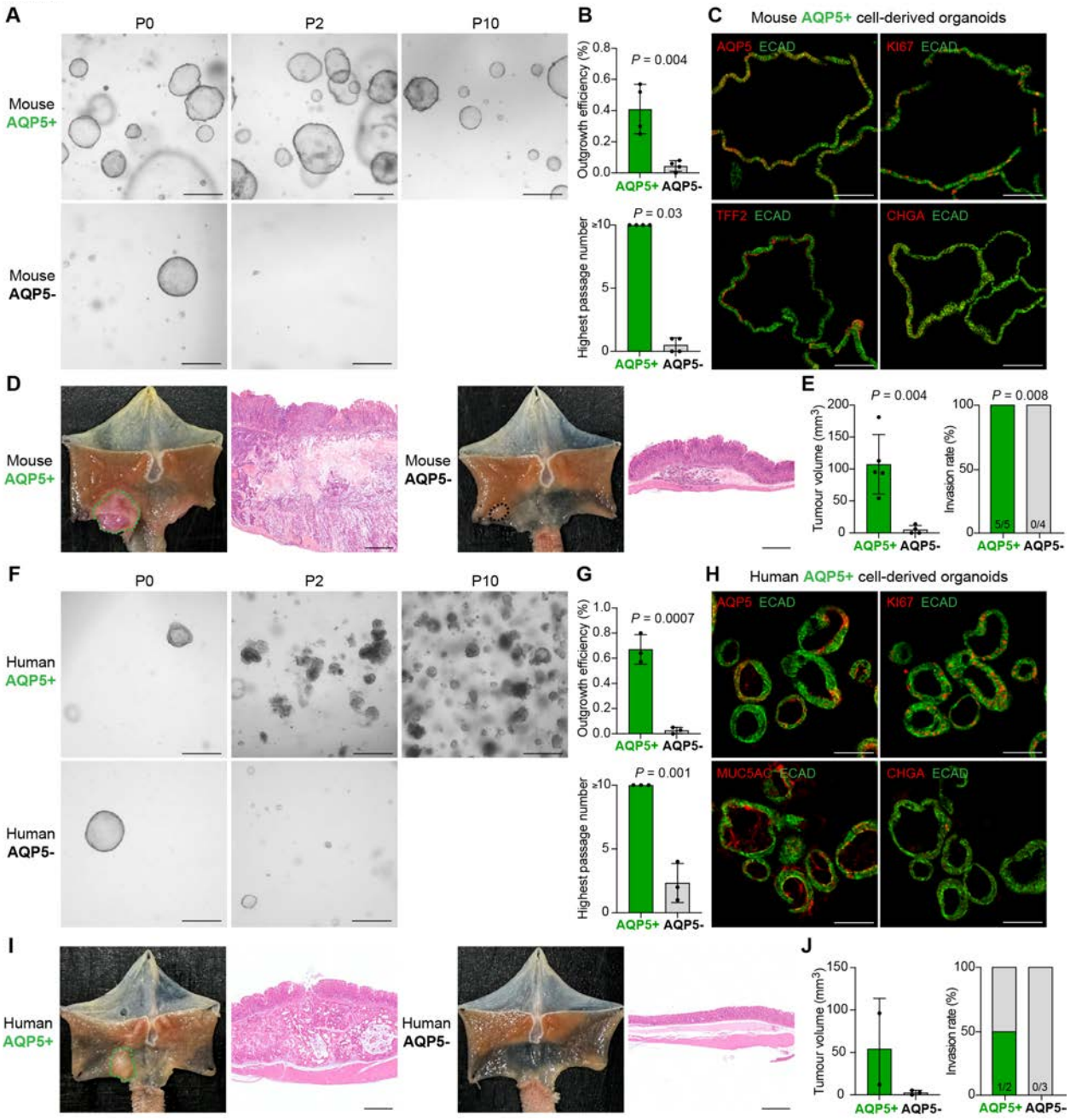

Fig. 2. Mouse and human AQP5+ pyloric tumour cells display functions of cancer stem cells. (**A**) Organoids generated from single FACS-sorted mouse AQP5+ and AQP5- cells at passages 0, 2, and 10. Mouse AQP5+ cell-derived organoids maintain high outgrowth efficiency until at least P10, while the small number of AQP5- cell-derived organoids that form fail to survive beyond P2. n = 4 biological replicates; scale bars, 500µm. (**B**) Organoid outgrowth efficiency of mouse AQP5+ and AQP5- cells at P0 and quantification of highest passage number reached for each culture. The latter dataset was analysed with a Mann-Whitney U-test. (**C**) Expression of AQP5 and differentiated lineage markers KI67, TFF2, and CHGA in mouse AQP5+ cell-derived organoids. n = 3 biological replicates; scale bars, 100µm. (**D**) Whole mount and H&E images of tumours generated from transplanted mouse AQP5+ (left) and AQP5- (right) pyloric tumour cells. Orthotopic tumour outlines are indicated in dotted lines in the whole mount images. n = 4

biological replicates; scale bars, 1mm. (**E**) Quantification of tumour volumes (left) and invasion rates (right) of tumours derived from transplanted AQP5+ and AQP5- pyloric tumour cells. Invasion rate was analysed using the Fisher's exact test. (**F**) Organoids generated from single FACS-sorted human AQP5+ and AQP5- cells at passages 0, 2, and 10. Human AQP5+ cell-derived organoids maintain high outgrowth efficiency until at least P10, while the small number of AQP5- cell-derived organoids fail to survive beyond a few passages. n = 3 biological replicates; scale bars, 500μm. (**G**) Organoid outgrowth efficiency of human AQP5+ and AQP5- cells at P2 and quantification of highest passage number reached for each culture. (**H**) Expression of AQP5 and differentiated lineage markers KI67, MUC5AC, and CHGA in human AQP5+ cell-derived organoids. n = 3 biological replicates; scale bars, 100μm. (**I**) Whole mount and H&E images of tumours generated from transplanted human AQP5+ (left) and AQP5- (right) pyloric tumour cells. Orthotopic tumour outlines are indicated in dotted lines in the whole mount images. n = 3 biological replicates; scale bars, 1mm. (**J**) Quantification of tumour volumes (left) and invasion rates (right) of tumours derived from transplanted AQP5+ and AQP5- pyloric tumour cells. Graphs represent mean ± S.D. with two-tailed unpaired t-test unless otherwise specified.

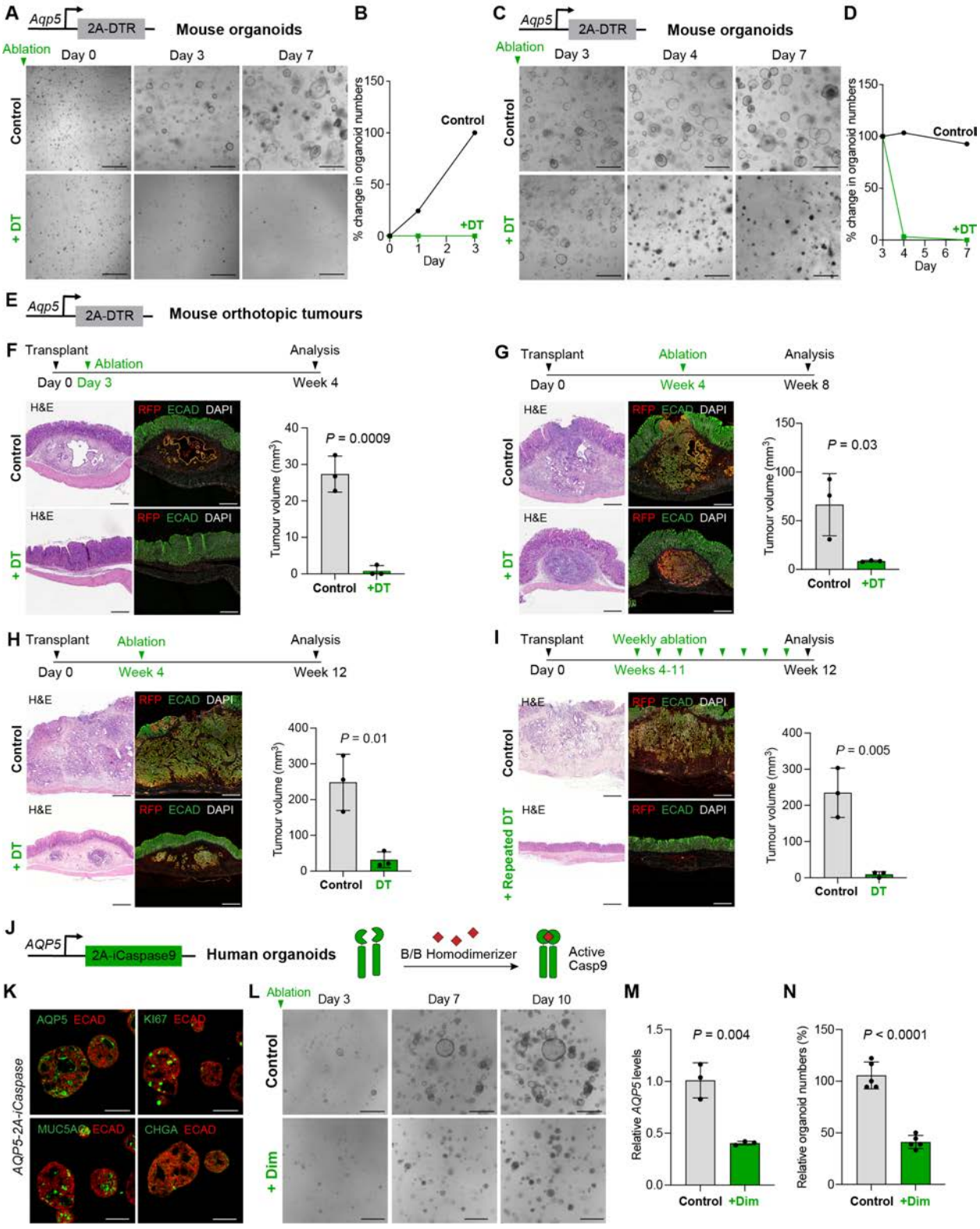
A
Aqp5
2A-DTR
Mouse organoids
Ablation
Day 0
Day 3
Day 7
Control
+ DT
B
% change in organoid numbers
Control
+DT
Day
C
Aqp5
2A-DTR
Mouse organoids
Ablation
Day 3
Day 4
Day 7
Control
+ DT
D
% change in organoid numbers
Control
+DT
Day
E
Aqp5
2A-DTR
Mouse orthotopic tumours
F
Transplant
Ablation
Analysis
Day 0 Day 3
Week 4
H&E
RFP ECAD DAPI
Control
+ DT
Tumour volume (mm3)
P = 0.0009
Control
+DT
G
Transplant
Ablation
Analysis
Day 0
Week 4
Week 8
H&E
RFP ECAD DAPI
Control
+ DT
Tumour volume (mm3)
P = 0.03
Control
+DT
H
Transplant
Ablation
Analysis
Day 0
Week 4
Week 12
H&E
RFP ECAD DAPI
Control
+ DT
Tumour volume (mm3)
P = 0.01
Control
DT
I
Transplant
Weekly ablation
Analysis
Day 0
Weeks 4-11
Week 12
H&E
RFP ECAD DAPI
Control
+ Repeated DT
Tumour volume (mm3)
P = 0.005
Control
DT
J
AQP5
2A-iCaspase9
Human organoids
B/B Homodimerizer
Active Casp9
K
AQP5 ECAD
KI67 ECAD
MUC5AC ECAD
CHGA ECAD
AQP5-2A-iCaspase
L
Ablation
Day 3
Day 7
Day 10
Control
+ Dim
M
Relative AQP5 levels
P = 0.004
Control
+Dim
N
Relative organoid numbers (%)
P < 0.0001
Control
+Dim

Fig. 3. Ablation of mouse and human AQP5+ cancer stem cells block tumour initiation and progression in experimental models. (**A**) *In vitro* DT treatment of Aqp5-Cre/APK/DTR mouse pyloric tumour organoids at the point of organoid initiation (day 0) blocks organoid outgrowth. *n* = 4 biological replicates; scale bars, 500μm. (**B**) Quantification of change in organoid numbers over time in control and DT-treated organoid cultures following DT treatment on day 0. (**C**) *In vitro* DT treatment of Aqp5-Cre/APK/DTR mouse pyloric tumour organoids during organoid growth/maintenance (day 3) results in rapid decline of the cultures, with no viable organoids remaining by day 7. *n* = 4 biological replicates; scale bars, 500μm. (**D**) Quantification of change in organoid numbers over time in control and DT-treated organoid cultures following DT treatment on day 3. (**E**) Schematic of the *Aqp5-2A-DTR* allele used for DT-mediated AQP5+ cell ablation in a mouse orthotopic tumour model. (**F** and **G**) Intraperitoneal DT administration to mice orthotopically transplanted with Aqp5-Cre/APK/DTR organoids during early stages of tumour initiation (day 3) results in complete suppression of tumour outgrowth (F), whereas ablation performed during later stages of tumour growth (week 4) results in tumour regression by week 8 (G), as reflected in representative H&E images (left) and tumour volume quantifications (right). *n* = 3 independent replicates; scale bars, 1mm. (**H** and **I**) Intraperitoneal DT administration to mice orthotopically transplanted with Aqp5-Cre/APK/DTR organoids at week 4 and analysed at an extended timepoint of 12 weeks shows that ablated tissues retain some tumour cells but fail to recur (H), whereas repeated weekly ablation of AQP5+ cells results in complete elimination of the tumour load (I), as reflected in representative H&E images (left) and tumour volume quantifications (right). *n* = 3 independent replicates; scale bars, 1mm. (**J**) Strategy for AQP5+ cell ablation within human gastric cancer organoids. The *AQP5-2A-iCaspase9* cassette is integrated into human gastric cancer organoids to drive expression of inducible Caspase9 within AQP5+ cells. Addition of B/B Homodimerizer promotes dimerization of Caspase9 and activation of apoptotic pathways leading to cell death. (**K**) Immunofluorescence of AQP5, KI67, MUC5AC, and CHGA confirms the presence of expected lineage markers within AQP5-2A-iCaspase organoids. *n* = 3 independent replicates; scale bars, 100μm. (**L**) B/B Homodimerizer treatment (+Dim) of *AQP5-2A-iCaspase* human gastric cancer organoids hinders organoid growth *in vitro*. *n* = 5 independent replicates; scale bars, 500μm. (**M**) B/B Homodimerizer treatment (+Dim) of *AQP5-2A-iCaspase* organoids results in ~60% decrease in AQP5 levels relative to control untreated organoids as measured by qPCR. (**N**) Quantification of organoid numbers present in control untreated and B/B Homodimerizer-treated (+Dim) *AQP5-2A-iCaspase* organoid cultures at day 10. Graphs represent mean ± S.D. with two-tailed unpaired *t*-test.

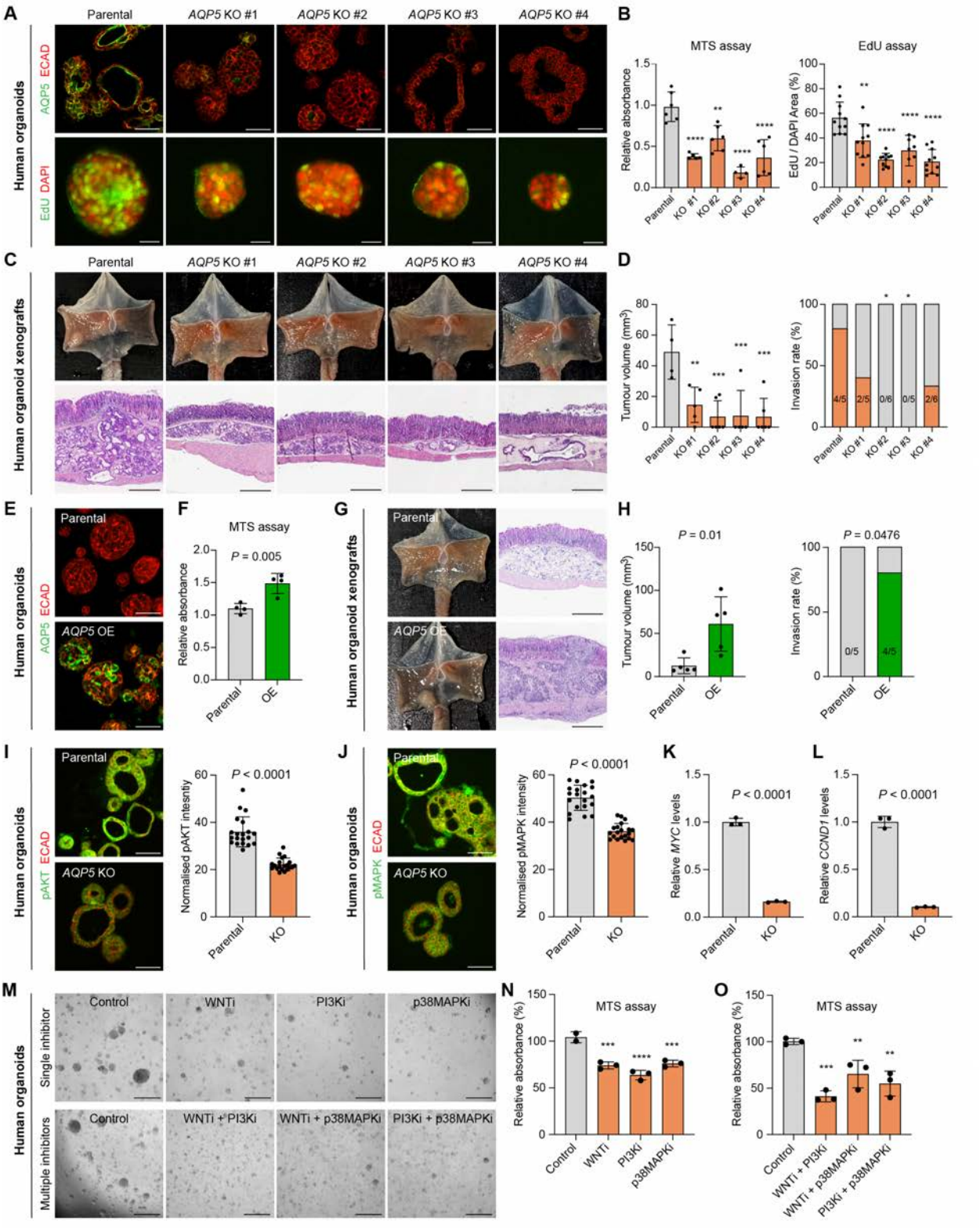
A
Parental
AQP5 KO #1
AQP5 KO #2
AQP5 KO #3
AQP5 KO #4
Human organoids
AQP5 ECAD
EdU DAPI
B
MTS assay
Relative absorbance
EdU assay
EdU / DAPI Area (%)
Parental
KO #1
KO #2
KO #3
KO #4
C
Human organoid xenografts
D
Tumour volume (mm3)
Invasion rate (%)
4/5
2/5
0/6
0/5
2/6
E
AQP5 OE
F
P = 0.005
G
H
P = 0.01
P = 0.0476
0/5
4/5
I
pAKT ECAD
Normalised pAKT intesnty
P < 0.0001
J
pMAPK ECAD
Normalised pMAPK intensity
K
Relative MYC levels
L
Relative CCND1 levels
M
Single inhibitor
Multiple inhibitors
Control
WNTi
PI3Ki
p38MAPKi
WNTi + PI3Ki
WNTi + p38MAPKi
PI3Ki + p38MAPKi
N
O

Fig. 4. AQP5 drives gastric cancer progression in human gastric cancer organoid and mouse xenograft models via WNT, PI3K, and MAPK signalling. (**A**) Representative images depicting a human gastric cancer organoid line (parental) and four independent *AQP5* KO clones derived from the same parental line (clones #1, #2, #3, and #4). AQP5 is expressed in apical membranes of the parental organoids but absent from all KO clones (top). Reduced EdU staining is detected within *AQP5* KO organoids compared to parental (bottom). n = 3 independent replicates; scale bars, 500μm (top), 100μm (bottom). (**B**) Quantification of cell proliferation within parental and *AQP5* KO organoids using an *in vitro* MTS colorimetric assay (left) and EdU staining assay (right). Statistical analyses for both datasets were performed using one-way ANOVA with Dunnett's multiple comparisons test. $^{**}P = 0.001$, $^{****}P < 0.0001$. (**C**) Representative whole mount (top) and H&E (bottom) images of orthotopic tumours derived from transplanted parental and *AQP5* KO human gastric cancer organoids. n = 5 biological replicates; scale bars, 1mm. (**D**) Quantification of tumour volumes (left) and invasion rates (right) of orthotopic tumours derived from transplanted parental and *AQP5* KO human gastric cancer organoids. Statistical analysis for tumour volume was performed using one-way ANOVA with Dunnett's multiple comparisons test, and with Fisher's exact test for invasion rate. Tumour volume: $^{**}P = 0.003$, $^{***}P = 0.0003$ (KO#2, #4), $^{***}P = 0.0006$ (KO#3). Invasion rate: $^{*}P = 0.02$ (KO#2), $^{*}P = 0.0476$ (KO#3). (**E**) Representative immunofluorescence images confirm the upregulation of AQP5 in *AQP5*-overexpressing (OE) organoids. n = 3 independent replicates; scale bars, 500μm. (**F**) *AQP5* OE organoids show greater cell proliferation rates *in vitro* compared to parental organoids as measured by an MTS assay. (**G**) Representative whole mount (left) and H&E (right) images depict the histological features of tumours formed from transplanted parental and *AQP5* OE organoids. n = 5 biological replicates; scale bars, 1mm. (**H**) Quantifications of tumour volumes (left) and invasion rates (right) of orthotopic tumours derived from transplanted parental and *AQP5* OE human gastric cancer organoids. Statistical analysis for invasion rate was performed using a Fisher's exact test. (**I** and **J**) Representative immunofluorescence images (left) and quantifications (right) of pAKT (I) and pMAPK (J) expression in parental and *AQP5* KO organoids, showing reduced PI3K and MAPK signalling in *AQP5* KO organoids relative to parental organoids. n = 3 independent replicates; scale bars, 500μm. (**K** and **L**) qPCR of WNT target genes *MYC* (K) and *CCND1* (L) shows reduced WNT signalling in *AQP5* KO organoids compared to parental organoids. (**M**) Single inhibitors significantly reduce growth of human gastric cancer organoids, but the effect is increased with the combined use of multiple inhibitors. n = 3 independent replicates; scale bars, 500μm. (**N** and **O**) Quantification of cell proliferation within control and drug-treated organoids using an *in vitro* MTS colorimetric assay, for single inhibitors (N) and multiple inhibitors (O). Statistical analyses for both datasets were performed using one-way ANOVA with Dunnett's multiple comparisons test. $^{**}P < 0.01$, $^{***}P < 0.001$, $^{****}P < 0.0001$. Graphs represent mean ± S.D. with two-tailed unpaired t-test unless otherwise specified.

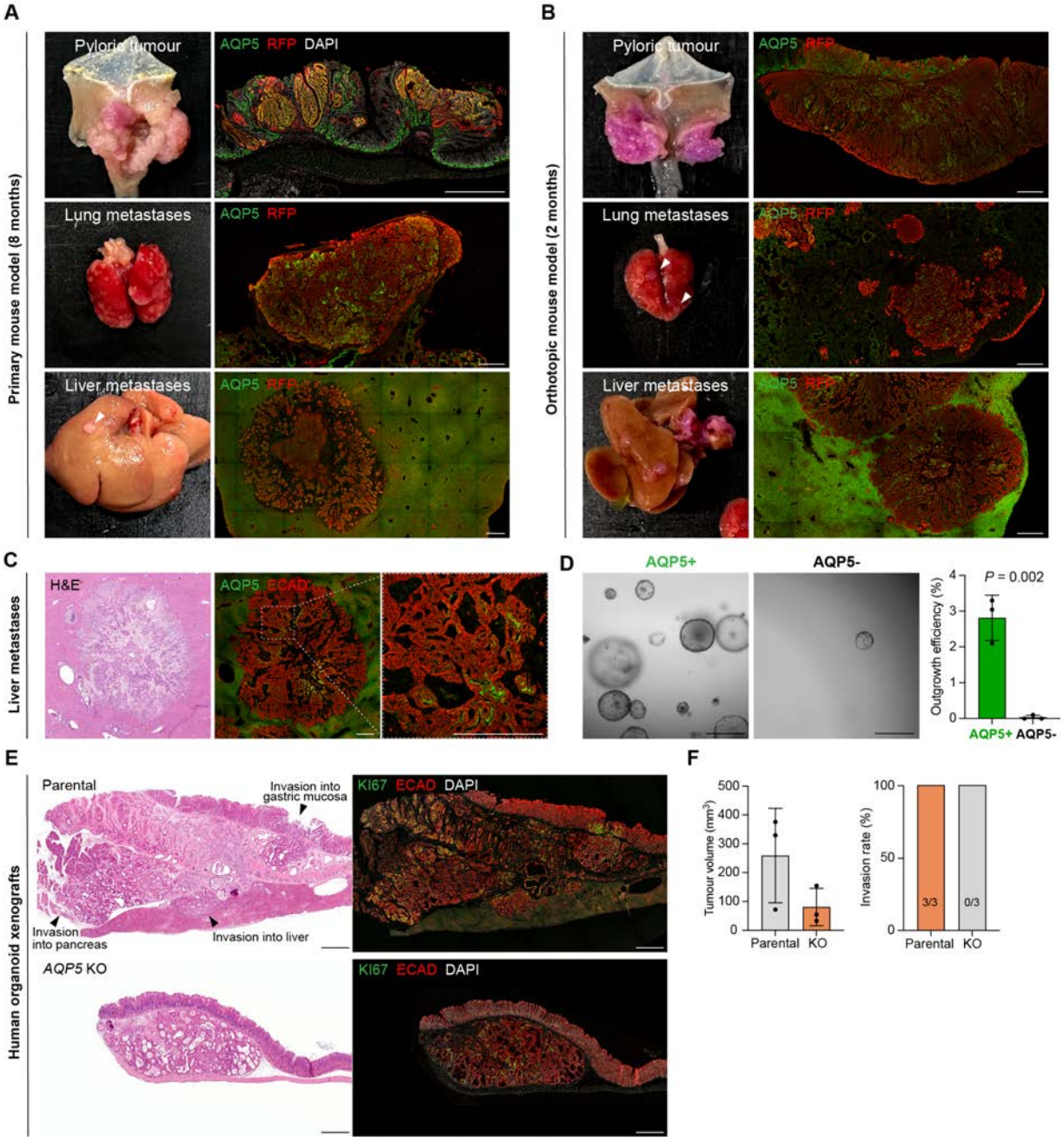

Fig. 5. AQP5+ cells are functional cancer stem cells in mouse metastatic gastric cancer and human organoid models. (**A**) Representative whole mount images of tumours observed in the stomach, lungs and liver isolated from the Aqp5-Cre/APK primary mouse model 8 months following induction (left). Immunofluorescence shows AQP5 expression and the distribution of RFP+ cancer cells within the tissues (right). n = 3 independent replicates; scale bars, 1mm. (**B**) Representative whole mount images of tumours observed in the stomach, lungs and liver isolated from the orthotopic cancer mouse model 2 months following transplantation of Aqp5-Cre/APK pyloric tumour organoids (left). Immunofluorescence shows AQP5 expression and the distribution of RFP+ cancer cells within the tissues (right). n = 3 independent replicates; scale bars, 1mm. (**C**) Histological analysis of liver metastases derived from the orthotopic cancer mouse model, with H&E (left) and AQP5 immunofluorescence (right) shown. (**D**) AQP5+ cells isolated from liver

metastatic tumours form organoids more efficiently than AQP5- cells. *n* = 3 independent replicates; scale bars, 500μm. (**E**) Analysis of human organoid xenografts 16 weeks following transplantation reveals extensive invasion of parental xenografts into the gastric mucosa and near-complete replacement of the muscle layer leading to integration of the cancer cells into surrounding liver and pancreatic tissues. In contrast, *AQP5* KO organoid xenografts display minimal signs of invasion and are retained in the submucosal layer. *n* = 3 independent replicates; scale bars, 1mm. (**F**) Quantifications of tumour volumes (left) and invasion rates (right) of xenografts derived from transplanted parental and *AQP5* KO human gastric cancer organoids. Graphs represent mean ± S.D. with two-tailed unpaired *t*-test.

Science
AAAS

Supplementary Materials for

AQP5: A functional gastric cancer stem cell marker in mouse and human tumors

Hui Yi Grace Lim[1]†, Swathi Yada[1]†, Kazuhiro Murakami[2], Bernett Teck Kwong Lee[3,4,5,6], Sowmya Sagiraju[1], Phyllis Phuah[1], Tanysha Chi-Ying Chen[1], Fidelia B. Alvina[1], Si Hui Tan[1], Kaushal Krishna Kaslikar[3,4], Nur Syahirah Binte Ruhazat[3,4,7], Menaka Priyadharsani Rajapakse[8], Katzrin Bte Ahmad Murad[1], Snezhina Kancheva[1], Liang Thing Tan[1], Seri Mustafah[8], Jimmy Bok Yan So[9,10], Nick Barker[1,11,13]*

Corresponding author: Nick Barker, nicholas_barker@imcb.a-star.edu.sg

The PDF file includes:

Materials and Methods
Figs. S1 to S19
Tables S1 to S7

Materials and Methods

Genetic conditional mouse models

Aqp5-eGFP-ires-creERT2, *Aqp5-2A-creERT2*, and *Aqp5-2A-DTR* mice were previously generated (*9*). Mice containing *Rosa26-tdTomato*^{LSL} (Ai14) (JAX 007914), *Apc*$^{fl/fl}$ (MGI 1857966), *Pten*$^{fl/fl}$ (MGI 2182005), *Kras*$^{LSL\text{-}G12D}$ (JAX 019104), and *p53*^{R172H} were also previously described (*9*). Aqp5 KO mice were obtained from Cyagen (KOCMP-11830-Aqp5-B6N-VA). All mice were housed under specific pathogen free (SPF) conditions and regularly tested as negative for infectious agents. Experimental mice were litter mates and sex-matched wherever possible. All mouse experiments were performed in accordance with ethical and safety regulations covered by the A*STAR Institutional Animal Care and Use Committee (IACUC) under IACUC No. 201528 and 231779. Mice were immediately sacrificed when tumours reached the maximum allowable size of 20mm.

Tumour xenograft models

Orthotopic transplants were performed on NOD.Cg-Prkdcscid Il2rgtm1Wjl/SzJ (NSG) mice (JAX 005557). Briefly, mice were anesthetised, and their stomach exposed under sterile surgical conditions. Injection was performed using an insulin syringe containing the transplantation material (cells or organoids) inserted in the pylorus region immediately beneath the outer muscle layer. Following the procedure, the wounds were sutured, and the mice administered the reversal drug Atipamezole, along with Buprenorphine over several days after surgery. All mouse experiments were performed in accordance with ethical and safety regulations covered by the A*STAR Institutional Animal Care and Use Committee (IACUC) under IACUC No. 201528 and 231779. Mice were immediately sacrificed when tumours reached the maximum allowable size of 20mm.

Human participants

Patient pyloric tumour biopsies were provided by Department of Surgery, National University Hospital Singapore (IRB protocol 2020-038). Informed consent was obtained from all patients. The research team was blinded to patient identifiers including age, sex, gender, ancestry, race, ethnicity, and socioeconomic status. Patient diagnosis and tumour characteristics were evaluated by a clinical pathologist. Fresh tumour samples were collected in an Advanced DMEM/F-12 media (Gibco 12634-028) with 2mM GlutaMAX supplement (Gibco 35050-079), 10mM HEPES (Gibco 15630-056), 1mM N-acetyl-L-cysteine (Sigma A9165), and 1x Antibiotic-Antimycotic (Gibco 15240096). Samples were washed vigorously in HBSS prior to proceeding with steps for tissue dissociation. All experiments involving human material were performed in accordance with ethical and safety regulations covered by the A*STAR Institutional Review Board (IRB) under IRB No. 2020-038.

Cell lines

KATOIII, SNU601, and AGS cell lines were a gift from P. Tan. The identity of all cell lines was authenticated by STR profiling (ATCC) prior to use. All cells were grown in a RPMI media with 10% FBS, 1x GlutaMAX supplement (Gibco 35050-079), 1x MEM Non-Essential Amino Acids Solution (Gibco 11140050), and 100U/ml Penicillin-Streptomycin (Gibco 15140122). Cells were passaged when confluent approximately once a week by dissociating with 0.25% Trypsin-EDTA (Gibco 25200056).

Organoids

Pyloric tumour organoids were grown in a basal media comprising Advanced DMEM/F-12 (Gibco 12634-028) with 2mM GlutaMAX supplement (Gibco 35050-079), 10mM HEPES (Gibco 15630-056), 1x N2 (Gibco 17502-048), 1x B27 (Gibco 17504-044), 1mM N-acetyl-L-cysteine (Sigma A9165), and 200μg/ml Primocin (InvivoGen Ant-pm-1). For mouse pyloric tumour organoid cultures, organoids in their first passage after plating were supplemented with these recombinant growth factors at the indicated concentrations: 50ng/ml EGF (Gibco PMG8043), 100ng/ml FGF-10 (Peprotech 100-26), 10nM [Leu15]-Gastrin I (Sigma G9145), 100ng/ml Wnt3A (Peprotech 315-20), 1μg/ml R-Spondin-1 (Peprotech 120-38), 100ng/ml Noggin (Peprotech 250-38). Following establishment, the cultures were switched to basal media for long-term maintenance to select for tumour organoids. Sorted single cells seeded in culture for organoid initiation assays were grown in basal media in the absence of growth factors. Human gastric cancer organoids HCM-BROD-0045-C16, HCM-BROD-0116-C16, and HCM-BROD-0235-C16 were purchased from ATCC. Human organoid cultures were given the abovementioned recombinant growth factors along with 2μM A83-01 (Tocris 2939) and 10mM Nicotinamide (Sigma N0636) in a base media composed of 50% WRNF conditioned media. Single cell cultures also received 10μM Y-27632 (Tocris 1254). Organoids were passaged when confluent approximately once a week by dissociating them with TrypLE (Gibco 12604) and continued maintenance in Growth Factor Reduced Matrigel basement membrane matrix (Corning 356231). For experiments involving orthotopic transplantation of organoids into mice, intact organoids were retrieved from Matrigel using Cell Recovery Solution (Corning 354253).

Mouse injections

For induction of Cre recombination, 8-week-old mice were injected intraperitoneally with 4mg Tamoxifen (Sigma T5648) dissolved in sunflower oil per 30g of mouse weight. Diphtheria toxin (DT) (Sigma D0564) administration was performed intraperitoneally, at a dose of 0.5μg DT dissolved in PBS per 30g of mouse weight.

Tissue dissociation for FACS

Dissociation of pyloric tumours was performed by incubation of minced tissue in an Advanced DMEM/F-12 media (Gibco 12634-028) with 2mM GlutaMAX supplement (Gibco 35050-079), 10mM HEPES (Gibco 15630-056), 2mg/ml Bovine Serum Albumin (BSA), and 1mg/ml Collagenase Type I (Gibco 17100017), at 37ºC for 45min. To release the gastric glands, minced tissues were vigorously and repeatedly pipetted using cold Advanced DMEM/F-12 buffer and filtered through a 100μm filter mesh before being spun down at 2500rpm at 4ºC for 3min. The resultant pellet was further dissociated into a single cell suspension by incubating with TrypLE (Gibco 12604) and 10mg/ml DNase I (Sigma D4513) at 37ºC for 10min. The digestion reaction was quenched using 30ml cold HBSS, and the suspension centrifuged at 2500rpm at 4ºC for 3min. For mouse pyloric tumours with AQP5 tagged with eGFP, the cell pellet was directly resuspended in 2% fetal bovine serum (FBS) in HBSS and passed through a 40μm filter for cell sorting on the BD Influx Cell Sorter (BD Biosciences). For human pyloric tumours, single cell suspensions following TrypLE digestion were incubated with AQP5-AF647 (1:500, Abcam ab215225), CD11b-FITC (1:200, Biolegend 101205), CD31-FITC (1:200, Biolegend 303103), and CD45-FITC (1:200, Biolegend 304054) in 2% FBS in HBSS at 4ºC for 45min. Cells were washed twice with 2% FBS in HBSS prior to filtering through the 40μm filter for FACS. Prior to FACS, cells were resuspended with DAPI for live/dead cell gating. Sorted cells were collected directly in RLT

Plus Buffer (Qiagen) with b-mercaptoethanol for RNA isolation or Advanced DMEM/F-12 with 0.5% Matrigel (Corning 354253) for organoid culture.

RNA isolation and qPCR

Cell lysis for RNA extraction was performed using RLT Plus buffer (Qiagen) with b-mercaptoethanol. RNA was purified from the cell extracts using the RNeasy Mini or Micro Kit (Qiagen) and used for cDNA synthesis with the Superscript III kit (Life Technologies), following manufacturer's instructions. qPCR was performed in triplicates using the GoTaq qPCR Master Mix (Promega A6002). qPCR reactions were run on the QuantStudio 7 Flex Real-Time PCR system (Applied Biosystems) and analysed using the double delta Ct method. For qPCR validation of RNA sequencing targets, cDNA amplification was performed using the Ovation Pico WTA System (NuGen 3302-60) following manufacturer's instructions in order to generate sufficient material for validation of a large number of targets. All qPCR primer sequences used in this paper are summarized in Table S5.

Bulk RNA sequencing

For bulk RNA sequencing, cells were collected directly in RLT Plus buffer (Qiagen) with β-mercaptoethanol during FACS sorting. Total RNA was extracted using the RNeasy Micro Kit (Qiagen 74034). The RNA integrity of all samples was verified by Agilent RNA 6000 Pico Chips (Agilent 5067-1513) and ran on the Agilent 2100 Bioanalyzer prior to proceeding with downstream library preparation methods. For AQP5+ samples, qPCR was also performed to confirm enrichment of Aqp5 levels over the corresponding sorted AQP5- samples. Due to the low amount of material available from sorted human cells, RNA from human samples was first amplified using the SMARTer Ultra Low RNA kit (Clontech 634936) prior to library construction and sequencing. For library construction, mRNA was enriched using oligo(dT) beads and double-stranded cDNA library generated following manufacturer's instructions. Sequencing of libraries was performed on the NovaSeq PE150 (Illumina) and Illumina real-time analysis software used for base-calling to obtain FASTQ files.

FASTQ files were checked using FASTQC and MultiQC and found to be of good quality. Sequence reads were mapped to the human genome build GRCh38 for human samples and mouse genome build GRCm39 for mouse samples using STAR aligner utilising annotations from GENCODE v41 for human and GENCODE vM22 for mouse samples respectively. Gene counts were determined by featureCounts (part of the Subread package) using GENCODE v41 gene annotation for human samples and GENCODEvM30 gene annotation for mouse samples. Differential expression analysis was performed using the edgeR package in R. The ClusterProfiler package in R was utilized to perform Gene Ontology (GO) enrichment analysis on differentially expressed genes. Multiple testing correction for differential gene expression analyses were performed using the Benjamini-Hochberg method.

Single cell RNA sequencing

For single cell RNA-sequencing, mouse pyloric tumour tissue was dissociated into a single cell suspension following the same procedure for FACS. Only samples with cell viability >70% and cell concentration of 1,000 cells/µl proceeded for library construction. Libraries were prepared using 10X Genomics Single-Cell 3' v3.1 Gene Expression Kit following manufacturer's instructions. Sequencing of libraries was performed on the NovaSeq PE150 (Illumina) and

Illumina real-time analysis software used for base-calling to obtain FASTQ files. For analysis of existing single cell RNA sequencing public datasets, human scRNAseq gene cell counts were obtained from NCBI GEO (Accession IDs: GSE183904, GSE150290). These datasets comprised primary gastric tumour and normal patient samples of varying subtypes and locations. Cells with high mitochondrial DNA (mtDNA) content (>20%) were first filtered out. Then, standard log normalization, scaling of data, and principal component analysis (PCA) were performed using the top 2,000 variable features. Graph-based clustering was performed on the first 10 principal components of the PCA-reduced data at a clustering resolution of 0.5. Clusters were visualized using a Uniform Manifold Algorithm Projection (UMAP) plot. Epithelial cell clusters were identified using pan-epithelial markers Epcam, Krt8 and Krt18. Key gene markers for each cluster were then identified using the FindAllMarkers function in the Seurat package in R, and cell types assigned based on these gene markers with the aid of supporting literature. Finally, we defined the "Aqp5-high" subset as the top 20% of cells expressing the highest levels of Aqp5 within the dataset.

Spatial transcriptomics

Aqp5-Cre/APK mouse pyloric tumour tissues were harvested and processed under RNase-free conditions following standard protocols to fix, dehydrate, and embed tissues into paraffin blocks. RNA integrity of the tissue sections was confirmed by DV200 score >60% before proceeding with MERSCOPE on a custom gene panel. Genes with predicted transcript abundances >1,000 FPKM were excluded from the gene panel to reduce the likelihood of optical crowding. Standard data processing, dimensionality reduction, and Leiden clustering was performed on the MERSCOPE dataset to generate the UMAP plot and identify distinct cell clusters.

Histology and staining methods

All tissues were processed according to standard protocols. Briefly, fresh tissues were fixed in 4% paraformaldehyde at 4ºC overnight, dehydrated, and processed into paraffin blocks. 8µm tissue sections collected on glass slides were deparaffinated and rehydrated. For Hematoxylin & Eosin (H&E), FFPE sections were stained with Richard Allan Haematoxylin, differentiated with acid alcohol (1% HCl in 70% alcohol), followed by Scott's blue and Eosin counterstaining. For immunohistochemistry (IHC) and immunofluorescence (IF), antigen retrieval was performed on rehydrated slides in a citrate pH 6.1 (Dako, S169984) or pH 9.0 (Dako, S236784) target retrieval solution at 121ºC in a pressure cooker. Primary antibodies used were rabbit anti-AQP5 (1:500, Invitrogen PA5-64195 or LSBio LS-C756566), mouse anti-CHGA (1:200, Abcam ab15160), rabbit anti-cleaved Caspase-3 (1:200 , Cell Signaling 9661S), mouse anti-E-cadherin (1:200, BD Biosciences 610181), rabbit anti-KI67 (1:200, Invitrogen MA5-14520), mouse anti-MUC5AC (1:200, Leica Biosystems NCL-HGM-45-M1), rabbit anti-RFP (1:500, Rockland 600-401-379), rabbit anti-TFF2 (1:1500, Proteintech 13681-1-AP), rabbit anti-Vimentin (1:500, Abcam ab92547), rabbit anti-P53 (1:1500, home-made antibody from David Lane). Secondary antibodies used were mouse or rabbit EnVision+ (DAKO) for IHC and anti-mouse or anti-rabbit Alexa Fluor 488, 568, or 647 (1:500, Invitrogen) for IF.

RNAscope methods

For in-situ hybridization (ISH) experiments, tissues were collected under RNase-free conditions and fixed in 4% paraformaldehyde at room temperature for 16-24h. RNAscope was performed using the RNAscope 2.5 High Definition Brown Assay (ACDbio 322300) and 2.5 High

Definition Duplex Reagent Assay following manufacturer's instructions. The following mouse probes were used: Mm-Aqp5 (ACDbio 430021), Mm-Lgr5 (ACDbio 312171), Mm-Rgs5 (ACDbio 430181), Mm-Pthlh (ACDbio 456521), Mm-Hey1 (ACDbio 319021), Mm-Cd44 (ACDbio 476201), and Mm-Cxcr4 (ACDbio 425901). The following human probes were used: Hs-AQP5 (ACDbio 452371), Hs-CLDN2 (ACDbio 492051), Hs-DCHS2 (ACDbio 1309261), Hs-HEY2 (ACDbio 441761), and Hs-PLA1A (ACDbio 536951).

Generation of modified gastric cancer cell lines

To generate AQP5-overexpressing cell lines, linearized pCMV-hAQP5-GFP plasmid (Origene RG206069) was transfected using the Lipofectamine 2000 transfection reagent (Invitrogen 11668019), following manufacturer's recommendations. Successful transfectants were selected by Geneticin (Gibco 10131027). To generate AQP5 KO cell lines, gDNA targeting AQP5 was ligated into SpCas9-HF1 vector and transfection performed using Lipofectamine 2000.

In vitro assays in cell lines

For analyses of cell proliferation, equal numbers of cells were seeded in 96-well plates, grown for a fixed length of time, and incubated with the CellTiter AQueous One Solution Assay (Promega G3582). The absorbance at 490nm was measured using a plate reader as a readout of cell proliferation. To measure cell migration, the scratch assay was performed by seeding cells in a 2 Well Culture-Insert in 35mm μ-Dish (Ibidi 81176) and removing the insert when a confluent cell monolayer was established. Images of the gap were captured at fixed timepoints and the length of the gap measured using Fiji.

Generation of modified gastric cancer organoid lines

To generate gene-edited human gastric cancer organoids, the following plasmids were electroporated: 1) HR110PA-1 hAQP5-5'arm-P2A-iCas9-IRES-Venus-3'arm, pX330 hAQP5 gRNA-1, and pX330 hAQP5 gRNA-2 to generate Aqp5-2A-iCaspase organoids, where the 2A-iCas9 cassette is inserted after the end of the *AQP5* transcript to retain endogenous AQP5 expression, 2) HR110PA-1 hAQP5-5'arm-CreERT2-pA-3'arm, pX330 hAQP5 gRNA-1, and pX330 hAQP5 gRNA-2 followed by AAVS1-2A-Blasticidin-CAG-LSL-tdTomato and pX330 AAVS1 gRNA to generate Aqp5-2A-CreERT2;LSL-tdTomato organoids, 3) FLIP-Puro-hAQP5 and pX330 hAQP5 FLIP gRNA to generate Aqp5-FLIP-Puro organoids, 4) HR110PA-1 hLGR5-5'arm-P2A-Venus-3'arm, pX330 hLGR5 gRNA-1, and pX330 hLGR5 gRNA-2 to generate Lgr5-2A-Venus organoids, and 5) pCI-neo β-catenin S337 (Addgene plasmid #16519), pCI-neo β-catenin Δ45 (Addgene plasmid #16520), pCMV2-Tag2A PIK3CA H1047R (Addgene plasmid #16639), and pCMV2-Tag2A PIK3CA E545K (Addgene plasmid #16642) individually into *AQP5* KO organoids to generate individual pathway rescue organoid lines. The pX330 plasmids were derived from pX330-U6-Chimeric_BB-CBh-hSpCas9 (Addgene plasmid #42230). For AQP5 overexpression in human gastric cancer organoids, linearised pPBCAG-hAQP5-GFP-IP was used. Electroporation of organoids was performed using the NEPA21 Electroporator (NEPA GENE) following manufacturer's recommendations. Briefly, organoids were supplemented with 5μM CHIR99021 (Stemgent 04-0004-10) and 10μM Y-27632 (Tocris 1254) one day prior to electroporation. Organoids were dissociated using TrypLE (Gibco 12604) and washed with Opti-MEM I reduced serum medium (Gibco 31985-062). The cell pellet was resuspended with BTXpress (BTX 45-0805) and the respective plasmids at a ratio of 100,000 cells to 15μg DNA before loading into the electroporation cuvette. Electroporation was performed with a poring pulse

of 175V and pulse length of 5ms. Successful transfectants were selected by puromycin (InvivoGen Ant-pr-1), with the exception of the AAVS1-2A-Blasticidin-CAG-LSL-tdTomato organoids selected by blasticidin (InvivoGen Ant-bl-1). Following transfection of the AQP5-2A-iCaspase and AQP5-2A-CreERT2 constructs, organoids were further treated with Cre Recombinase Gesicles (Takara Bio 631449) to remove the selection cassette. Briefly, organoids were dissociated by TrypLE (Gibco 12604) and washed with 10% FBS in Advanced DMEM/F12 (Invitrogen 12634-028). Cre Recombinase Gesicles (Takara Bio 631449) and 6μg/ml polybrene (Sigma H9268) were added and the suspension centrifuged at 600g at 32ºC for 1h. The cells were incubated at 37ºC for 6h before transferring into Matrigel. Following Cre Gesicle treatment, cells were grown in organoid media without puromycin for 1 week and cell sorting performed on the BD Influx Cell Sorter (BD Biosciences) to collect RFP negative cells.

In vitro assays in organoids

To measure cell proliferation in organoids, equal numbers of cells were seeded in 96-well plates within Matrigel, left to grow for 3 days, and incubated for 2h with CellTiter AQueous One Solution Assay (Promega G3582). The absorbance at 490nm was measured using a plate reader as a readout of cell proliferation. Proliferation was also measured using the Click-iT EdU Cell Proliferation Kit with Alexa Fluor 594 (Life Technologies C10339) following manufacturer's recommendations. Whole mount organoids were imaged on the Evos M5000 (Thermofisher).

AQP5+ cell ablation in organoids

To induce AQP5+ cell ablation, organoids were treated with 500nM B/B Homodimerizer (Takara Bio 635059) for Aqp5-2A-iCaspase organoids and 240ng/ml DT for Aqp5-2A-DTR organoids. To perform lineage tracing of Aqp5+ cells in AQP5-2A-CreERT2; LSL-tdTomato organoids, 1μM 4-OHT was administered to organoids for 16h and removed thereafter. For conditional Aqp5 KO in AQP5-FLIP-Puro organoids, organoids were dissociated by TrypLE (Gibco 12604) and washed with 10% FBS in Advanced DMEM/F12 (Invitrogen 12634-028). Cre Recombinase Gesicles (Takara Bio 631449) and 6μg/ml polybrene (Sigma H9268) were added and the suspension centrifuged at 600g at 32ºC for 1h. The cells were incubated at 37ºC for 6h before transferring into Matrigel. Following Cre Gesicle treatment, cells were grown in organoid media without puromycin.

Drug treatment in organoids

For pathway inhibition experiments, 500nM Apitolisib / GDC-0980 (TargetMol, T1916), 10μM Adezmapimod / SB203580 (TargetMol, T1764) and 10μM IWR-1-endo (TargetMol, T2651) were used for inhibition of PI3K, p38MAPK, and Wnt pathways respectively. Drugs at the indicated final concentrations were added to culture media immediately upon organoid plating and refreshed every 3 days.

Microscopy

For image acquisition, H&E and IHC slides were captured using the Nikon ECLIPSE Ni-E microscope with DS-10 camera. IF images were acquired using the Zeiss LSM780 laser scanning confocal microscope and Nikon A1RHD25 confocal microscope. Brightfield and fluorescence images of organoids were taken with the Thermofisher Evos M5000 system. Large-area images acquired on the Nikon Ni-E microscope were processed with NIS-Elements AR software (Nikon),

and those acquired on the Thermofisher Evos M5000 microscope were stitched using Adobe Photoshop. All acquired images were processed using Fiji and Adobe Photoshop.

Statistical analyses

All statistical analyses were performed in GraphPad Prism. Qualitative datasets were analysed using the Fisher's exact test. Quantitative datasets were first evaluated for normality using the Shapiro-Wilk test. Variables that follow a normal distribution were analysed by the unpaired, two-tailed Student's *t*-test for two groups or ANOVA with Dunnett's multiple comparisons test for more than two groups, whereas variables that do not follow a normal distribution were analysed using an unpaired, two-tailed Mann-Whitney *U*-test for two groups or Kruskal-Wallis test with Dunn's multiple comparisons test for more than two groups. Reproducibility was confirmed by at least three independent experiments.

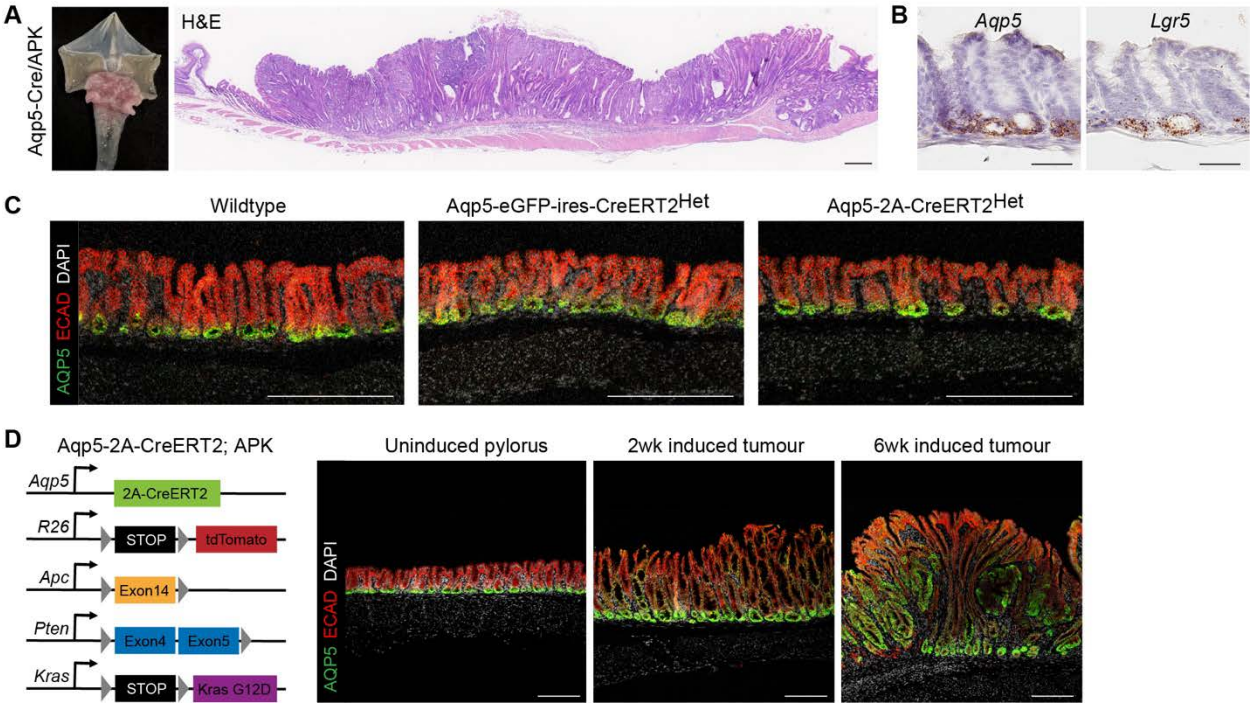

Fig. S1. Validation of mouse models used to generate advanced pyloric tumours. (**A**) Representative whole mount and H&E images of an Aqp5-Cre/APK mouse pyloric tumour. $n = 5$ biological replicates. (**B**) RNAscope of *Aqp5* (left) and *Lgr5* (right) in the healthy mouse pylorus, showing their co-localization within the gland base pyloric stem cell compartment. $n = 3$ biological replicates. (**C**) AQP5 expression is not perturbed in mouse models with the *Aqp5-eGFP-ires-CreERT2* or *Aqp5-2A-CreERT2* allele in a heterozygous form. (**D**) Schematic of the *Aqp5-2A-CreERT2; Apc$^{fl/fl}$; Pten$^{fl/fl}$; Kras$^{LSL\text{-}G12D/+}$; Rosa26-tdTomato^{LSL}* conditional genetic mouse model for pyloric cancer (left). AQP5 levels increase over time during tumour development and resembles expression patterns of tumours derived from *Aqp5-eGFP-ires-CreERT2* models (right). $n = 3$ biological replicates.

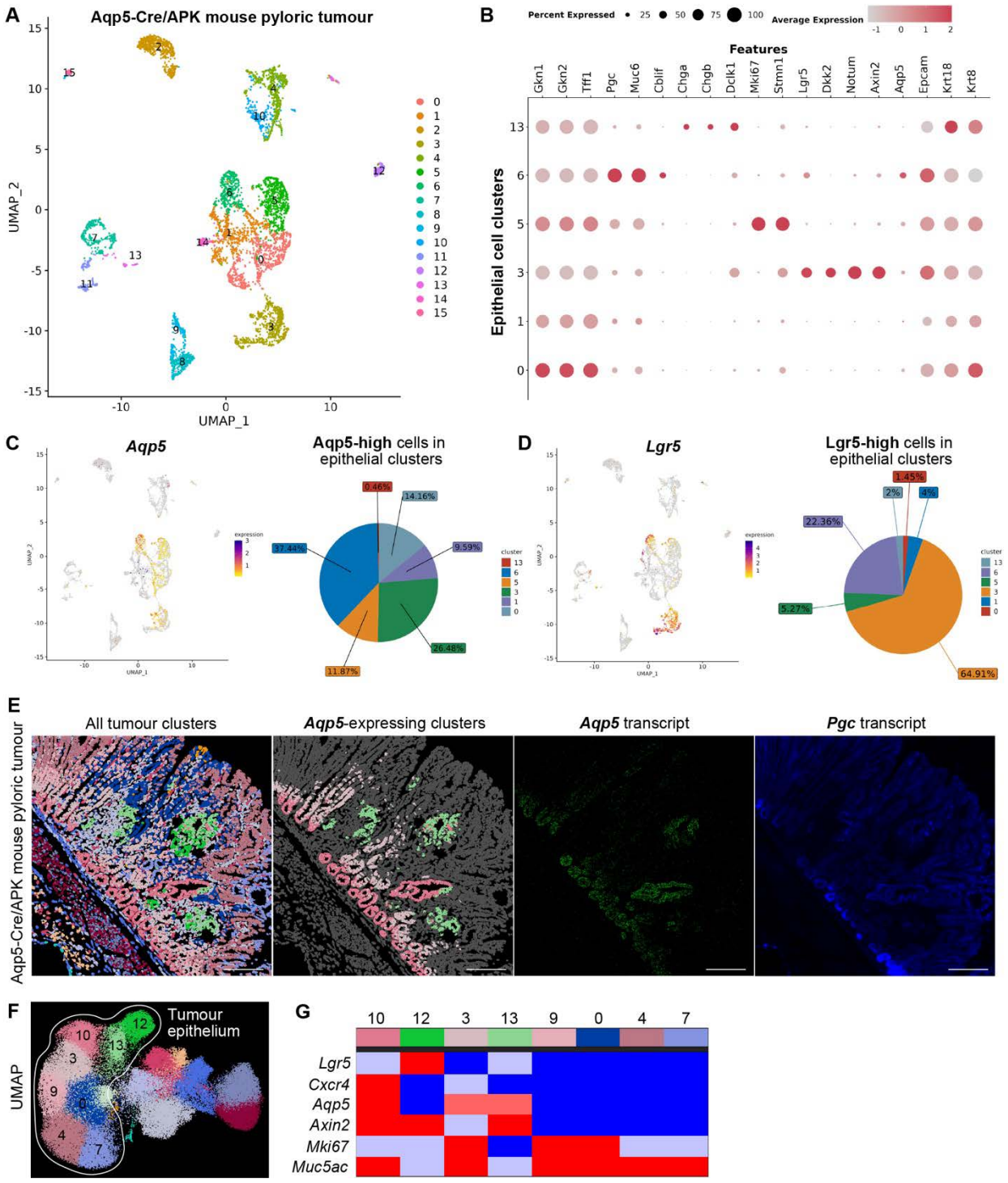

Fig. S2. AQP5 is enriched in a subset of epithelial cells within mouse pyloric tumours. (**A**) UMAP plot derived from scRNAseq of Aqp5-Cre/APK mouse pyloric tumour cells. (**B**) Dotplot of selected markers for assigning identities to each of the 6 epithelial cell clusters. (**C**) UMAP plot depicting expression of *Aqp5* (left) and pie chart showing relative proportions of *Aqp5*-high expressing cells across the epithelial cell populations (right). *Aqp5*-high cells are primarily enriched within cluster 6. (**D**) UMAP plot depicting expression of *Lgr5* (left) and pie chart showing

relative proportions of *Lgr5*-high expressing cells across the epithelial cell populations (right). *Lgr5*-high cells are primarily enriched within cluster 3. (**E**) MERSCOPE-based spatial transcriptomics of an Aqp5-Cre/APK mouse pyloric tumour section revealing highly heterogenous cell types assigned by Leiden clustering. The *Aqp5*-expressing clusters, *Aqp5* transcript levels, and *Pgc* transcript levels are indicated, highlighting the overlap of *Aqp5*-high cells with the gland-base *Pgc*+ cells. Scale bars, 200μm. (**F**) UMAP plot of Aqp5-Cre/APK tumour cell clusters derived from the MERSCOPE dataset, with the tumour epithelial clusters circled and labelled. (**G**) Heatmap of expression levels of selected markers in each of the 8 epithelial cell clusters.

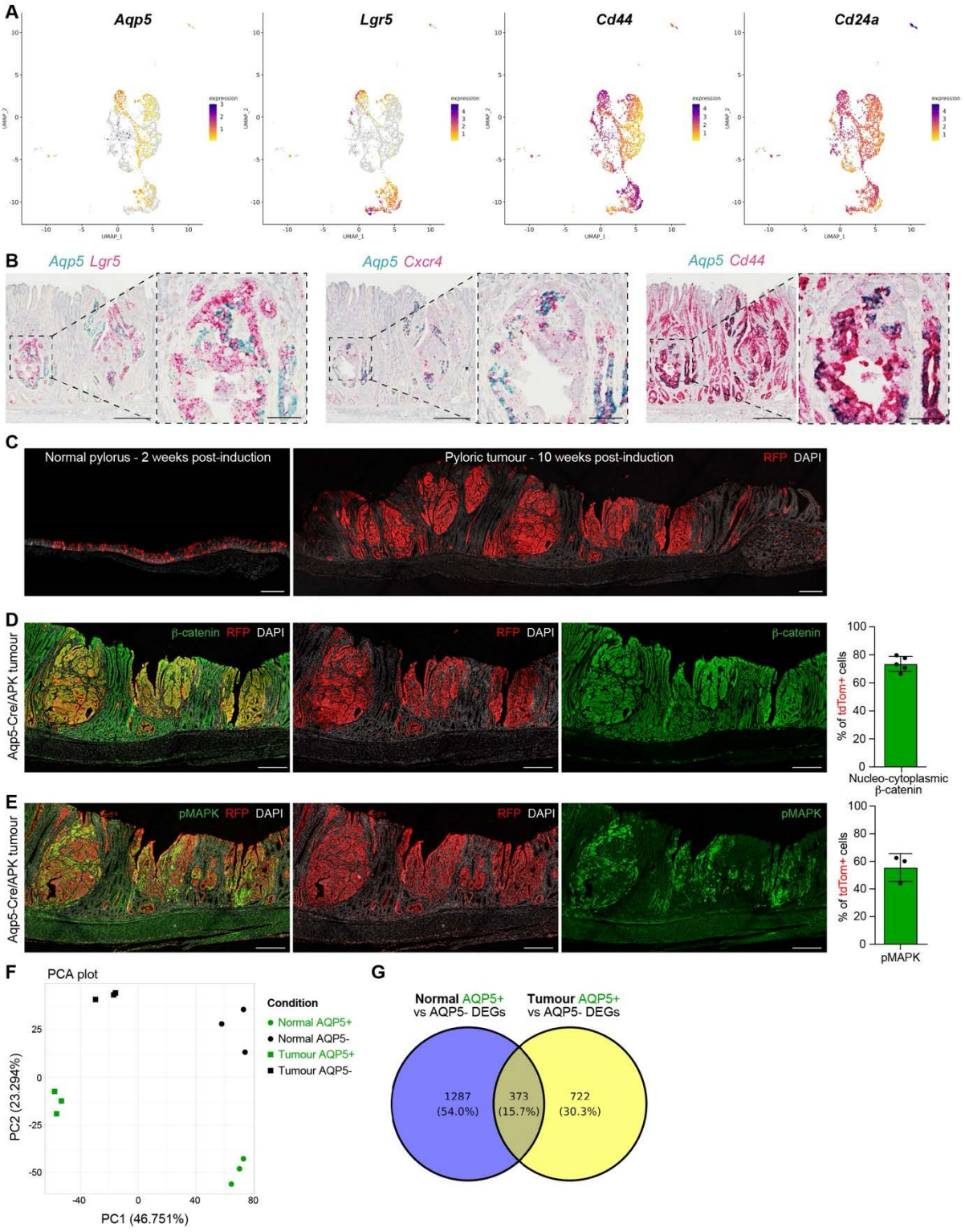

Fig. S3. Comparison of AQP5 with other stem markers and validation of RFP as a specific marker of the mouse pyloric tumour epithelium. (**A**) UMAP plots depicting expression of *Aqp5* and other putative cancer stem cell markers. (**B**) Duplex RNAscope of *Aqp5* with each of the putative cancer stem cell markers *Lgr5*, *Cxcr4*, and *Cd44* within Aqp5-Cre/APK mouse pyloric

tumour sections. *Aqp5* expression overlaps partially with these stem markers and also mark unique tumour compartments. $n = 3$ biological replicates; scale bars, 50μm (insets) and 200μm. (**C**) RFP tracing detected within the normal pylorus (left) and pyloric tumour (right) following Tamoxifen induction. The entire tumour epithelium is highly transformed and hyperplastic, together with robust RFP tracing. (**D**) Immunofluorescence showing the overlap between RFP and nucleocytoplasmic accumulation of β-catenin within Aqp5-Cre/APK pyloric tumour tissues. (**E**) Immunofluorescence showing the overlap between RFP and pMAPK within Aqp5-Cre/APK pyloric tumour tissues. (**F**) Principal component analysis (PCA) plot of normal AQP5+, normal AQP5-, tumour AQP5+, and tumour AQP5- bulk RNA sequencing samples, showing that these populations are highly distinct. (**G**) The majority of differentially expressed genes (DEGs) are unique to normal or tumour AQP5+ cells.

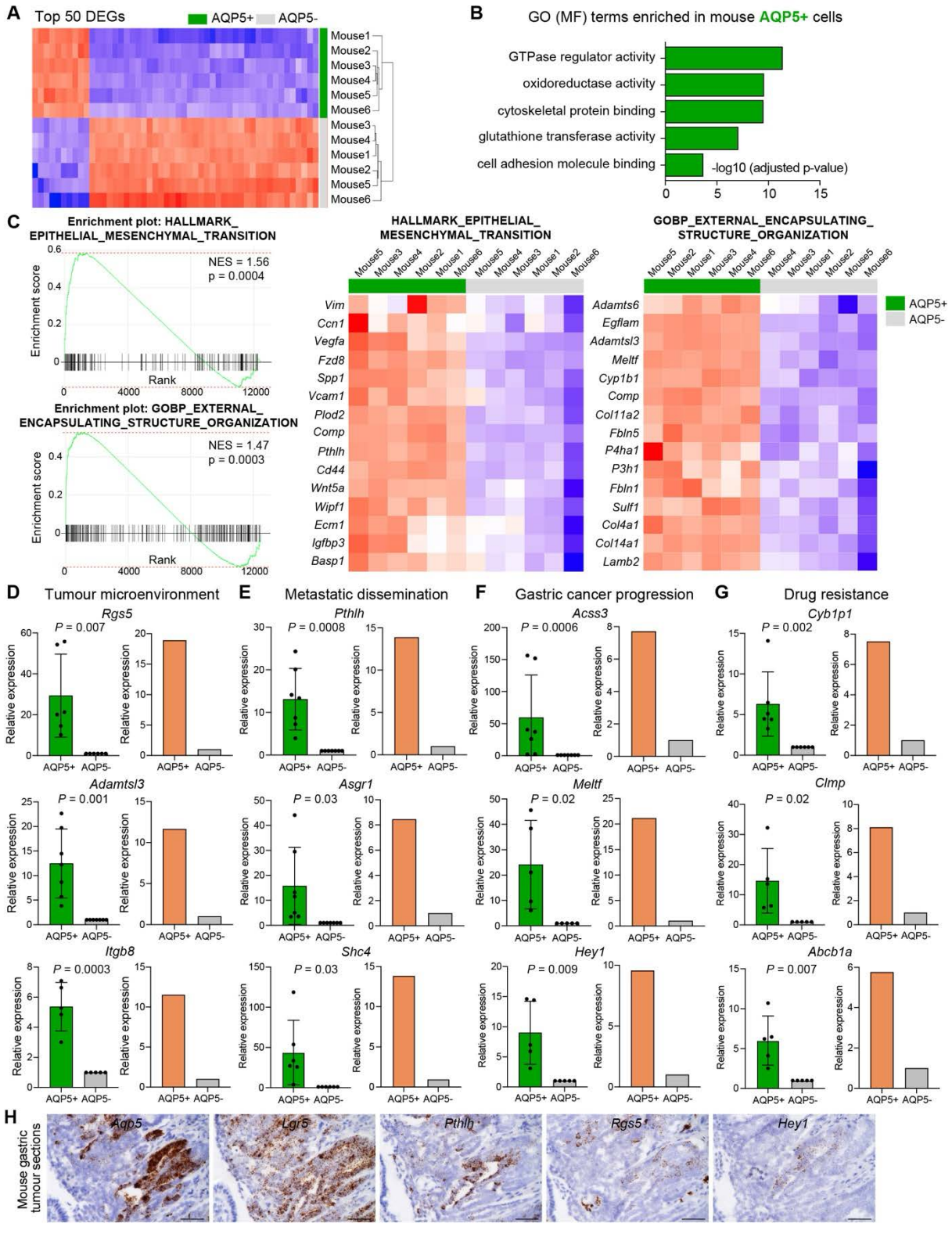
A
Top 50 DEGs
AQP5+
AQP5-
Mouse1
Mouse2
Mouse3
Mouse4
Mouse5
Mouse6
B
GO (MF) terms enriched in mouse AQP5+ cells
GTPase regulator activity
oxidoreductase activity
cytoskeletal protein binding
glutathione transferase activity
cell adhesion molecule binding
-log10 (adjusted p-value)
C
Enrichment plot: HALLMARK_ EPITHELIAL_MESENCHYMAL_TRANSITION
NES = 1.56
p = 0.0004
Enrichment score
Rank
Enrichment plot: GOBP_EXTERNAL_ ENCAPSULATING_STRUCTURE_ORGANIZATION
NES = 1.47
p = 0.0003
HALLMARK_EPITHELIAL_ MESENCHYMAL_TRANSITION
Vim
Ccn1
Vegfa
Fzd8
Spp1
Vcam1
Plod2
Comp
Pthlh
Cd44
Wnt5a
Wipf1
Ecm1
Igfbp3
Basp1
GOBP_EXTERNAL_ENCAPSULATING_ STRUCTURE_ORGANIZATION
Adamts6
Egflam
Adamtsl3
Meltf
Cyp1b1
Comp
Col11a2
Fbln5
P4ha1
P3h1
Fbln1
Sulf1
Col4a1
Col14a1
Lamb2
D
Tumour microenvironment
E
Metastatic dissemination
F
Gastric cancer progression
G
Drug resistance
Rgs5
P = 0.007
Pthlh
P = 0.0008
Acss3
P = 0.0006
Cyb1p1
P = 0.002
Adamtsl3
P = 0.001
Asgr1
P = 0.03
Meltf
P = 0.02
Clmp
P = 0.02
Itgb8
P = 0.0003
Shc4
P = 0.03
Hey1
P = 0.009
Abcb1a
P = 0.007
Relative expression
AQP5+
AQP5-
H
Mouse gastric tumour sections
Aqp5
Lgr5
Pthlh
Rgs5
Hey1

Fig. S4. Transcriptomic analyses of mouse AQP5+ and AQP5- pyloric tumour cells. (**A**) Heatmap of the top 50 differentially expressed genes (DEGs) between AQP5+ and AQP5- samples isolated from 6 independent mouse pyloric tumours. Z-score normalization was performed on the gene expression on a per gene basis. Z-scores above 0 are coloured in red while Z-scores below 0 are in blue. AQP5+ and AQP5- samples are annotated on the right using green and grey bars respectively. (**B**) Selected gene ontology (GO) terms from the molecular function (MF) category significantly enriched in the transcriptome of mouse pyloric tumour AQP5+ cells compared to AQP5- cells. The x-axis shows the negative log10 transform of the adjusted *P* values. (**C**) Gene set enrichment analysis (GSEA) of the epithelial-mesenchymal transition and external encapsulating structure organization pathways (left), with accompanying heat maps showing relative expression of selected genes within each pathway (right). (**D** to **G**) qPCR validation (left graphs) and RNAseq expression data (right graphs) of selected genes upregulated in the mouse AQP5+ cell transcriptome relating to the tumour microenvironment (D), metastatic dissemination (E), gastric cancer progression (F), and drug resistance (G). qPCR validations were performed on at least $n = 5$ additional independent samples. Graphs represent mean ± S.D. and statistical analyses were performed using two-tailed *t*-test for all genes except for *Acss3* and *Cyb1p1*, which were analysed with Mann-Whitney *U*-test. (**H**) RNAscope validation of selected targets *Lgr5*, *Pthlh*, *Rgs5*, and *Hey1* confirming their upregulation in Aqp5+ tumour cell regions in an independent mouse Aqp5-Cre/APK pyloric tumour sample. $n = 3$ independent replicates; scale bars, 100μm.

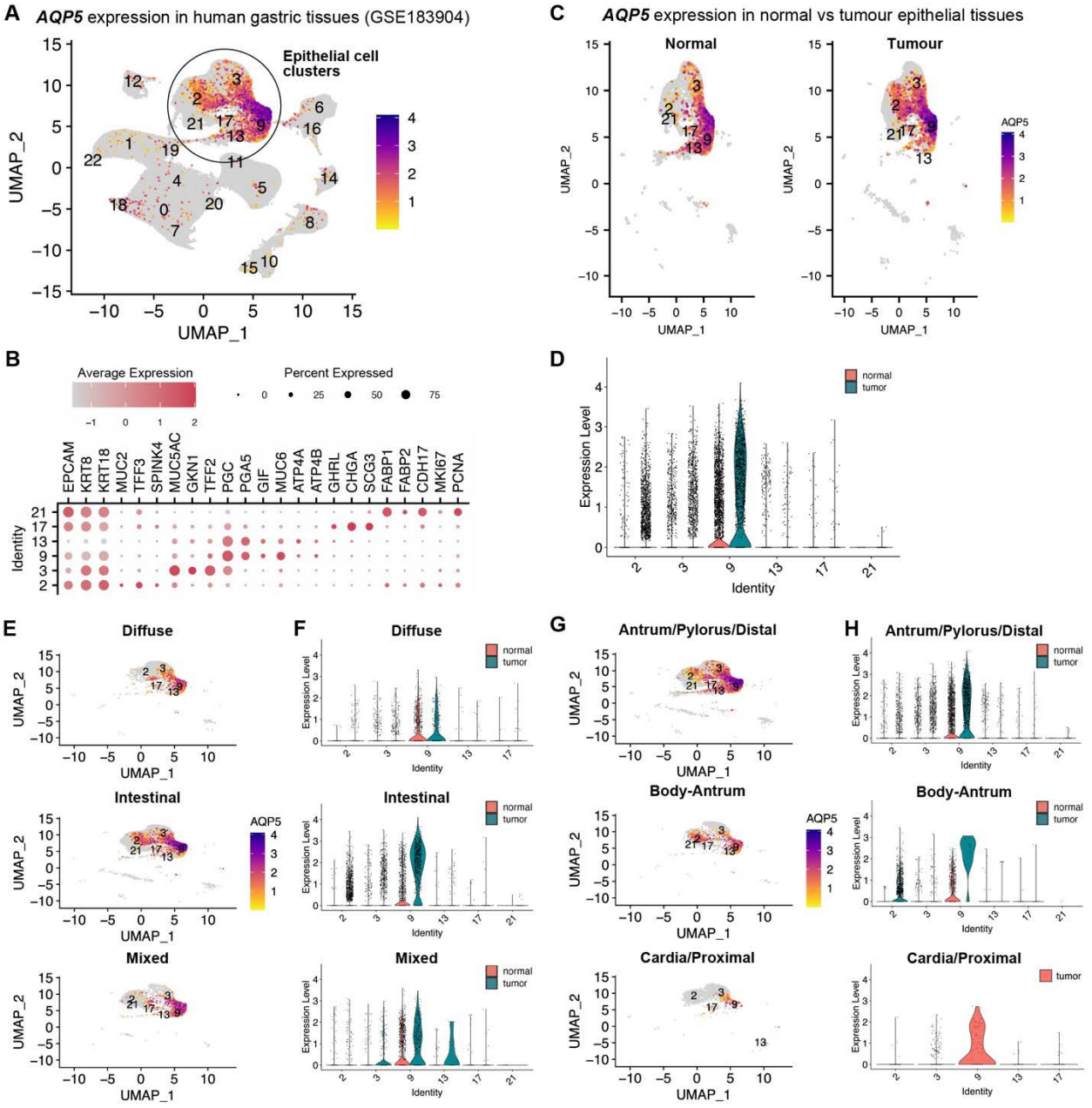

Fig. S5. *AQP5* is expressed in a subset of epithelial cells within human pyloric tumours. (**A**) UMAP plot derived from scRNAseq of healthy and tumour human gastric tissues (from GSE183904 dataset), with the epithelial cell clusters circled. (**B**) Selected markers for assigning identities to each of the 6 epithelial cell clusters. (**C**) UMAP plot showing *AQP5* expression in the epithelial cell clusters within normal (left) and tumour (right) human gastric cells. (**D**) Violin plot of *AQP5* expression in each of the epithelial clusters, showing elevated levels within tumour cell populations. (**E** and **F**) UMAP plots (E) and corresponding violin plots (F) of tumour epithelial cell clusters analysed by gastric tumour subtype: diffuse, intestinal, and mixed. (**G** and **H**) UMAP plots (G) and corresponding violin plots (H) of tumour epithelial cell clusters analysed by tumour location: antrum/pylorus/distal, body-antrum, and cardia/proximal.

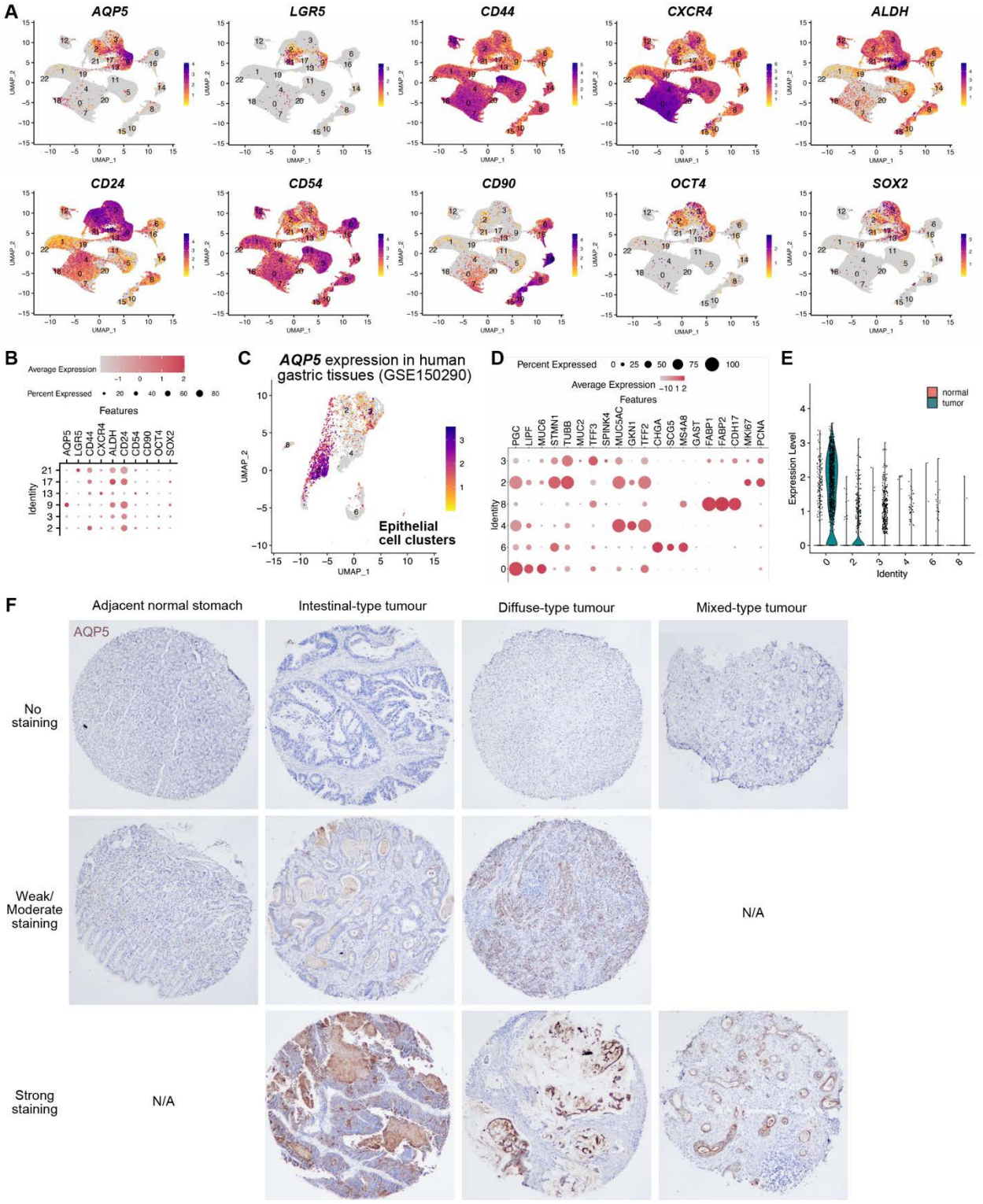

Fig. S6. *AQP5* enriches for a unique cancer stem cell population within human pyloric tumours. (**A**) UMAP plots depicting expression of *AQP5* and other putative cancer stem cell markers. Many markers show broad enrichment across epithelial and non-epithelial clusters. (**B**) Dotplot showing expression of the same 10 markers across the epithelial clusters. (**C**) UMAP plot

of epithelial cell clusters derived from a second scRNAseq dataset (GSE150290) of healthy and tumour human gastric samples. (**D**) Selected markers for assigning identities to the epithelial cell clusters in (C). (**E**) Violin plot of *AQP5* expression in each of the epithelial clusters identified in (C) showing elevated levels within tumour populations. (**F**) Representative images of tissue microarray cores presenting negative, weak/moderate, or strong staining of AQP5 in human stomach tissues, including adjacent normal stomach and gastric tumours across intestinal, diffuse, and mixed subtypes.

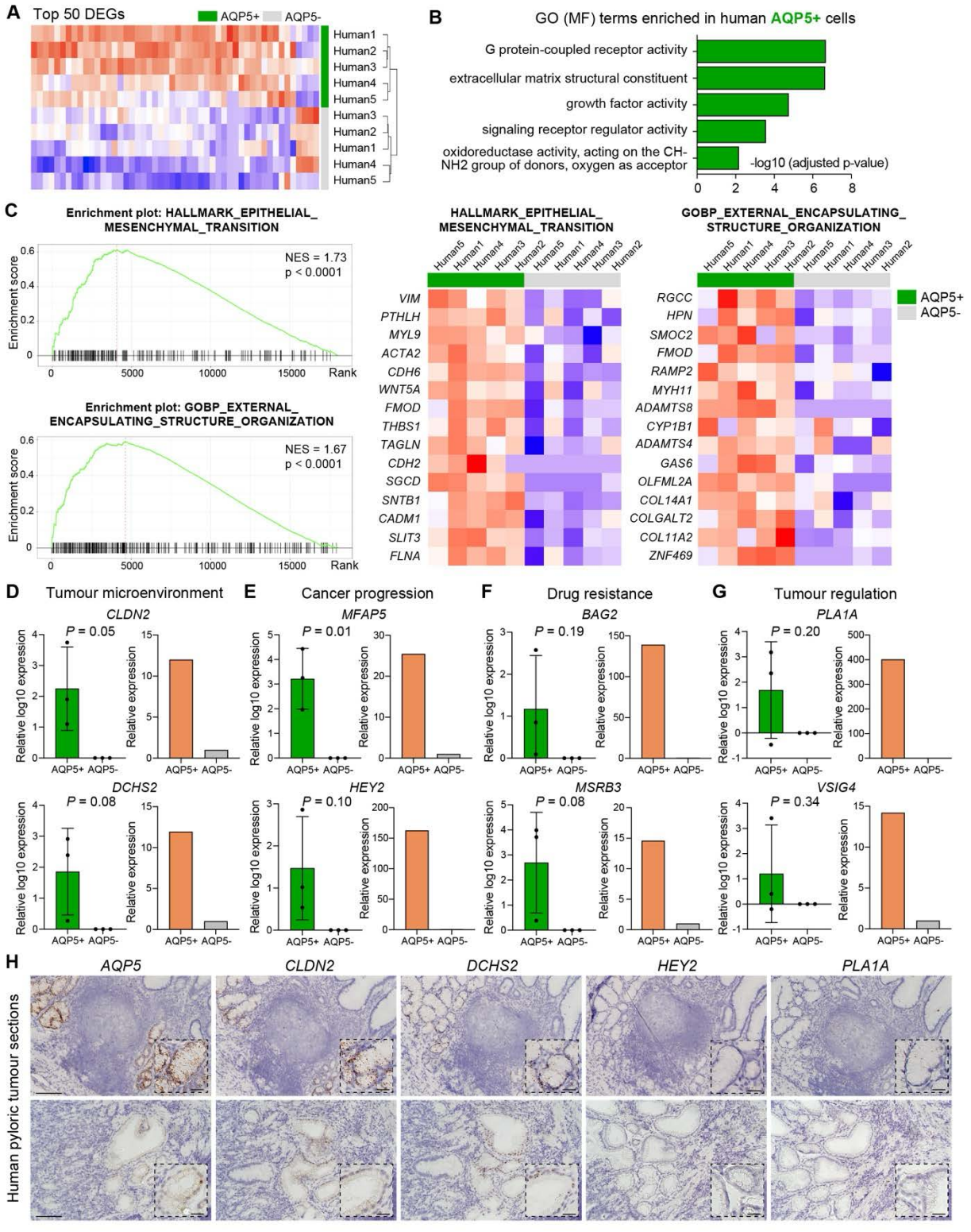
A
Top 50 DEGs
AQP5+
AQP5-
Human1
Human2
Human3
Human4
Human5
Human3
Human2
Human1
Human4
Human5
B
GO (MF) terms enriched in human AQP5+ cells
G protein-coupled receptor activity
extracellular matrix structural constituent
growth factor activity
signaling receptor regulator activity
oxidoreductase activity, acting on the CH-NH2 group of donors, oxygen as acceptor
-log10 (adjusted p-value)
0
2
4
6
8
C
Enrichment plot: HALLMARK_EPITHELIAL_MESENCHYMAL_TRANSITION
NES = 1.73
p < 0.0001
Enrichment score
Rank
Enrichment plot: GOBP_EXTERNAL_ENCAPSULATING_STRUCTURE_ORGANIZATION
NES = 1.67
p < 0.0001
HALLMARK_EPITHELIAL_MESENCHYMAL_TRANSITION
VIM
PTHLH
MYL9
ACTA2
CDH6
WNT5A
FMOD
THBS1
TAGLN
CDH2
SGCD
SNTB1
CADM1
SLIT3
FLNA
GOBP_EXTERNAL_ENCAPSULATING_STRUCTURE_ORGANIZATION
RGCC
HPN
SMOC2
FMOD
RAMP2
MYH11
ADAMTS8
CYP1B1
ADAMTS4
GAS6
OLFML2A
COL14A1
COLGALT2
COL11A2
ZNF469
AQP5+
AQP5-
D
Tumour microenvironment
CLDN2
P = 0.05
DCHS2
P = 0.08
E
Cancer progression
MFAP5
P = 0.01
HEY2
P = 0.10
F
Drug resistance
BAG2
P = 0.19
MSRB3
P = 0.08
G
Tumour regulation
PLA1A
P = 0.20
VSIG4
P = 0.34
Relative log10 expression
Relative expression
H
AQP5
CLDN2
DCHS2
HEY2
PLA1A
Human pyloric tumour sections

Fig. S7. Transcriptomic analyses of human AQP5+ and AQP5- pyloric tumour cells. (**A**) Heatmap of the top 50 DEGs between AQP5+ and AQP5- samples isolated from 5 independent human pyloric tumours. *Z*-score normalization was performed on the gene expression on a per gene basis. *Z*-scores above 0 are coloured in red while *Z*-scores below 0 are in blue. AQP5+ and AQP5- samples are annotated on the right using green and grey bars respectively. (**B**) Selected gene ontology (GO) terms from the molecular function (MF) category significantly enriched in the transcriptome of human pyloric tumour AQP5+ cells compared to AQP5- cells. The x-axis shows the negative log10 transform of the adjusted *P* values. (**C**) Gene set enrichment analysis (GSEA) of the epithelial-mesenchymal transition and external encapsulating structure organization pathways (left), with accompanying heat maps showing relative expression of selected genes within each pathway (right). (**D** to **G**) qPCR validation (left graphs) and RNAseq expression data (right graphs) of selected genes upregulated in the human AQP5+ cell transcriptome relating to the tumour microenvironment (D), cancer progression (E), drug resistance (F), and tumour regulation (G). (**H**) RNAscope validation of selected targets *CLDN2*, *DCHS2*, *HEY2*, and *PLA1A* confirming their upregulation in *AQP5*+ tumour cell regions in an additional independent human pyloric tumour sample. Scale bars, 20μm (insets), 100μm. Graphs represent mean ± S.D. with two-tailed unpaired *t*-test.

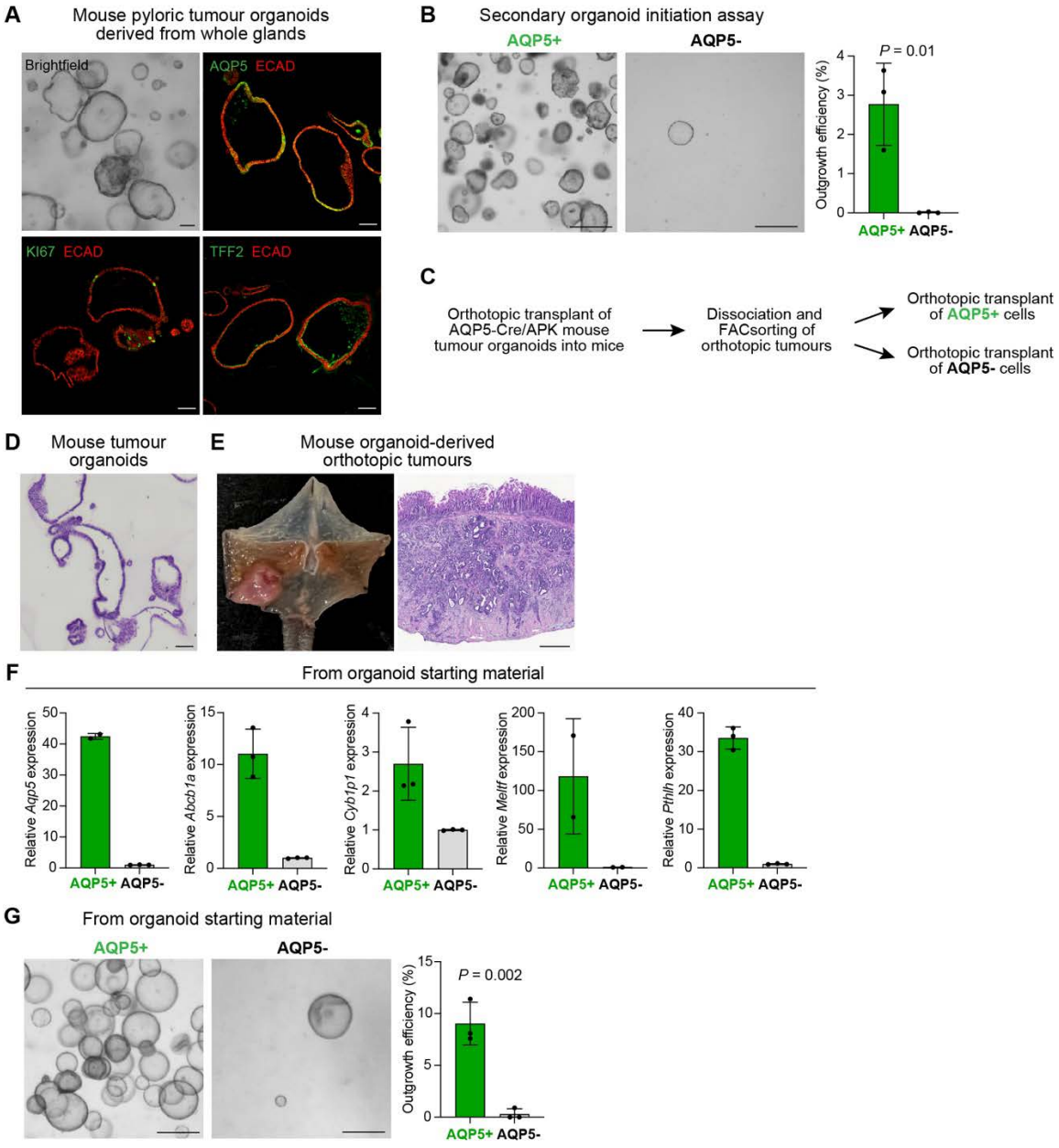

Fig. S8. Mouse AQP5+ cells function as gastric cancer stem cells in both primary tumours and organoid models. (**A**) Representative brightfield and immunofluorescence images of mouse Aqp5-Cre/APK pyloric tumour organoids generated from whole glands, showing expression of AQP5 and gastric lineage markers. $n = 3$ biological replicates; scale bars, 100µm. (**B**) AQP5+ cells isolated from AQP5+ cell-derived organoids continue to seed new organoids more efficiently than their AQP5- counterparts. $n = 3$ biological replicates; scale bars, 500µm. (**C**) Experimental workflow for generating orthotopic tumours from transplantation of mouse pyloric tumour organoids, isolating AQP5+ and AQP5- cells by FACS, and re-transplanting these cells into immune-deficient mice. (**D**) Histology of mouse Aqp5-Cre/APK pyloric tumour organoids as assessed by H&E. $n = 3$ biological replicates; scale bars, 100µm. (**E**) Histology of orthotopic tumours generated from transplanting mouse Aqp5-Cre/APK pyloric tumour organoids, visualised

by whole mount (left) and H&E (right). *n* = 3 biological replicates; scale bars, 1mm. (**F**) qPCR of selected targets performed on sorted AQP5+ and AQP5- cells derived from mouse Aqp5-Cre/APK pyloric tumour organoids, confirming enrichment of *Aqp5*, chemoresistance genes (*Abcb1a* and *Cyb1p1*), and genes involved in cancer progression (*Meltf* and *Pthlh*) within the AQP5+ population, similar to expression patterns in sorted AQP5+ and AQP5- cells from primary mouse tumours. (**G**) Isolated AQP5+ cells from mouse Aqp5-Cre/APK pyloric tumour organoids establish organoids more efficiently than AQP5- cells, indicative of stem potential. *n* = 3 biological replicates; scale bars, 500μm. Graphs represent mean ± S.D. with two-tailed unpaired *t*-test.

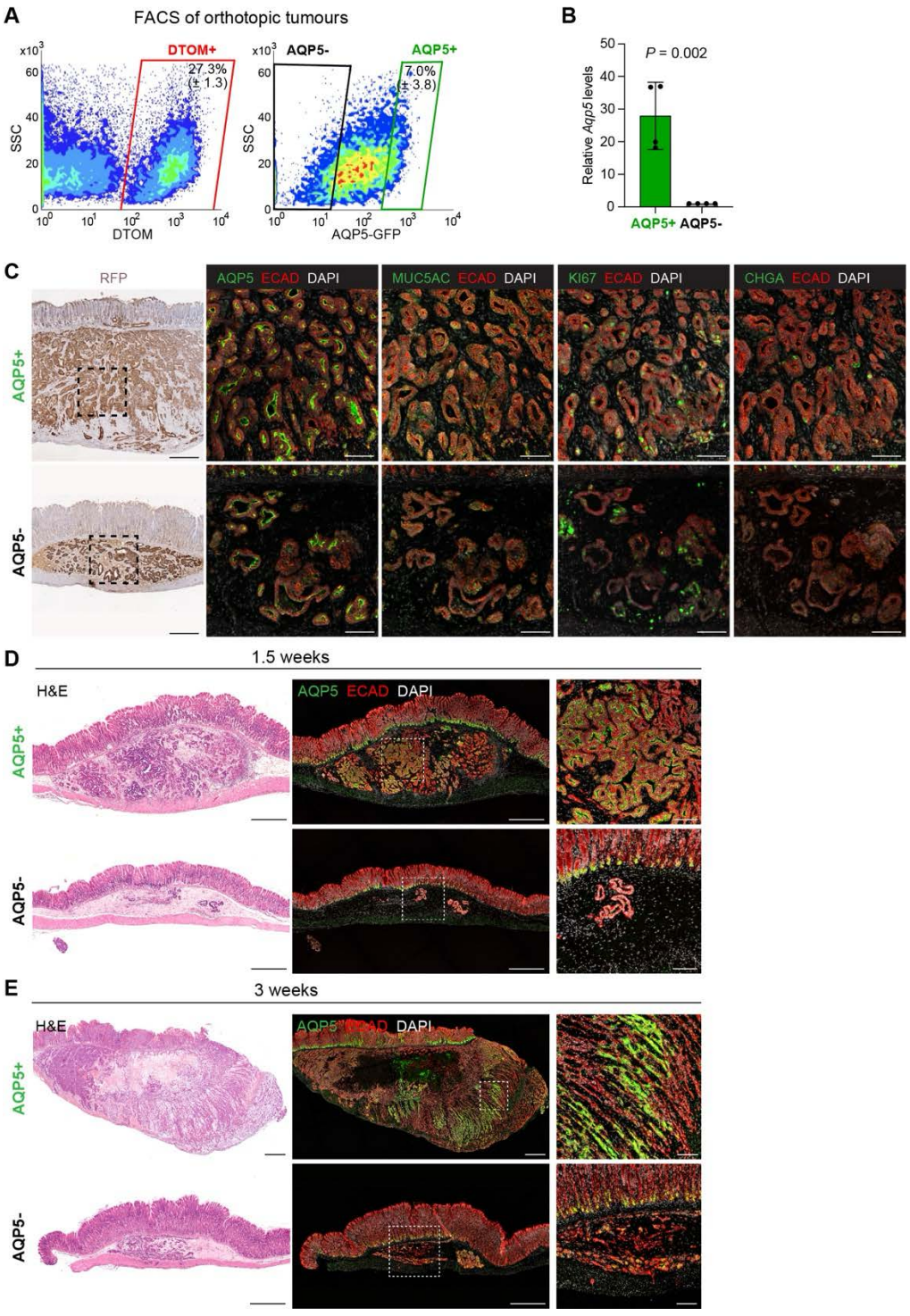

Fig. S9. Mouse AQP5+ cells establish tumours following transplantation. (**A**) FACS gating strategy for isolating tumour epithelial (DTOM+) AQP5+ and AQP5- cells from orthotopic mouse tumours. SSC, side scatter. n = 5 biological replicates. (**B**) Relative *Aqp5* expression in sorted mouse tumour cell populations by qPCR. (**C**) Histology of orthotopic tumours derived from transplanted tumour epithelial AQP5+ and AQP5- cells, 3 weeks post-transplantation. RFP immunohistochemistry highlights the location of the transplanted cells within the gastric mucosa

(left). AQP5+ cell-derived tumours are larger than their AQP5- counterparts and display tumour cell invasion into the adjacent epithelial and muscle layers. Immunofluorescence for AQP5, MUC5AC, KI67, and CHGA shows that AQP5+ cell-derived tumours express both stem and differentiated lineage markers (right). n = 5 biological replicates; scale bars, 1mm (left), 250μm (right). (**D**) Representative tissues showing transplanted mouse AQP5+ and AQP5- cells 1.5 weeks after transplant. Robust AQP5 expression is detected within the transplanted AQP5+ population and absent from the transplanted AQP5- population. n = 3 independent replicates; scale bars, 1mm (left and middle), 200μm (right insets). (**E**) By 3 weeks, transplanted AQP5+ cells have developed into highly invasive, advanced tumours, whereas transplanted AQP5- cells are retained within the submucosal space. Some AQP5- cells also start to turn on expression of AQP5. n = 3 independent replicates; scale bars, 1mm (left and middle), 200μm (right insets). Graphs represent mean ± S.D. with two-tailed unpaired t-test.

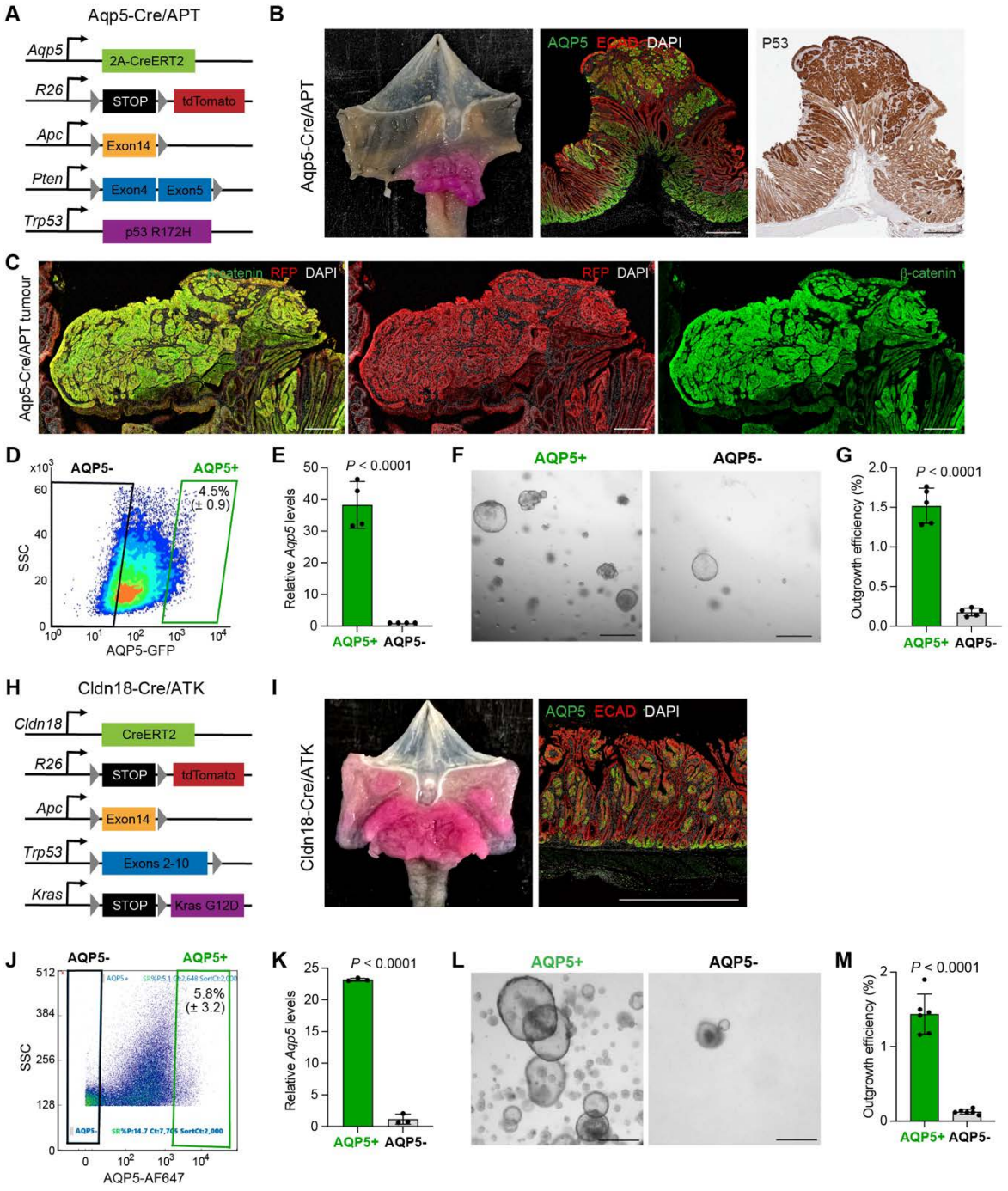

Fig. S10. Mouse AQP5+ cells function as gastric cancer stem cells in two additional mouse models of pyloric cancer. (**A**) Alleles present in the *Aqp5-2A-CreERT2; Apc$^{fl/fl}$; Pten$^{fl/fl}$; Trp53$^{R172H/+}$; Rosa26-tdTomato^{LSL}* conditional genetic mouse model for pyloric cancer (Aqp5-Cre/APT in short). (**B**) Representative images of pyloric tumours generated from the Aqp5-Cre/APT mouse model, confirming P53 mutant expression (right) and the presence of AQP5+ cells in a subset of tumour cells (middle). n = 3 biological replicates; scale bars, 1mm. (**C**) Co-immunofluorescence confirms overlap between RFP and nucleocytoplasmic accumulation of β-catenin, highlighting the specificity of RFP for transformed tumour cells. (**D**) FACS gating strategy

for isolating tumour epithelial AQP5+ and AQP5- cells from P53 mutant mouse pyloric tumours. SSC, side scatter. n = 5 biological replicates. (**E**) Relative *Aqp5* expression in sorted tumour cell populations by qPCR. (**F**) Organoids generated from FACS-sorted Aqp5-Cre/APT mouse tumour AQP5+ and AQP5- cells, with organoids forming more readily from AQP5+ cells. n = 5 biological replicates; scale bars, 500μm. (**G**) Organoid outgrowth efficiency of Aqp5-Cre/APT mouse tumour AQP5+ and AQP5- cells. n = 5 biological replicates. (**H**) Alleles present in the *Cldn18-CreERT2; Apc*$^{fl/fl}$*; Trp53*$^{fl/fl}$*; Kras*$^{G12D/+}$*; Rosa26-tdTomato*^{LSL} conditional genetic mouse model for pyloric cancer (Cldn18-Cre/ATK in short). (**I**) Representative images of pyloric tumours generated from the Cldn18-Cre/ATK mouse model confirming the presence of AQP5+ cells in a subset of tumour cells. n = 3 biological replicates; scale bars, 1mm. (**J**) FACS gating strategy for isolating tumour epithelial AQP5+ and AQP5- cells from Cldn18-Cre/ATK mouse pyloric tumour organoids. SSC, side scatter. n = 5 biological replicates. (**K**) Relative *Aqp5* expression in sorted tumour cell populations by qPCR. (**L**) Organoids generated from FACS-sorted Cldn18-Cre/ATK mouse tumour AQP5+ and AQP5- cells, with organoids forming more readily from AQP5+ cells. n = 5 biological replicates; scale bars, 500μm. (**M**) Organoid outgrowth efficiency of Cldn18-Cre/ATK mouse tumour AQP5+ and AQP5- cells. n = 5 biological replicates. Graphs represent mean ± S.D. with two-tailed unpaired t-test.

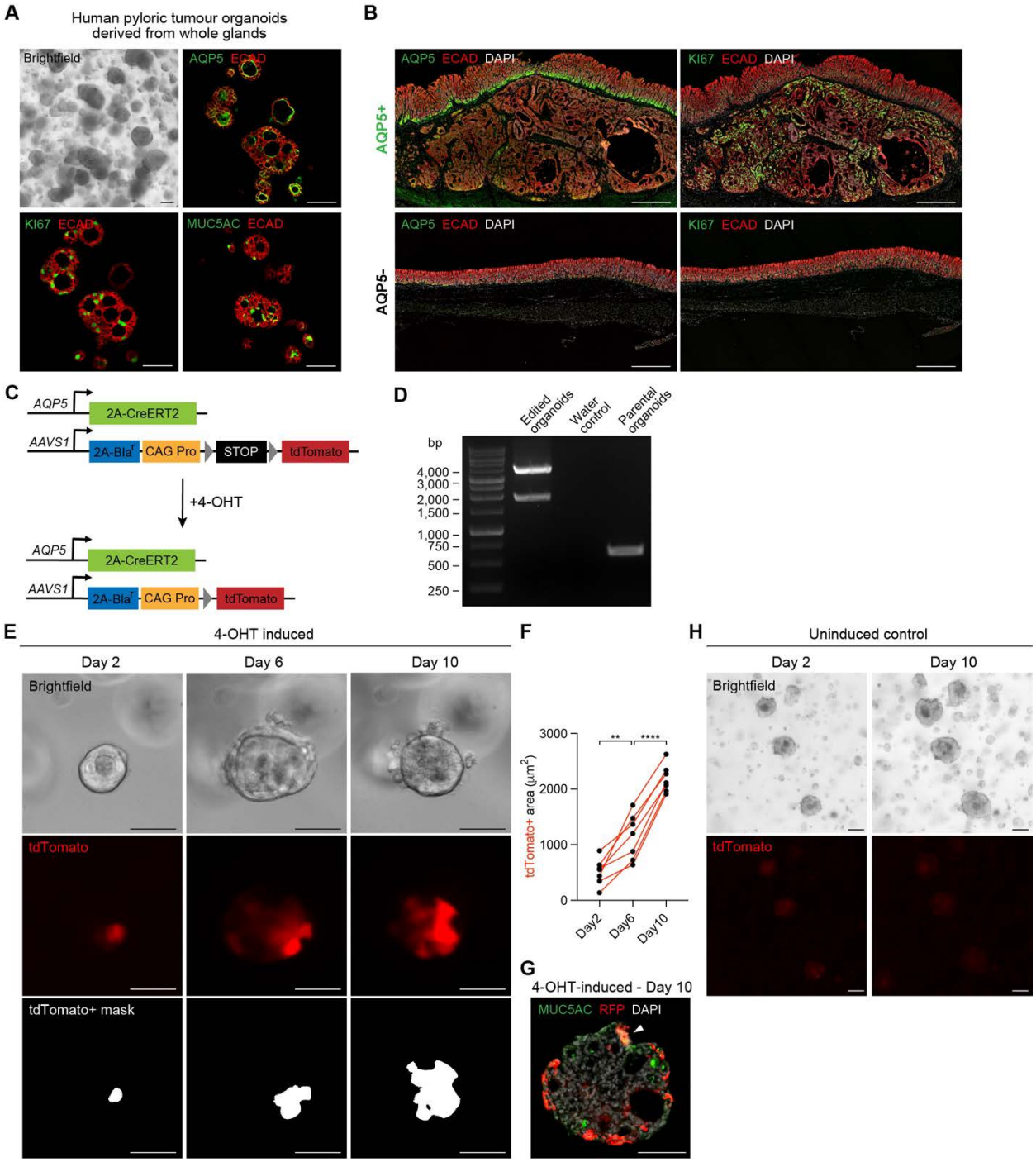

Fig. S11. Human AQP5+ cells function as gastric cancer stem cells. (**A**) Representative brightfield and immunofluorescence images of human pyloric tumour organoids generated from whole glands, highlighting the expression of AQP5 and multiple gastric lineage markers. $n = 3$ independent replicates; scale bars, 100µm. (**B**) Immunofluorescence confirms expression of AQP5 within tumours derived from transplanted AQP5+ cells, which are also highly proliferative with elevated KI67 levels. $n = 3$ independent replicates; scale bars, 1mm. (**C**) Schematic of the *AQP5-2A-CreERT2; AAVS1-CAG-tdTomato*^{LSL} constructs inserted into human gastric cancer organoids

and strategy for lineage tracing of AQP5+ CSCs and their progeny. Administration of 4-hydroxytamoxifen (4-OHT) results in the removal of the STOP codon (black rectangle) flanked by loxP sites (grey triangles) and expression of the tdTomato reporter (red rectangle). (**D**) Genomic PCR performed at the insertion site of *AQP5-2A-CreERT2* confirms successful insertion based on expected band size. (**E**) 4-OHT induction performed in *AQP5-2A-CreERT2; AAVS1-CAG-tdTomato*^{LSL} organoids results in the visible tdTomato labelling of a small pool of cells by day 2, which expands over time. $n = 7$ independent replicates; scale bars, 50μm. (**F**) Quantification of the expansion of tdTomato-labelled clone area within each organoid over time. Statistical analyses were performed using one-way ANOVA with Tukey's multiple comparisons test. $^{**}P = 0.003$, $^{****}P < 0.0001$. (**G**) Co-immunofluorescence confirms the overlap of tdTomato-labelled cells with differentiated lineage marker MUC5AC in organoids 10 days post-induction. $n = 3$ independent replicates; scale bars, 100μm. (**H**) Uninduced *AQP5-2A-CreERT2; AAVS1-CAG-tdTomato*^{LSL} organoids never show visible signs of tdTomato tracing over the same analysed timepoints. $n = 3$ independent replicates; scale bars, 100μm.

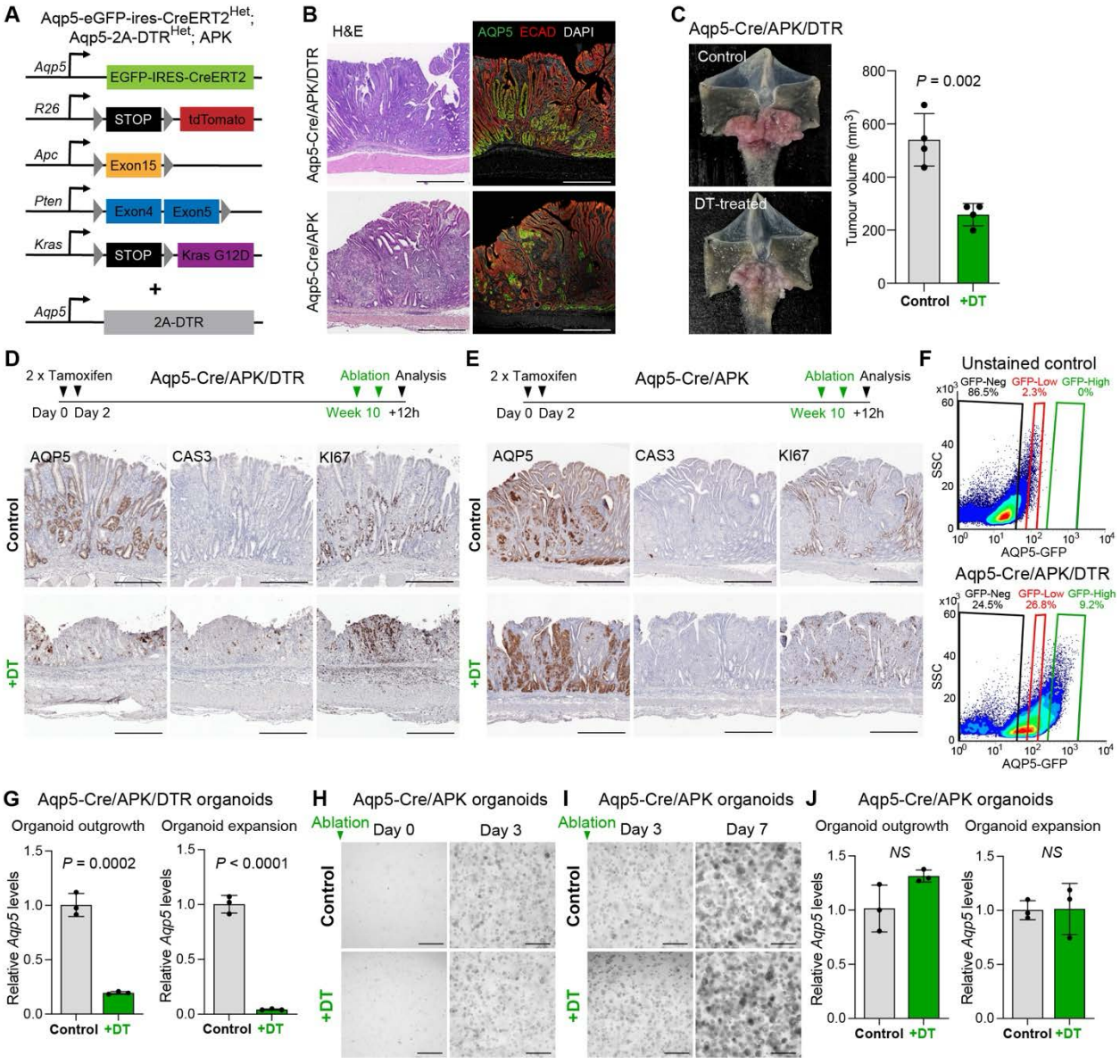

Fig. S12. Ablation of AQP5+ cells within organoid and mouse pyloric tumour models confirms their requirement for tumour initiation and progression. (**A**) Schematic of the *Aqp5-eGFP-ires-CreERT2; Apc$^{fl/fl}$; Pten$^{fl/fl}$; Kras$^{LSL-G12D/+}$; Rosa26-tdTomato^{LSL}* conditional genetic mouse model for pyloric cancer with the addition of a *Aqp5-2A-DTR* cassette (Aqp5-Cre/APK/DTR in short) to facilitate diphtheria toxin (DT)-mediated targeted ablation of Aqp5+ cells. (**B**) Representative images show that Aqp5-Cre/APK and Aqp5-Cre/APK/DTR mouse pyloric tumours are comparable in terms of histological features and AQP5 expression. n = 3 biological replicates; scale bars, 1mm. (**C**) Intraperitoneal DT administration to 10-week Aqp5-Cre/APK/DTR mouse pyloric tumours results in an approximately 50% reduction in tumour volume. Representative whole mount images of control and DT-treated tumours are shown on the left. n = 4 biological replicates. (**D**) Timeline of DT administration 10 weeks after induction of tumour formation and analysis of tumour tissues 12h following ablation in Aqp5-Cre/APK/DTR mice (top). Representative immunohistochemistry images confirm the loss of AQP5+ cells in DT-

treated Aqp5-Cre/APK/DTR tumours accompanied by an increase in CAS3 and KI67 expression in the remaining tumour load (bottom). *n* = 3 biological replicates; scale bars, 1mm. (**E**) Timeline of DT administration 10 weeks after induction of tumour formation and analysis of tumour tissues 12h following ablation in Aqp5-Cre/APK mice lacking the *Aqp5-2A-DTR* allele (top). Representative immunohistochemistry images show that control and DT-treated tumours present comparable levels of AQP5, CAS3, and KI67 (bottom). *n* = 3 biological replicates; scale bars, 1mm. (**F**) FACS analysis confirms the staining results that approximately 9% of cells within Aqp5-Cre/APK/DTR organoids express high levels of AQP5-GFP. A mouse pyloric tumour organoid line lacking AQP5-GFP was used as an unstained control to set the FACS gates in the profile. (**G**) DT treatment of Aqp5-Cre/APK/DTR organoids results in an 80% and 95% decrease in *Aqp5* transcript levels relative to control untreated organoids during the organoid outgrowth and organoid expansion phases respectively. (**H** and **I**) DT treatment of Aqp5-Cre/APK organoids lacking the *Aqp5-2A-DTR* allele on day 0 does not affect organoid outgrowth (H), and treatment on day 3 does not affect subsequent organoid expansion (I). *n* = 3 independent replicates; scale bars, 500μm. (**J**) DT treatment of Aqp5-Cre/APK organoids lacking the *Aqp5-2A-DTR* allele does not affect *Aqp5* transcript levels at both the organoid outgrowth and organoid expansion phases by qPCR. Graphs represent mean ± S.D. with two-tailed unpaired *t*-test.

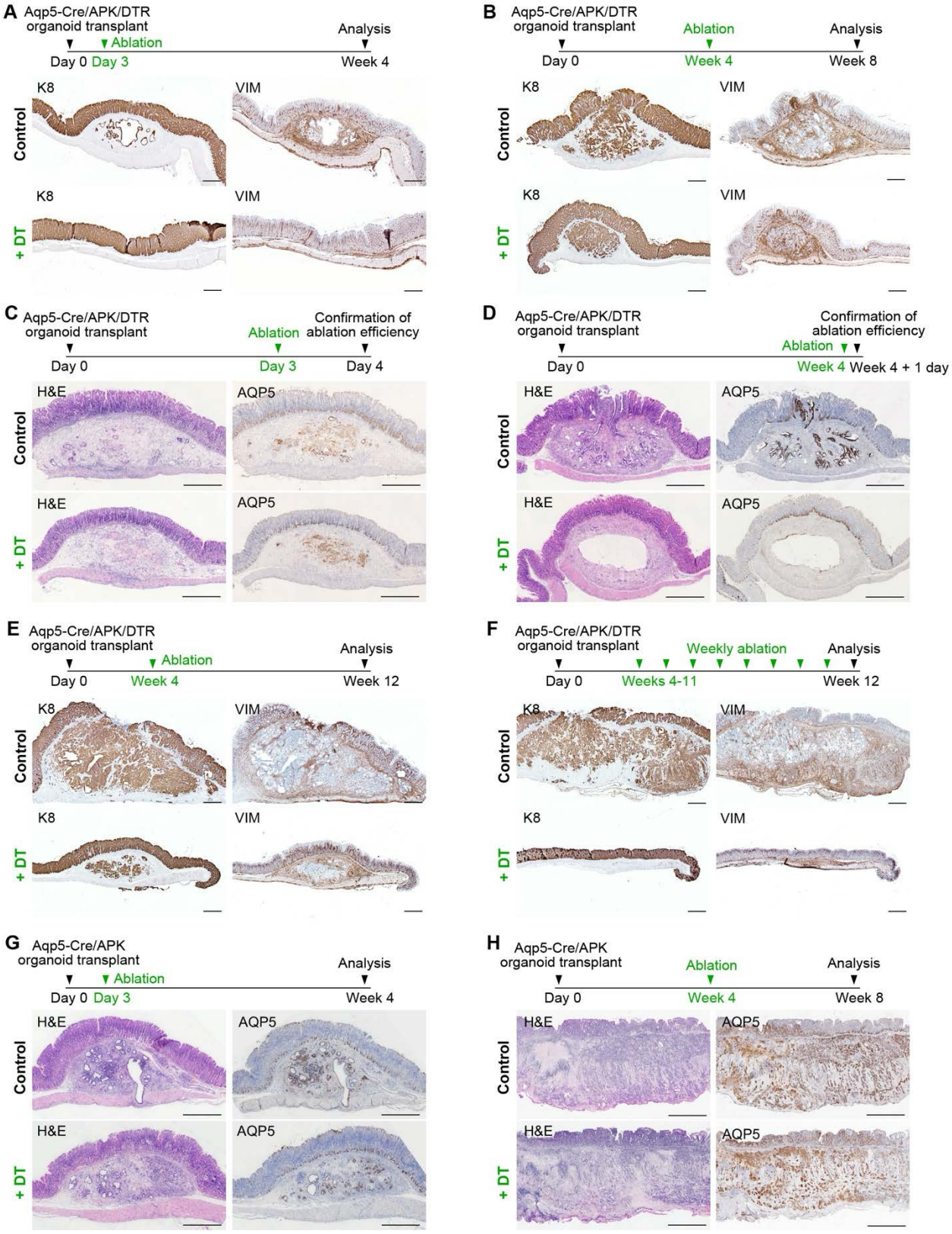
A
Aqp5-Cre/APK/DTR
organoid transplant
Ablation
Analysis
Day 0
Day 3
Week 4
K8
VIM
Control
+ DT
B
Aqp5-Cre/APK/DTR
organoid transplant
Ablation
Analysis
Day 0
Week 4
Week 8
C
Aqp5-Cre/APK/DTR
organoid transplant
Ablation
Confirmation of
ablation efficiency
Day 0
Day 3
Day 4
H&E
AQP5
D
Aqp5-Cre/APK/DTR
organoid transplant
Confirmation of
ablation efficiency
Ablation
Day 0
Week 4
Week 4 + 1 day
E
Aqp5-Cre/APK/DTR
organoid transplant
Ablation
Analysis
Day 0
Week 4
Week 12
F
Aqp5-Cre/APK/DTR
organoid transplant
Weekly ablation
Analysis
Day 0
Weeks 4-11
Week 12
G
Aqp5-Cre/APK
organoid transplant
Ablation
Analysis
Day 0
Day 3
Week 4
H
Aqp5-Cre/APK
organoid transplant
Ablation
Analysis
Day 0
Week 4
Week 8

Fig. S13. Ablation of AQP5+ cells within mouse orthotopic tumour models confirms their requirement for tumour initiation and progression. (**A** and **B**) Representative images of tumour histology shown by Keratin 8 (K8) and Vimentin (VIM) immunohistochemistry in control and DT-treated animals at 4 weeks following an early ablation (A) or at 8 weeks following ablation at 4 weeks (B). *n* = 3 biological replicates; scale bars, 1mm. (**C** and **D**) Representative images of tumour histology shown by H&E and AQP5 immunohistochemistry in control and DT-treated animals confirming that AQP5 expression was lost and/or perturbed 1 day following ablation either 3 days (C) or 4 weeks (D) after transplantation of Aqp5-Cre/APK/DTR organoids. *n* = 3 biological replicates; scale bars, 1mm. (**E** and **F**) Representative images of tumour histology shown by Keratin 8 (K8) and Vimentin (VIM) immunohistochemistry in control and DT-treated animals 12 weeks post-transplant following ablation at 4 weeks (E) or weekly ablations from weeks 4 to 11 (F). *n* = 3 biological replicates; scale bars, 1mm. (**G** and **H**) Representative images of tumour histology shown by H&E and AQP5 immunohistochemistry confirm that DT administration did not affect tumour load or AQP5 expression 4 weeks (G) or 8 weeks (H) following transplantation of Aqp5-Cre/APK organoids lacking the *Aqp5-2A-DTR* allele. *n* = 3 biological replicates; scale bars, 1mm.

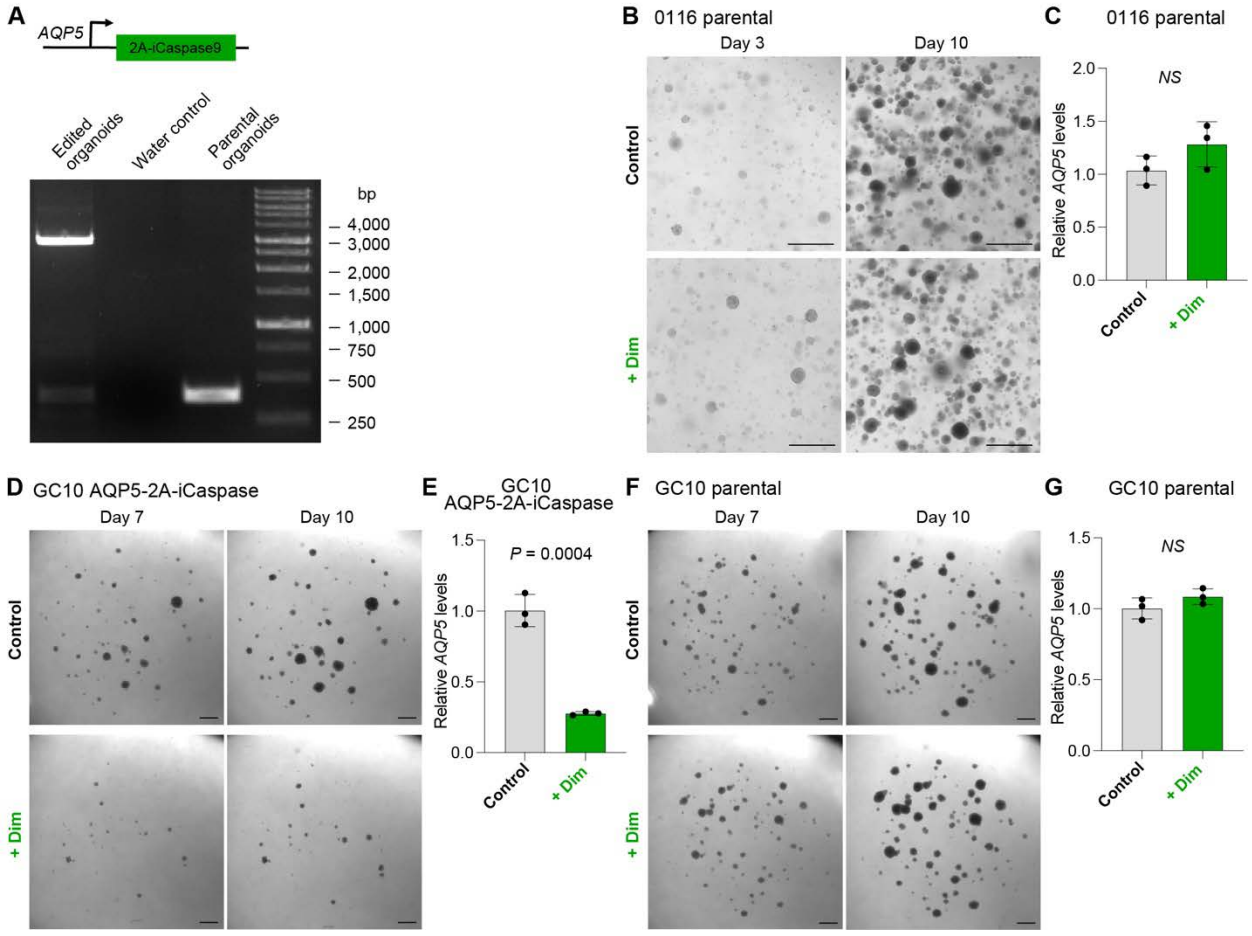

Fig. S14. Ablation of human AQP5+ cells within gastric cancer organoid models confirms their requirement for tumour progression. (**A**) Genomic PCR performed at the insertion site of *AQP5-2A-iCaspase* confirms successful insertion based on expected band size. (**B**) Dimerizer treatment (+Dim) of unedited parental organoids does not alter organoid initiation or subsequent growth tracked over 10 days in culture. $n = 3$ independent replicates; scale bars, 500µm. (**C**) qPCR shows that *AQP5* transcript levels are comparable in control and dimerizer-treated parental organoids lacking *AQP5-2A-iCaspase*. (**D**) Ablation of AQP5+ cells in an independent GC10 *AQP5-2A-iCaspase* organoid line recapitulates the reduced growth rates. $n = 3$ independent replicates; scale bars, 500µm. (**E**) Dimerizer treatment (+Dim) of GC10 *AQP5-2A-iCaspase* organoids results in a 70% decrease in *AQP5* levels relative to control untreated organoids. (**F**) Dimerizer treatment (+Dim) of unedited GC10 parental organoids does not alter organoid initiation or subsequent growth tracked over 10 days in culture. $n = 3$ independent replicates; scale bars, 500µm. (**G**) *AQP5* transcript levels are comparable in control versus dimerizer-treated GC10 parental organoids by qPCR. Graphs represent mean ± S.D. with two-tailed unpaired *t*-test.

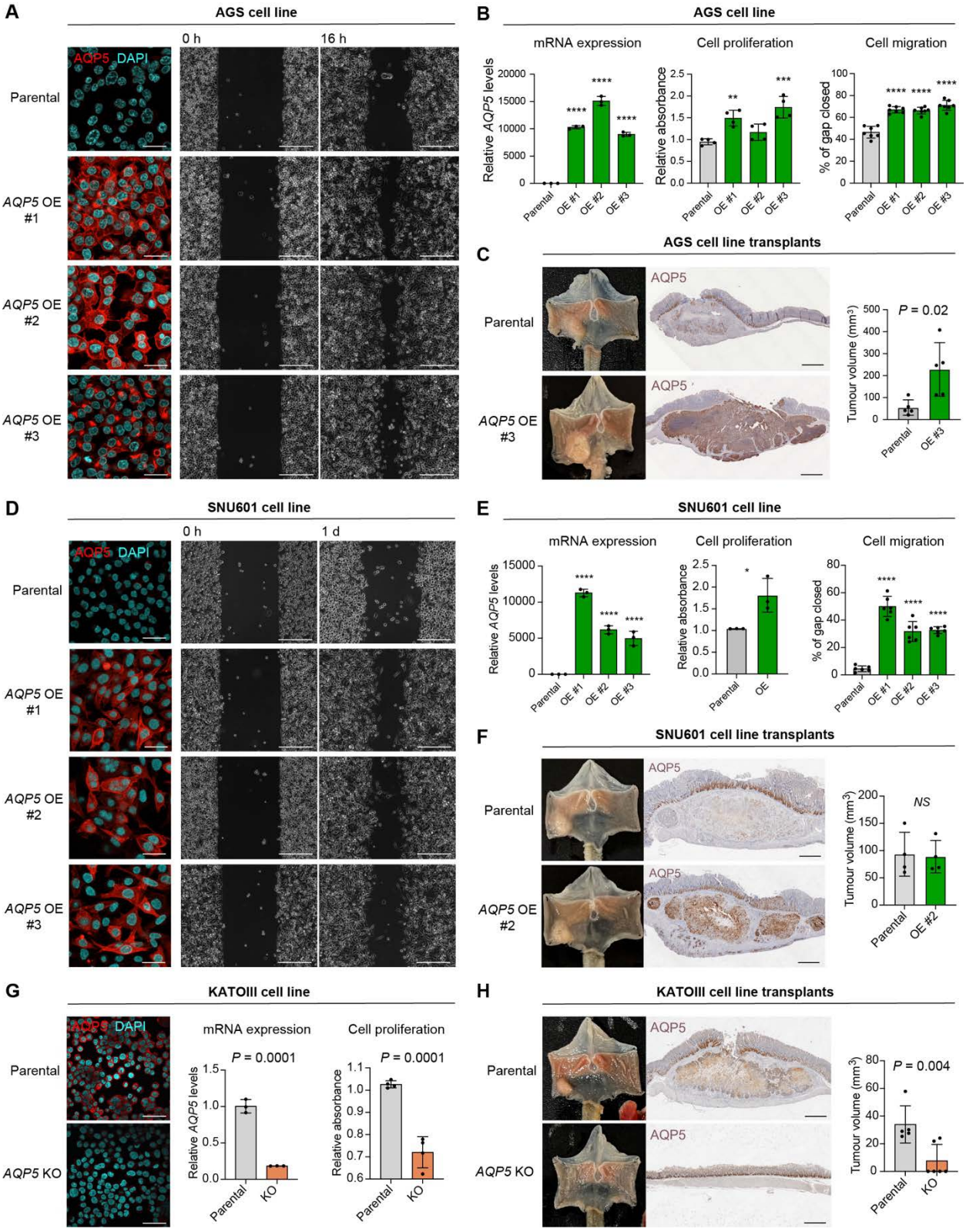
A
AGS cell line
0 h
16 h
AQP5 DAPI
Parental
AQP5 OE #1
AQP5 OE #2
AQP5 OE #3
B
AGS cell line
mRNA expression
Cell proliferation
Cell migration
Relative AQP5 levels
Relative absorbance
% of gap closed
Parental
OE #1
OE #2
OE #3
C
AGS cell line transplants
AQP5
Parental
AQP5 OE #3
Tumour volume (mm3)
P = 0.02
D
SNU601 cell line
0 h
1 d
E
SNU601 cell line
F
SNU601 cell line transplants
NS
G
KATOIII cell line
P = 0.0001
AQP5 KO
KO
H
KATOIII cell line transplants
P = 0.004

Fig. S15. AQP5 drives tumour progression across multiple human gastric cancer cell lines. (**A**) Representative immunofluorescence images show the upregulation of AQP5 expression across three independent *AQP5* overexpressing (OE) AGS clones and *in vitro* migration assays show that *AQP5* OE clones have higher cell migration rates in culture. (**B**) qPCR confirms the upregulation of *AQP5* mRNA levels in all three AGS *AQP5* OE clones and quantifications show that these *AQP5* OE clones also have higher cell proliferation and cell migration rates in culture, relative to the parental AGS cell line. Statistical analyses were performed using one-way ANOVA with Dunnett's multiple comparisons test. $^{**}P = 0.003$, $^{***}P = 0.0002$, $^{****}P < 0.0001$; scale bars, 500μm. (**C**) AGS *AQP5* OE cells establish orthotopic tumours in mice that are larger and display more aggressive tumour features, compared to AGS parental cells. $n = 5$ biological replicates; scale bars, 1mm. (**D**) Representative immunofluorescence images show the upregulation of AQP5 in three independent *AQP5* OE SNU601 clones and *in vitro* migration assays show that *AQP5* OE clones have higher cell migration rates in culture. (**E**) qPCR confirms the upregulation of *AQP5* mRNA levels in the *AQP5* OE clones and quantifications show that *AQP5* OE clones also have higher cell proliferation and cell migration rates in culture. Statistical analyses were performed using one-way ANOVA with Dunnett's multiple comparisons test. $^{*}P = 0.03$, $^{****}P < 0.0001$; scale bars, 500μm. (**F**) No detectable difference in tumour volumes from orthotopic tumours established from SNU601 parental and SNU601 *AQP5* OE cells. $n = 4$ biological replicates; scale bars, 1mm. (**G**) Representative immunofluorescence images and qPCR of *AQP5* levels confirm the loss of *AQP5* in *AQP5* knockout (KO) KATOIII cells (left). *In vitro* assays show that KATOIII *AQP5* KO cells proliferate more slowly in culture compared to KATOIII parental cells (right). Scale bars, 500μm. (**H**) KATOIII parental cells seed large, invasive tumours in mice following orthotopic transplantation, but the same line with *AQP5* KO fail to establish orthotopic tumours in mice in the majority of cases examined. $n = 5$ biological replicates; scale bars, 1mm. Statistical analysis was performed using a Mann-Whitney *U*-test. Graphs represent mean ± S.D. with two-tailed unpaired *t*-test unless otherwise stated.

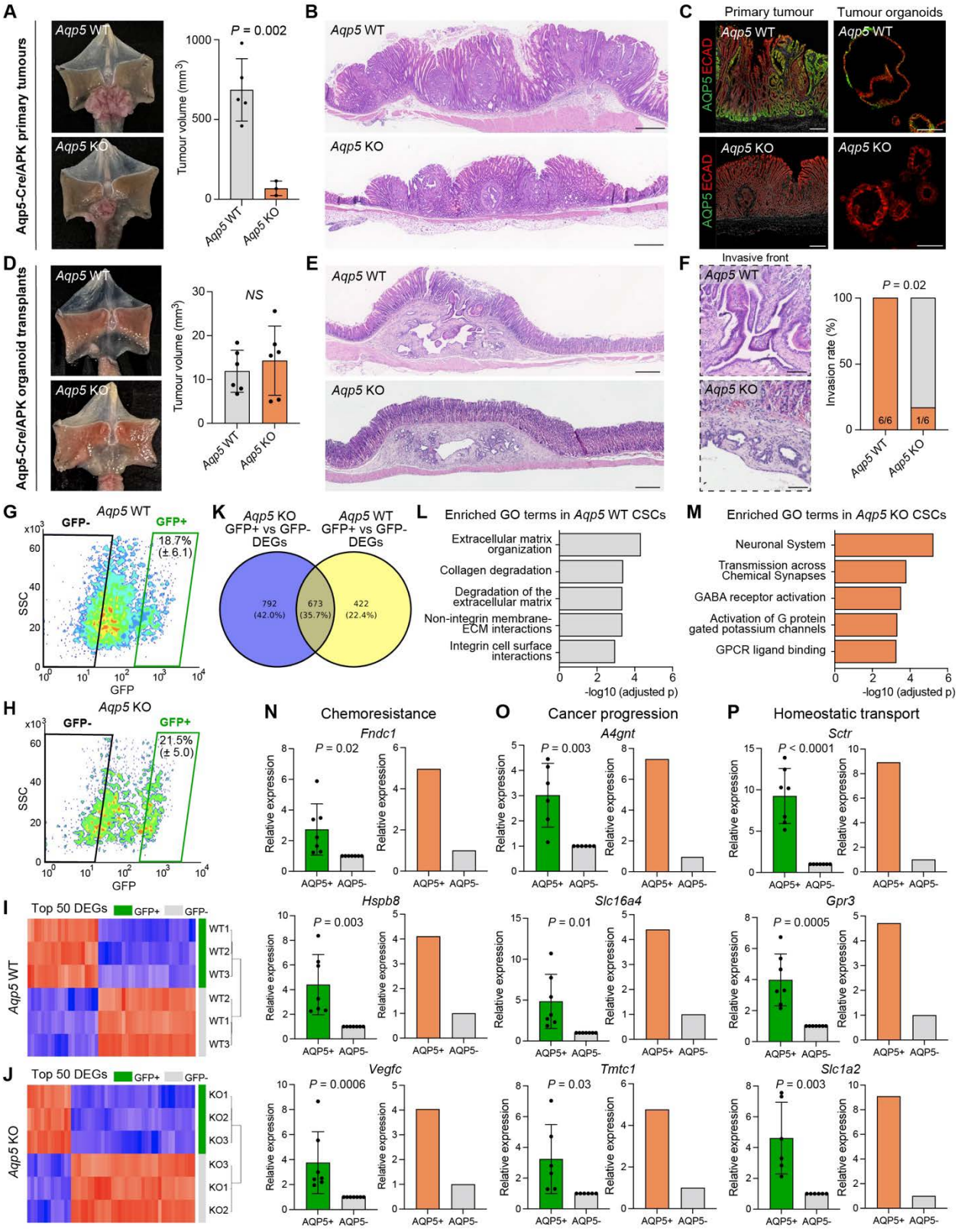
A
Aqp5-Cre/APK primary tumours
Aqp5 WT
Aqp5 KO
P = 0.002
Tumour volume (mm3)
1000
500
0
Aqp5 WT
Aqp5 KO
B
Aqp5 WT
Aqp5 KO
C
Primary tumour
Tumour organoids
AQP5 ECAD
Aqp5 WT
Aqp5 KO
D
Aqp5-Cre/APK organoid transplants
Aqp5 WT
Aqp5 KO
NS
Tumour volume (mm3)
30
20
10
0
Aqp5 WT
Aqp5 KO
E
Aqp5 WT
Aqp5 KO
F
Invasive front
Aqp5 WT
Aqp5 KO
P = 0.02
Invasion rate (%)
100
50
0
6/6
1/6
Aqp5 WT
Aqp5 KO
G
Aqp5 WT
GFP-
GFP+
18.7%
(± 6.1)
SSC
GFP
H
Aqp5 KO
GFP-
GFP+
21.5%
(± 5.0)
SSC
GFP
K
Aqp5 KO GFP+ vs GFP- DEGs
Aqp5 WT GFP+ vs GFP- DEGs
792
(42.0%)
673
(35.7%)
422
(22.4%)
L
Enriched GO terms in Aqp5 WT CSCs
Extracellular matrix organization
Collagen degradation
Degradation of the extracellular matrix
Non-integrin membrane-ECM interactions
Integrin cell surface interactions
-log10 (adjusted p)
M
Enriched GO terms in Aqp5 KO CSCs
Neuronal System
Transmission across Chemical Synapses
GABA receptor activation
Activation of G protein gated potassium channels
GPCR ligand binding
-log10 (adjusted p)
I
Top 50 DEGs
GFP+
GFP-
Aqp5 WT
WT1
WT2
WT3
J
Top 50 DEGs
GFP+
GFP-
Aqp5 KO
KO1
KO2
KO3
N
Chemoresistance
Fndc1
P = 0.02
Hspb8
P = 0.003
Vegfc
P = 0.0006
O
Cancer progression
A4gnt
P = 0.003
Slc16a4
P = 0.01
Tmtc1
P = 0.03
P
Homeostatic transport
Sctr
P < 0.0001
Gpr3
P = 0.0005
Slc1a2
P = 0.003
Relative expression
AQP5+
AQP5-

Fig. S16. AQP5 drives tumour progression in a primary mouse model of gastric cancer. (**A**) Representative whole mount images of *Aqp5* wildtype (WT) and knockout (KO) mouse pyloric tumours (left), with quantification of tumour volumes (right). *n* = 3 biological replicates. (**B**) H&E showing tumour histology of *Aqp5* WT and *Aqp5* KO mouse pyloric tumours. *n* = 3 biological replicates; scale bars, 1mm. (**C**) Representative immunofluorescence images of *Aqp5* WT and *Aqp5* KO pyloric tumours confirming the loss of AQP5 in the KO tumours (left). Mouse pyloric tumour organoids generated from *Aqp5* WT and *Aqp5* KO tumours reflect the pattern of AQP5 expression in the original tumours (right). *n* = 3 biological replicates; scale bars, 1mm (left), 500μm (right). (**D**) Representative whole mount images of orthotopic tumours derived from transplanted *Aqp5* WT and *Aqp5* KO mouse pyloric tumour organoids (left), with quantification of tumour volumes (right). *n* = 6 biological replicates. (**E**) *Aqp5* KO tumour organoids form less invasive tumours following transplantation into immune-deficient mice compared to *Aqp5* WT tumour organoids. *n* = 6 biological replicates; scale bars, 1mm. (**F**) Insets highlighting the invasive front present in orthotopic tumours derived from transplanted *Aqp5* WT and *Aqp5* KO tumour organoids (left), with quantification of tumour invasion rates (right). Statistical analysis was performed using a Fisher's exact test; scale bars, 200μm. (**G** and **H**) FACS gating strategy for isolation of tumour epithelial GFP+ (stem) and GFP- (rest of tumour) cells from *Aqp5* WT (G) and *Aqp5* KO (H) mouse pyloric tumours. SSC, side scatter. (**I** and **J**) Heatmap of the top 50 differentially expressed genes (DEGs) between GFP+ and GFP- samples isolated from 3 independent mouse pyloric tumours with either *Aqp5* WT (I) or *Aqp5* KO (J) backgrounds. (**K**) Venn diagram of the DEGs common and unique between the *Aqp5* WT and *Aqp5* KO cancer stem cell-enriched transcriptomic profiles. (**L**) Gene ontology (GO) terms represented in DEGs significantly enriched in *Aqp5* WT cancer stem cells (CSCs), largely associated with extracellular matrix remodelling. The x-axis shows the negative log10 transform of the adjusted *P* values. (**M**) Gene ontology (GO) terms represented in DEGs significantly enriched in *Aqp5* KO cancer stem cells (CSCs), including neuronal signalling-related pathways. The x-axis shows the negative log10 transform of the adjusted *P* values. (**N** to **P**) qPCR validation (left graphs) and RNAseq expression data (right graphs) of selected genes upregulated in the GFP+ stem cells of *Aqp5* WT tumours compared to *Aqp5* KO tumours, with putative roles in chemoresistance (N), cancer progression (O), and homeostatic transport (P). Statistical analyses were performed using two-tailed t-test for all genes except for Vegfc, which was analysed with Mann-Whitney *U*-test. Graphs represent mean ± S.D. with two-tailed unpaired *t*-test unless otherwise specified.

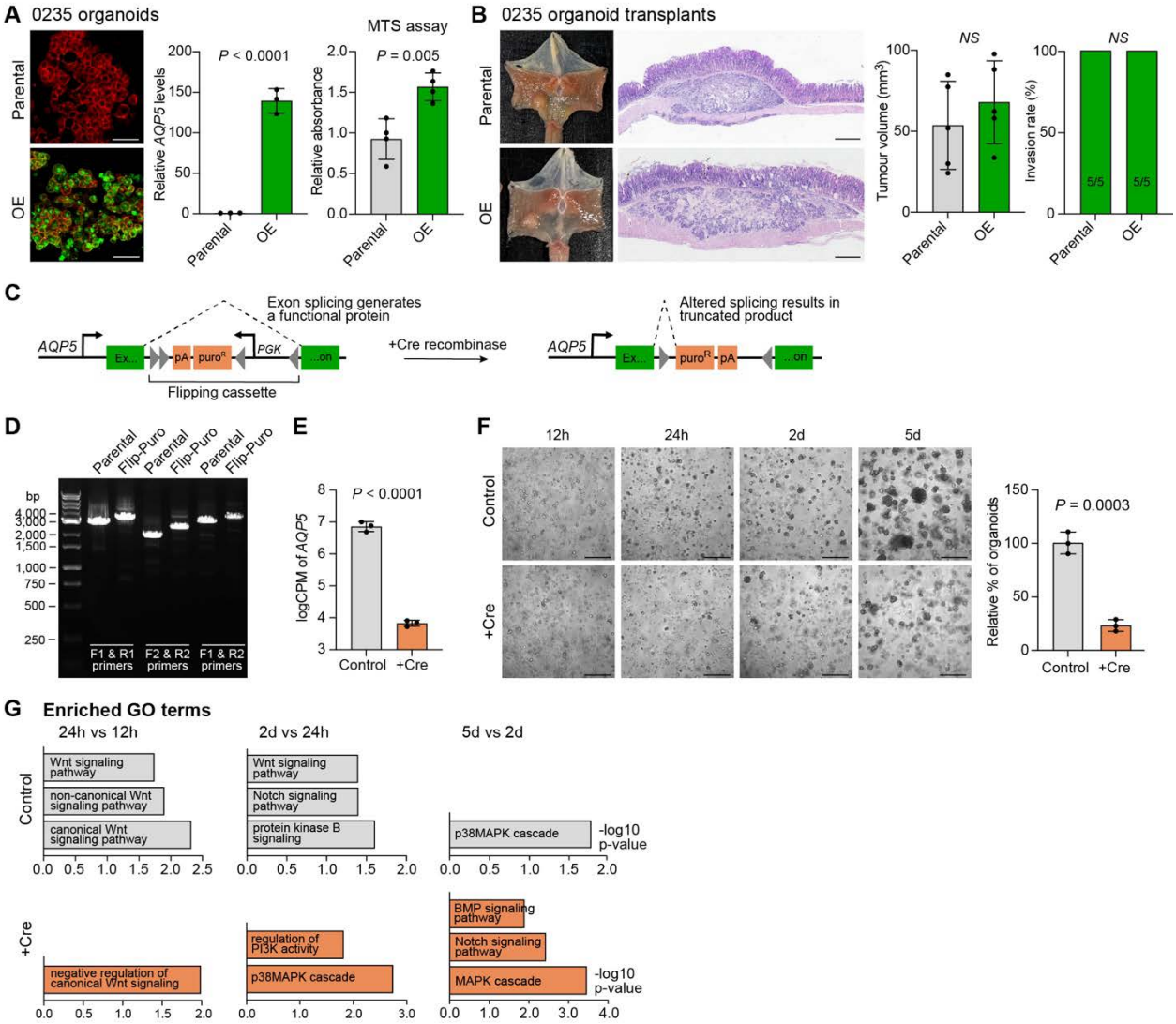

Fig. S17. AQP5 drives tumour progression in human organoid models of gastric cancer. (**A**) Representative immunofluorescence images (left) and qPCR of *AQP5* levels (middle) confirm the upregulation of AQP5 in the diffuse-type 0235 *AQP5*-overexpressing (OE) human gastric cancer organoid line. $n = 3$ independent replicates; scale bars, 500μm. 0235 *AQP5* OE organoids show higher cell proliferation rates *in vitro* compared to the parental line as measured by an MTS proliferation assay (right). (**B**) Representative whole mount and H&E images (left) depict the histological features of the tumours formed from transplanted parental and *AQP5* OE organoids, with quantifications of tumour volumes (middle) and invasion rates (right). $n = 5$ biological replicates; scale bars, 1mm. Statistical analysis for invasion rate was performed using a Fisher's exact test. (**C**) *FLIP-Puro* cassette used in generating Cre-inducible *AQP5* KO in human gastric cancer organoids. Administration of Cre gesicles to induce recombination of the flipping cassette results in altered splicing and a truncated *AQP5* gene product. (**D**) Genomic PCR performed at the insertion site of *AQP5 FLIP-Puro* confirms successful insertion based on expected band sizes. (**E**) Quantification of logCPM values confirms the loss of *AQP5* expression in Cre recombinase-treated *AQP5 FLIP-Puro* organoids at day 5. (**F**) Representative brightfield images of control and Cre recombinase-treated (+Cre) *AQP5 FLIP-Puro* organoids, across the 4 indicated timepoints

(12h, 24h, 2d, and 5d), showing significantly reduced organoid growth following *AQP5* loss. Graph shows relative organoid counts at the 5-day timepoint. $n = 3$ independent replicates; scale bars, 500μm. (**G**) Gene ontology (GO) terms enriched in DEGs obtained in control and Cre recombinase-treated (+Cre) samples across the timepoints indicated, reflecting dysregulated WNT, PI3K, and p38MAPK signalling downstream of *AQP5* loss. Graphs represent mean ± S.D. with two-tailed unpaired *t*-test unless otherwise specified.

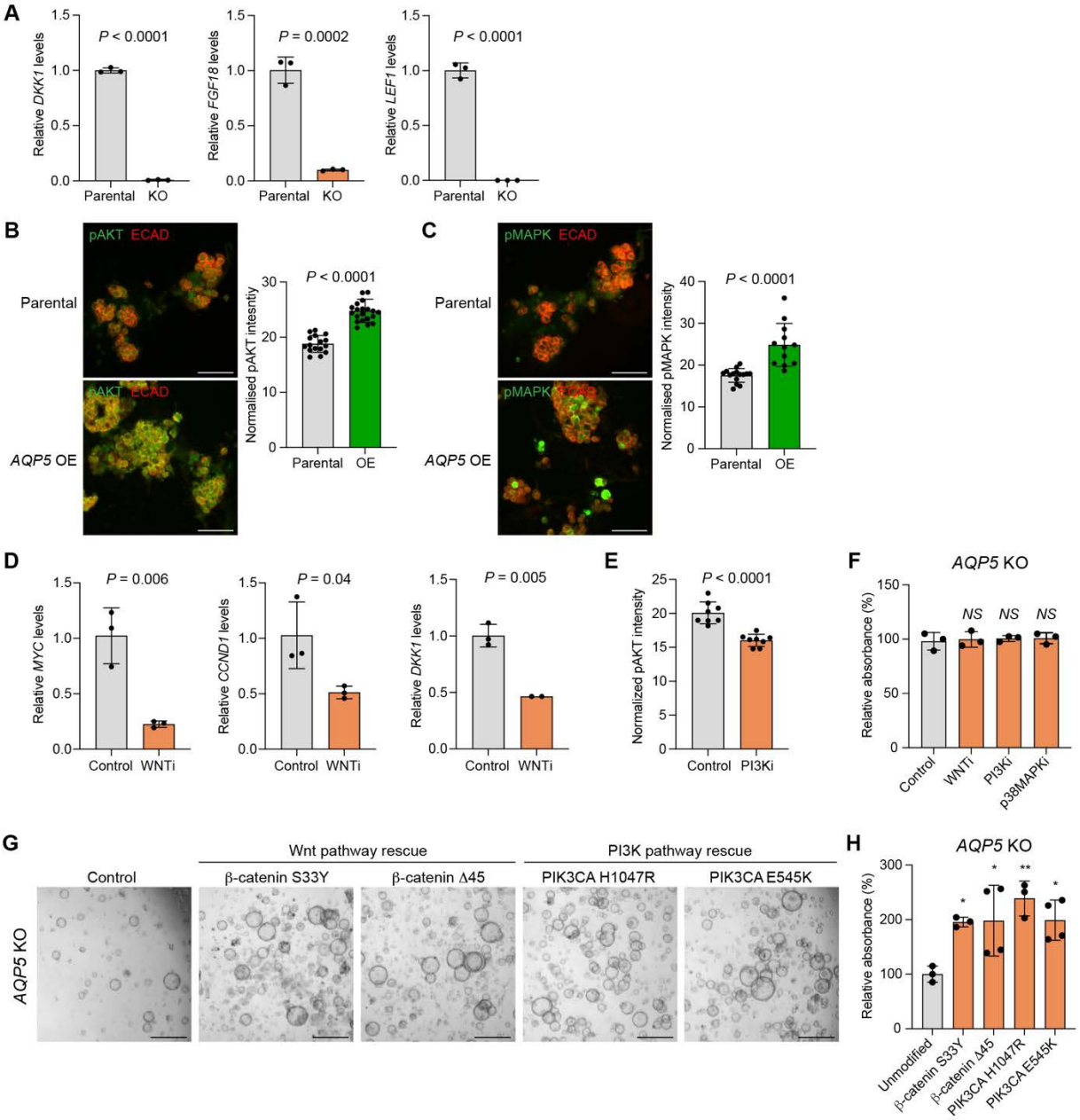

Fig. S18. AQP5 promotes cell proliferation in gastric cancer via WNT, PI3K, and MAPK pathways. (**A**) qPCR of WNT target genes *DKK1*, *FGF18*, and *LEF1* showing downregulated expression within *AQP5* KO organoids relative to parental organoids. (**B** and **C**) Representative immunofluorescence images (left) and quantifications (right) of pAKT (B) and pMAPK (C) expression in parental and *AQP5*-overexpressing (OE) organoids, showing elevated PI3K and MAPK signalling in *AQP5* OE organoids relative to parental organoids. n = 3 independent replicates; scale bars, 500μm. (**D**) qPCR of WNT target genes *MYC*, *CCND1*, and *DKK1* showing downregulated expression within organoids treated with WNTi. (**E**) Quantification of normalized pAKT expression in control and PI3Ki-treated organoids, confirming the reduction in PI3K signalling following inhibitor treatment. (**F**) *AQP5* KO organoids treated with WNTi, PI3Ki, or p38MAPKi do not display significant changes in cell proliferation as measured by an *in vitro* MTS

colorimetric assay. (**G**) Representative images of *AQP5* KO organoids (left), two WNT pathway rescue organoid lines (middle), and two PI3K pathway rescue organoid lines (right); scale bars, 500μm. (**H**) Quantification of cell proliferation for the same 5 organoid lines using an *in vitro* MTS colorimetric assay, showing elevated proliferation across the rescue lines. Statistical analyses were performed using one-way ANOVA with Dunnett's multiple comparisons test. $^{**}P < 0.05$, $^{**}P < 0.005$. Graphs represent mean ± S.D. with two-tailed unpaired *t*-test unless otherwise specified.

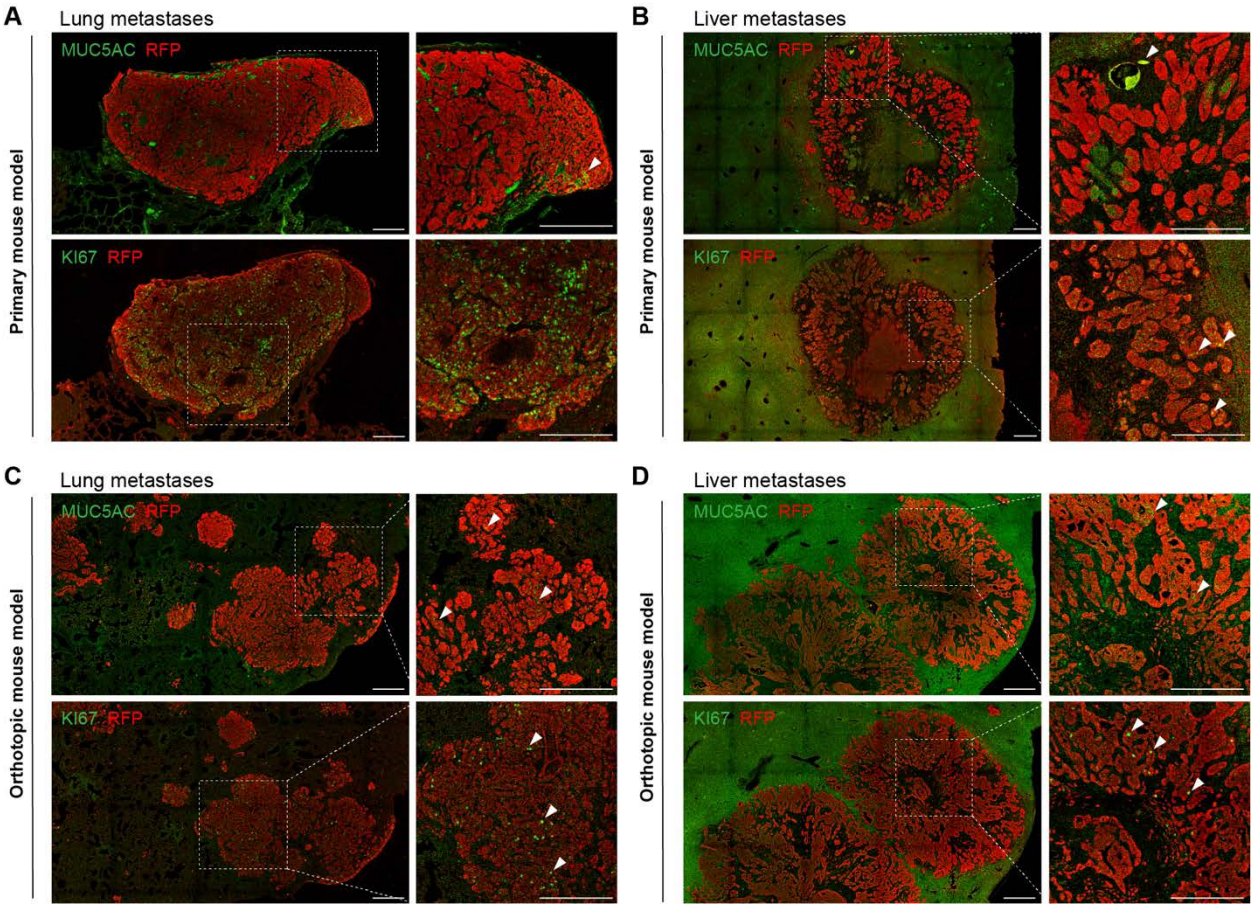

Fig. S19. Characterization of lung and liver metastases in primary and orthotopic pyloric cancer mouse models. (**A** and **B**) Co-immunofluorescence of RFP (demarcating the tumour region) and MUC5AC or KI67 markers on metastatic tissue sections derived from the lungs (A) or liver (B) in the primary pyloric cancer mouse model. White arrows indicate examples of MUC5AC+ or KI67+ tumour cells. n = 3 independent replicates; scale bars, 1mm. (**C** and **D**) Co-immunofluorescence of RFP (demarcating the tumour region) and MUC5AC or KI67 markers on metastatic tissue sections derived from the lungs (C) or liver (D) in the orthotopic pyloric cancer mouse model. White arrows indicate examples of MUC5AC+ or KI67+ tumour cells. n = 3 independent replicates; scale bars, 1mm.